

1995

Numerical modeling of reactive gas assisted laser cutting of metals

Chin Kooi Lim
Iowa State University

Follow this and additional works at: <https://lib.dr.iastate.edu/rtd>

 Part of the [Mechanical Engineering Commons](#)

Recommended Citation

Lim, Chin Kooi, "Numerical modeling of reactive gas assisted laser cutting of metals " (1995). *Retrospective Theses and Dissertations*. 10923.
<https://lib.dr.iastate.edu/rtd/10923>

This Dissertation is brought to you for free and open access by the Iowa State University Capstones, Theses and Dissertations at Iowa State University Digital Repository. It has been accepted for inclusion in Retrospective Theses and Dissertations by an authorized administrator of Iowa State University Digital Repository. For more information, please contact digirep@iastate.edu.

INFORMATION TO USERS

This manuscript has been reproduced from the microfilm master. UMI films the text directly from the original or copy submitted. Thus, some thesis and dissertation copies are in typewriter face, while others may be from any type of computer printer.

The quality of this reproduction is dependent upon the quality of the copy submitted. Broken or indistinct print, colored or poor quality illustrations and photographs, print bleedthrough, substandard margins, and improper alignment can adversely affect reproduction.

In the unlikely event that the author did not send UMI a complete manuscript and there are missing pages, these will be noted. Also, if unauthorized copyright material had to be removed, a note will indicate the deletion.

Oversize materials (e.g., maps, drawings, charts) are reproduced by sectioning the original, beginning at the upper left-hand corner and continuing from left to right in equal sections with small overlaps. Each original is also photographed in one exposure and is included in reduced form at the back of the book.

Photographs included in the original manuscript have been reproduced xerographically in this copy. Higher quality 6" x 9" black and white photographic prints are available for any photographs or illustrations appearing in this copy for an additional charge. Contact UMI directly to order.

UMI

A Bell & Howell Information Company
300 North Zeeb Road, Ann Arbor, MI 48106-1346 USA
313/761-4700 800/521-0600



Numerical modeling of reactive gas assisted laser cutting of metals

by

Chin Kooi Lim

**A Dissertation Submitted to the
Graduate Faculty in Partial Fulfillment of the
Requirements for the Degree of
DOCTOR OF PHILOSOPHY**

**Department: Mechanical Engineering
Major: Mechanical Engineering**

Approved:

Signature was redacted for privacy.

Signature was redacted for privacy.

In Charge of Major Work

Signature was redacted for privacy.

For the Major Department

Signature was redacted for privacy.

For the Graduate College

**Iowa State University
Ames, Iowa
1995**

UMI Number: 9531759

UMI Microform 9531759

Copyright 1995, by UMI Company. All rights reserved.

**This microform edition is protected against unauthorized
copying under Title 17, United States Code.**

UMI

**300 North Zeeb Road
Ann Arbor, MI 48103**

TABLE OF CONTENTS

ACKNOWLEDGMENTS	x
CHAPTER 1. INTRODUCTION	1
Background	2
The CO_2 Laser	3
The Laser Cutting Process	4
Literature Review	6
Experimental Research	6
Computational Research	8
Present Model of Laser Cutting	10
Interfaces	12
Liquid Phase	13
Gas Phase	14
Oxidation Reactions	14
CHAPTER 2. GOVERNING EQUATIONS	16
Gas Phase: Compressible Flow	16
Thin-Layer Approximation	19
Liquid Phase: Incompressible Flow	20
Interface Conditions	22

Physical Properties	24
Liquid Iron	24
Coaxial Jet	27
Laser Beam Characteristics	28
Oxidation Reactions	29
CHAPTER 3. NUMERICAL ALGORITHM	32
Temporal Discretization	32
Artificial Compressibility Method	33
Spatial Discretization	34
Spatial Discretization of LHS	35
Spatial Discretization of RHS	38
Inviscid and Viscous Jacobians	43
Compressible Flow Equations	43
Incompressible Flow Equations	45
Implementation of Boundary Conditions	46
Free Surface Conditions	46
Symmetry/Periodic Conditions	48
Inflow/Outflow Conditions	49
Wall Conditions	50
Overall Solution Procedure	51
CHAPTER 4. RESULTS AND DISCUSSIONS	54
Incompressible Flow	54
Circular Cylinder $Re = 40$	54
Circular Cylinder $Re = 200$	56

Compressible Flow	63
Shock Tube	63
Supersonic Flow in a 10° Double-Wedge Channel	64
Axisymmetric Flow over SOCBT Projectile	68
Shock-Boundary Layer Interaction	77
Reactive Gas Assisted Laser Cutting	80
Axisymmetric Jet Impingement Solutions	83
Laser Cutting Solutions	86
CHAPTER 5. CONCLUSIONS	111
REFERENCES	114
APPENDIX EXPERIMENTAL INVESTIGATION	120

LIST OF FIGURES

Figure 1.1:	Schematic of a typical laser resonator	3
Figure 1.2:	A simplified energy levels of the CO_2 molecule and transition which produce the laser beam	4
Figure 1.3:	Schematic of the laser cutting process	5
Figure 1.4:	Schematic of the molten layer	12
Figure 3.1:	Implementation of symmetry boundary conditions by reflecting the $i = 3$ line about the symmetry line $i = 2$	48
Figure 3.2:	Schematic of the overall solution procedure	52
Figure 4.1:	50×53 O-type grid for the upper half of the circular cylinder . . .	55
Figure 4.2:	Comparison of pressure coefficient distributions on the circular cylinder at $Re = 40$	57
Figure 4.3:	Comparison of skin friction coefficient distributions on the circu- lar cylinder at $Re = 40$	58
Figure 4.4:	Streamlines of the flow over the circular cylinder at $Re = 40$. . .	59
Figure 4.5:	Pressure contours for the flow over the circular cylinder at $Re = 40$	59
Figure 4.6:	100×35 O-type grid for the complete circular cylinder	60

Figure 4.7:	Time evolution of lift and drag coefficients on the circular cylinder at $Re = 200$	61
Figure 4.8:	Streamlines of the flow over the circular cylinder at $t = 160.00, 161.44, 162.88, 164.32,$ and 165.76 at $Re = 200$	62
Figure 4.9:	Comparison of pressure distributions in the shock tube at $t = 0.211$ using the 3rd order upwind biased scheme	65
Figure 4.10:	Comparison of Mach number distributions in the shock tube at $t = 0.211$ using the 3rd order upwind biased scheme	66
Figure 4.11:	Comparison of density distributions in the shock tube at $t = 0.211$ using the 3rd order upwind biased scheme	67
Figure 4.12:	91×40 grid for the 10° double-wedged channel	68
Figure 4.13:	Comparison of pressure coefficient distributions on the lower surface at $M_\infty = 2.0$	69
Figure 4.14:	Comparison of pressure coefficient distributions on the upper surface at $M_\infty = 2.0$	70
Figure 4.15:	Comparison of Mach number distributions on the lower wall using the 3rd order upwind biased scheme with and without Roe's "Superbee" limiter	71
Figure 4.16:	Comparison of Mach number distributions on the upper wall using the 3rd order upwind biased scheme with and without Roe's "Superbee" limiter	72
Figure 4.17:	Comparison of pressure coefficient contours in the channel with and without Roe's "Superbee" limiter	73
Figure 4.18:	89×30 hyperbolic grid around the SOCBT projectile	74

Figure 4.19:	Comparison of surface pressure coefficients at $M_\infty = 0.96$ with measured data for the SOCBT projectile	75
Figure 4.20:	Pressure contours near the SOCBT projectile at $M_\infty = 0.96$. . .	76
Figure 4.21:	Comparison of pressure distributions on the surface of the flat plate in the shock impingement problem	78
Figure 4.22:	Comparison of skin friction distributions on the surface of the flat plate in the shock impingement problem	79
Figure 4.23:	Velocity vectors of the separated region in the shock impingement problem	81
Figure 4.24:	Pressure contours in the shock impingement problem	81
Figure 4.25:	Nozzle geometry assumed in the jet impingement calculations . .	84
Figure 4.26:	60×40 grid for the jet impingement calculations	85
Figure 4.27:	Mach contours in the vicinity of the nozzle exit	87
Figure 4.28:	Velocity vectors in the vicinity of the nozzle exit showing the entrainment effects	88
Figure 4.29:	Stagnation pressure on the surface of the workpiece	89
Figure 4.30:	Various contour plots of the gas jet flow field within the kerf . . .	90
Figure 4.31:	Nondimensionalized pressure and shearing stress on the erosion front due to the gas jet	92
Figure 4.32:	Axial force coefficient distributions on the erosion front due to pressure and shearing stress of the gas jet	94
Figure 4.33:	Streamlines within the molten layer shown in sections of $0.625t$ from left to right	95
Figure 4.34:	Variation of laser beam incident angle along the erosion front . .	96

Figure 4.35:	Curvature effects on the laser-material coupling at the melt interface	98
Figure 4.36:	Typical striation pattern on the edges of the kerf	98
Figure 4.37:	Evolution of the erosion front profile subjected to a sustained pressure disturbance ($\Delta t = 0.16$)	100
Figure 4.38:	Nondimensionalized heat flux at the erosion front due to laser beam, oxidation, convection, and radiation losses	102
Figure 4.39:	Temperature distribution at the erosion front	103
Figure 4.40:	Nondimensionalized temperature across the molten layer at vari- ous x/D locations	104
Figure 4.41:	Nondimensionalized velocity magnitude across the molten layer at various x/D locations	105
Figure 4.42:	Nondimensionalized heat flux due to laser beam and oxidation, and conduction loss in the solid phase	107
Figure 4.43:	Nondimensionalized heat flux due to advection at the exit plane of the molten layer	108
Figure 4.44:	Various TEM modes and their spatial energy distributions	110
Figure A.1:	SEM pictures of the melt interfaces for case 1 ($t = 3.175$ mm) . .	124
Figure A.2:	SEM pictures of the melt interfaces for case 2 ($t = 6.35$ mm) . .	125

LIST OF TABLES

Table 4.1:	Summary of cutting parameters used in the modal laser cutting case considered in the present study	82
Table 4.2:	Percentages of heat due to conduction, advection, and phase change with respect to the total heat input	109
Table A.1:	Variation of inclination angle with cutting speed for case 2 ($t = 3.175$ mm)	123

ACKNOWLEDGMENTS

I would first of all like to express my sincere gratitudes to my major professors, Dr. R. C. Brown and Dr. P. A. Molian, for their continuous guidance and encouragement. I am grateful to the members of my examining committee for their insightful suggestions and to Dr. J. M. Prusa for the helpful discussions on the free surface modeling considered in my dissertation work. I also thank the department secretary, Ms. Rosalie Enfield, for taking care of all my paper work throughout the years.

I would also like to acknowledge the departmental support in the form of teaching assistantship that made it possible for me to pursue my doctorate degree. I should also acknowledge the partial financial support from the National Science Foundation through the grant NSF-DMI-9407735.

I want to express my sincere appreciation to my parents. I am thankful for their understanding and patience during my many years away from home. I am fortunate to have my wife, Lieng, here with me in Ames for the last two years. No words can describe the sacrifices she made to make this possible. This dissertation is dedicated to her.

CHAPTER 1. INTRODUCTION

The application of high power lasers and reactive gases in the cutting of metals has reached a high degree of industrial maturity. The ease of interfacing lasers with computer controls and robots has resulted in more efficient and cost-effective manufacturing processes [1–3]. Nevertheless, performance measures of laser cutting, such as cutting speed, section thickness, and cut quality have to be improved for any extension of the present range of industrial applications.

The physical phenomena occurring during reactive gas assisted laser cutting are not fully understood at the present time. Fundamentally, laser cutting is a thermal process. Numerous models based on energy balance between the laser beam and the workpiece have been proposed and have been quite successful in predicting various performance parameters such as the maximum cutting speed for a given laser power. However, these models failed to yield any conclusion on the fluid dynamics of the molten metal layer, the effects of the gas jet, the laser-material interaction, or the extent of oxidation reaction—all of which are essential for a complete understanding of the process.

The objective of the present study is to develop a model for laser cutting which addresses these various effects. This is achieved by solving the appropriate governing equations for the molten layer and the gas jet. This fundamental approach is expected to yield an accurate representation of the significance of various physical phenomena that

affect laser cutting.

Background

The generation of the laser beam requires that certain group of atoms or molecules be in a non-equilibrium situation known as population inversion [4]. Population inversion refers to the condition where more atoms or molecules are in some excited state than are in the state to which radiative transition would most probably occur. The inversion can, in principle, be established by a variety of excitation processes, the most common being electrical discharge.

When transitions occur, photons are spontaneously emitted in all directions. The photons traveling through the lasing medium (or host) will *stimulate* other excited atoms or molecules to undergo transition when the photons pass near these atoms or molecules. The photons that are emitted this way travel in the same direction and have the same polarization as the stimulating photons. This phenomenon provides the *amplification* in a laser. Further amplification is achieved by reflecting the photons back and forth through the lasing medium with an optical resonator as depicted in Fig. 1.1. Some photons leave the laser cavity through a hole in one mirror of the resonator to form the laser beam.

The concept of light amplification by stimulated emission of radiation (LASER) has been known since the early 1900's. However, experimental verification of the concept was not achieved until Theodore Maiman built the first ruby laser in 1960 at the Hughes Laboratories. In the ruby laser, the lasing material is the triply ionized chromium atoms, Cr^{3+} , which are dispersed in a lasing host made of aluminum oxide, Al_2O_3 . Following this, development of other types of lasers proceeded rapidly. The first gas laser appeared in 1961 when Ali Javan introduced the He-Ne laser at the Bell Telephone Laboratories. Since

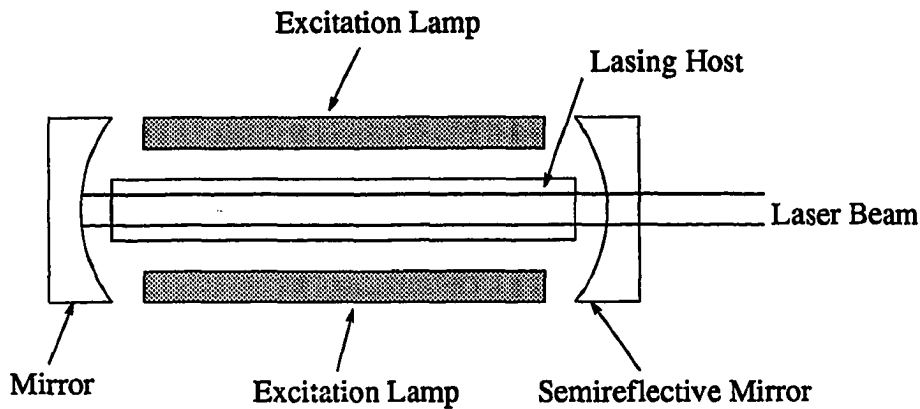


Figure 1.1: Schematic of a typical laser resonator

then, newer types of laser that are more powerful and reliable in their operations have been developed.

The CO_2 Laser

The CO_2 laser is the most common high power laser used for cutting applications. It can be operated in a continuous wave mode at output power of several kilowatts at a wavelength of $10.6\mu\text{m}$. The CO_2 laser is a molecular laser in which molecular vibrations rather than electronic transitions provide the mechanism for lasing action. Pure CO_2 can be made to lase but only very weakly and, therefore, most CO_2 lasers utilize a mixture of CO_2 , N_2 , and He in a typical ratio of 0.4:4.5:10 [5].

The lasing in a CO_2 laser can be illustrated with a simplified version of its energy levels as shown in Fig. 1.2. The CO_2 molecules, initially at level 1, absorb energy when they collide with the N_2 molecules and are elevated to a higher energy level (level 2). This is followed by a rapid non-radiative transition to level 3 with lasing occurring between this level and another intermediate level 4. The lifetime of the CO_2 molecules at level 3 is on

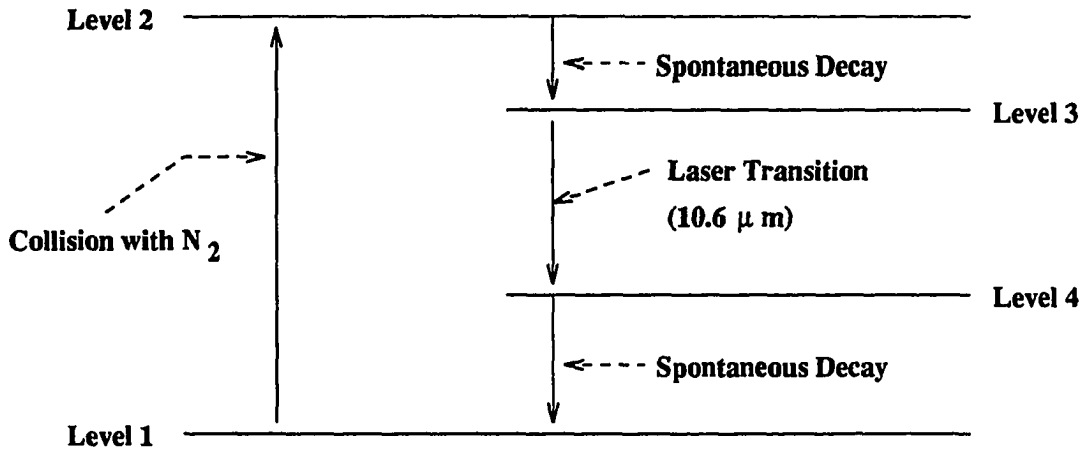


Figure 1.2: A simplified energy levels of the CO_2 molecule and transition which produce the laser beam

the order of 1 ms compare to the other levels which are on the order of 1 μ s. This allows a population inversion to establish between level 3 and level 4. Subsequent collisions with *He* atoms (which act like a thermal sink) and with the walls of the discharge tube return the CO_2 molecules back to level 1.

All high power CO_2 lasers use some form of flowing gas technique to ensure a fresh supply of gas in the laser cavity at all times. Although many designs simply exhaust the gas into the atmosphere, most high power lasers (because of high flow rates) recirculate the gas through a heat exchanger. The recirculating gas is also continuously or periodically filtered and replaced with fresh gas to keep the flowing gas free of decomposition products, particularly carbon monoxide (CO), which absorbs radiation at 10.6 μ m and may quench the lasing action.

The Laser Cutting Process

Figure 1.3 shows a typical gas assisted laser cutting process. The laser beam is focused

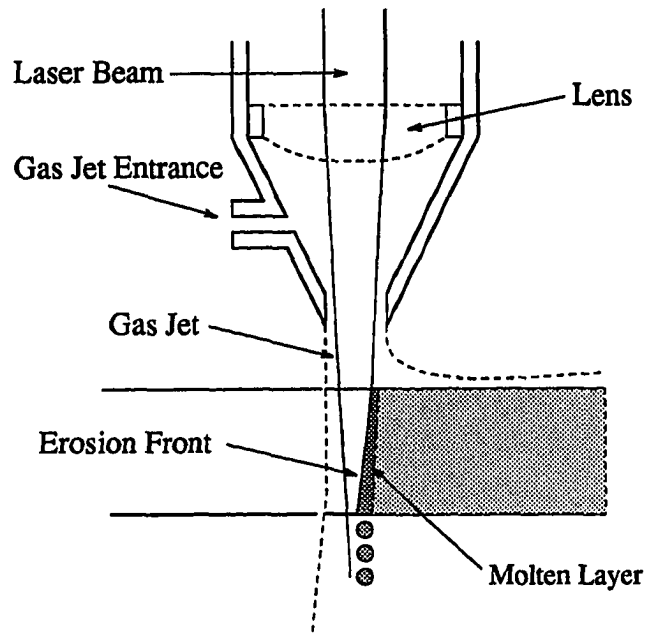


Figure 1.3: Schematic of the laser cutting process

by an optical system onto the surface of the material (or workpiece) being cut. Oxygen is supplied to the cutting zone through a nozzle coaxial to the laser beam. The incident radiation heats up the surface of the workpiece and eventually causes the workpiece to melt. A thin molten layer is then formed on a nearly vertical plane at the end of the cut. The molten material is continuously removed from the cutting area or kerf through evaporation and through forceful ejection by the pressure and shearing forces of impinging gas jet [6]. The forceful ejection of the molten layer causes the layer to oscillate [7] and as a result, striations are created on the edges of the kerf.

For metallic materials, only a small portion of the laser radiation is absorbed at the onset of the cut but subsequent heating and the formation of a metal oxide scale rapidly increases the absorptivity at the erosion front, sometimes up to near 100 percent [8]. The

oxidation reactions also serve as an additional heat source, and in some cases, account for half the energy input in the process. The kerf width (or cut width) is usually slightly larger than the diameter of the laser beam and any thermal-damage zone (heat affected zone or HAZ) is limited to a few millimeter along the edges of the cut.

Literature Review

Almost all improvements in laser cutting techniques have come from experimental studies. Although various models for laser cutting have been developed, they are used primarily for providing rough estimations of the maximum cutting speed or cutting depth and, hence, contribute little to the understanding the actual phenomena.

Experimental Research

The feasibility of using laser for cutting application was first demonstrated in the mid-sixties. An assist-gas has always been used to protect the lens assembly from the debris in the cutting zone but subsequent studies by Sullivan and Houldcroft [9] showed that using oxygen as the assist gas allowed thicker metals to be cut at faster rates and with lower power requirement. This improvement was attributed to the additional heat source provided by the oxidation reactions at the erosion front.

The efficiency of the cutting process depends, to a great extent, on the reflectivity at the cut surface. High power lasers [10] with shorter wavelengths were found to improve the laser-material coupling by reducing the reflectivity at the erosion front. Other techniques that were found to improve the cutting efficiency include coating the cut surface with a highly absorbent agent and preheating the workpiece.

The characteristics of the laser beam such as beam mode, wavelength, beam size, and polarization have all been shown to affect the quality of the cut. Belforte [11] reported that the TEM₀₀ (essentially Gaussian in spatial distribution) beam mode can be focused to a smaller spot size, which resulted in a significant increase in energy density at the cut surface. Olsen [12] observed that optimal cutting speeds were achieved when the polarization of the laser beam was aligned with the direction of the cut. The location of the focal point of the laser beam was also found to affect laser cutting, especially for thicker plates. Rothe and Sepold [13] observed that better cut performance was achieved when the focal point was located one-third of the thickness beneath the surface of the workpiece.

Sepold and Rothe [14] showed an increase in cutting speed by operating the nozzle at total pressure values which would produce supersonic velocity in the gas jet. This observation was also confirmed independently by Steen and Kamalu [15]. However, Duley [16] reported that there is a point beyond which any further increase in total pressure of the nozzle would actually cause a decrease in the cutting speed. This point was found to correspond closely to the onset of a Mach shock disc (MSD) above the workpiece. Recent studies [17,18] have also shown improvement in cutting speed with convergent-divergent nozzles. This was attributed to the more favorable shock structure with a convergent-divergent nozzle. Furthermore, certain cross sectional shapes of the nozzle and nozzle designs [19,20] have yielded higher cutting speeds and better cut quality by delaying the onset of MSD. While the jet from coaxial nozzles is limited by the nozzle pressure and fixed jet orientation, the use of an auxiliary jet in tandem with the coaxial jet has resulted in a vast improvement in the cutting speed as well as the cutting depth [21–24].

The effects of chemical reactions have also been studied extensively. Forbes [20], for example, estimated that in oxygen-assisted laser cutting of steel, only 30 percent of

the energy came from the laser while the remaining 70 percent was due to the exothermic energy associated with the oxidation reactions when optimum cutting speed was achieved. Steen and Kamalu [15] compared laser cutting rates of steels for jets of argon and oxygen and concluded that about 60 percent of the cutting energy was supplied by oxidation reactions. Hence, great improvement in cutting efficiency can be achieved by augmenting the chemical reactions. For instance, Molian [25] showed that the use of oxygen and acetylene mixture as the assisting jet had increased the thickness of mild steel that can be cut to 19 mm, which is otherwise impossible with a 1.5KW CO_2 laser.

These studies represent only a small portion of the overall experimental efforts. Extensive reviews on experimental studies can be found in the compilations of Steen and Kamalu [15] and Mazumder [26]. Nevertheless, it is evident from these experimental studies that laser cutting is an extremely complicated process which is dependent on many physical mechanisms.

Computational Research

Models of laser cutting can be useful tools in evaluating the fundamental mechanisms of the cutting process. Models can be used to evaluate proposed mechanisms and to assess the sensitivity of various performance parameters to the various mechanisms that act in parallel. Eventually, models can be used to optimize the cutting process and to explore new cutting techniques.

Most published reactive gas assisted laser cutting models are based on relatively simple mathematical formulations. They are invariably developed based on heat conduction concepts. Decker *et al.* [27] employed a lumped capacitance model to obtain the cutting speed. This model neglects the heat transfer into the workpiece, thermal radiation, and the

effects of the assisting gas jet. Chemical reaction is treated by a simple inclusion of the heat of chemical reaction per unit time in the overall energy balance. Material removal is achieved only through evaporation (a quasi-sublimation process).

More sophisticated models allow spatial temperature variations by solving the classical heat conduction equation with a moving heat source. This approach forms the basis of the point source model of Babenko and Tychinskii [28]. In their formulation, the chemical reaction effect on the cut is spatially parameterized with respect to a dimensionless thermochemical parameter that is independent of the cutting conditions. Slightly more elaborate models assume cylindrical heat sources such as by Bunting and Cornfield [29]. In this model, the cut edges are assumed to coincide with the melting point isotherm of a moving diffused heat source. Similar consideration can be found in the work of Petring *et al.* [30].

The most sophisticated model on reactive gas assisted laser cutting is represented by the work of Schuöcker [31]. In his model, the equations for mass, momentum, and energy conservation are considered in both the gas and molten metal phase. The erosion front is represented by a flat, planar surface that is slightly tilted from the vertical plane to allow the coupling of laser radiation at the erosion front. Lumped capacitance mass and energy balances are solved for such variables as film thickness, film temperature, and maximum cutting speed for given laser power and material thickness.

The computational work by Vicanek *et al.* [32] is among the few attempts to characterize the fluid dynamics and heat transfer of the jet flow by solving the governing equations without the lumped capacitance consideration. Instead, the fluid dynamics solutions are obtained through conforming mapping of the irrotational, inviscid potential solutions. The pressure distribution on the erosion is then calculated from Bernoulli's equation. Based on

this pressure profile, the boundary layer equations are solved for the wall stress distribution along the erosion front. Although the calculations provided some insight on the jet flow, the assumptions taken to arrive at the final solutions are too rigid for a realistic cutting conditions. For instance, compressibility effects are neglected entirely even though most gas jets in laser cutting are operated at high total pressure.

Present Model of Laser Cutting

The objective of the present study is to develop a model that is suitable for detailed studies of reactive gas assisted laser cutting. As previously pointed out, such a model has to consider the role of the molten layer, the gas jet, and the interaction between the two regions.

The model to be presented will address the following issues which are essential to the better understanding of laser cutting:

- **Absorption of Laser Radiation:** The laser-material coupling should address the possible curvature of the erosion front (the interface between the molten layer and the gas jet) since the absorptivity at the erosion front would depend on the local laser beam angle of incident. This would require that the erosion front itself be allowed to “deform” and its geometry be computed as part of the solutions.
- **Fluid Dynamics of Molten Layer and Gas Jet:** The fluid dynamics of the molten layer and gas jet directly determine the profile (or geometry) of the erosion front. Hence, the appropriate governing equations in each region must be solved in a coupled manner, each is allowed to influence the other.
- **Heat Transfer Phenomena:** Convective and radiative heat losses must be included

in the energy balance at the erosion front. Although these losses have been shown to be small [32] at certain cutting conditions, this determination should be made intrinsically in the model.

- **Oxidation Reactions:** As pointed out previously, oxidation reactions represent an additional heat source and in most cases, its magnitude is of the same order as the laser beam. But, its contribution should be evaluated locally along the erosion front and be made dependent on the flow field solution.

The approach taken in the development of the present model for reactive gas assisted laser cutting is outlined next. Essentially, the theoretical modeling involves solving the appropriate governing equations in both the molten metal and gas phases. The interaction is provided by the interface boundary conditions, namely, the balance of the normal and tangential stresses as well as continuity in flow characteristics such as velocity and temperature. Furthermore, the physical as well as transport properties of the molten metal are assumed to depend only on temperature variation. The laser beam is assumed to have TEM₀₀ mode and the laser-material coupling at the erosion front is assumed to depend only on the angle of incidence. Even though absorptivity is dependent on the surface temperature [33], this effect is neglected in the present study.

The geometry of the molten layer is shown in Fig. 1.4. The inertial coordinates system is chosen such that the x axis is along the nozzle centerline and y axis is in the direction of the cut. The molten layer is delimited by the erosion front (gas-liquid interface) and the melt (liquid-solid) interface. With this reference, the molten material is viewed as being ejected from the melt interface at the cutting velocity.

The location of the nozzle with respect to the erosion front is not well established even from experimental observations. The location would seem to strongly depend on

the cutting speed and the thickness of the workpiece. However, in the present model, a fixed offset between the centerline line of the nozzle and the erosion front is assumed (see Fig. 1.4). The offset (h) is taken as $0.15D$ [32], where D is the diameter of the nozzle exit.

Interfaces

As pointed out previously, it is essential that the profile of the erosion front be computed as a part of the solution rather than treating it a priori. Therefore, the erosion front is treated as a free surface and is allowed to assume its shape as determined by the fluid dynamics near the erosion front. The profile of the erosion front is described by a function $F(x, t)$ (see Fig. 1.4), which is a function of both x and time.

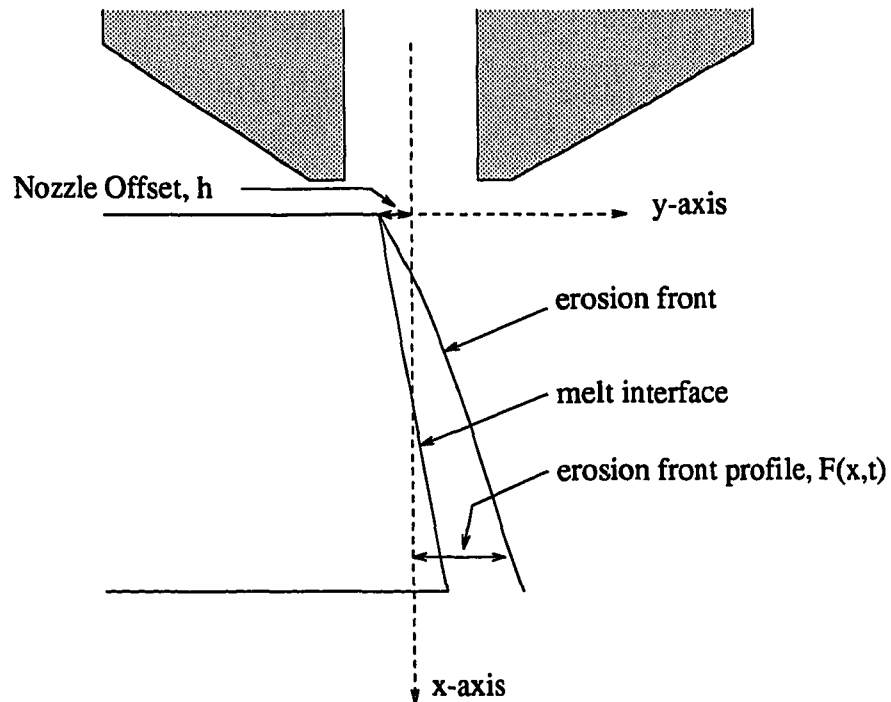


Figure 1.4: Schematic of the molten layer

In principle, the melt interface profile can be obtained from an energy balance of the form

$$-(k_l \nabla T_l - k_s \nabla T_s + \rho \Delta H_f \vec{v}_c) \cdot \hat{n} = \rho \Delta H_f v_n \quad (1.1)$$

where $-(k_l \nabla T_l - k_s \nabla T_s + \rho \Delta H_f \vec{v}_c) \cdot \hat{n}$ is the net heat flux at the melt interface, ρ and ΔH_f are the density and the latent heat of fusion respectively, and v_n is the normal velocity of the melt interface with respect to the cutting speed vector, \vec{v}_c . The local normal vector is represented by \hat{n} . The new profile for the melt interface can be updated from the v_n distribution along the interface. At equilibrium, the left-hand-side in Eqn. 1.1 will be zero, i.e, the melt interface is moving at \vec{v}_c , and an equilibrium melt interface profile is thus obtained. However, such calculations are not necessary if the melt interface has a well defined geometry. As in the models of Schuöcker and Vicanek, the melt interface is assumed to be an inclined plane where the inclination angle is to be determined from experimental observations. As will be shown later, the experimental results obtained in the present study do provide, indeed, a strong justification for this simplification.

Liquid Phase

The fluid dynamics of the molten layer may resemble those encountered in film condensation problems where the boundary layer approximation has been used successfully. However, in the presence of the stresses at the erosion front, coupled with the jet pressure and surface tension effects, the normal pressure gradient might not be zero and the boundary layer approximation becomes inappropriate in this situation. In the present model, the normal momentum equation is included. In addition, the energy equation is solved for the temperature field within the molten layer such that the temperature-dependent transport and physical properties can be incorporated intrinsically into the model.

Gas Phase

For most part, the jet flow is axisymmetric except in the region where part of the jet traverses through the cut kerf. In a typical cutting application, the width of the kerf is roughly one tenth the diameter of the nozzle exit. The kerf is larger at the top surface of the workpiece and tapers down to the bottom surface. Nonetheless, the kerf represents a small portion of the overall impingement area.

It is thus assumed that the gas flow above the workpiece can be approximated by the solution of an axisymmetric impingement problem with the same nozzle operating conditions and the same stand-off distance between the nozzle exit and the workpiece. The resulting stagnation conditions on the workpiece are then used as the inlet conditions for the flow within the kerf. Hence, the jet flow is solved iteratively with the governing equations in the molten layer only for the portion within the kerf and the flow above the workpiece is solved as an independent step in the overall solution strategy.

Oxidation Reactions

The scope of the present study is limited to the laser cutting of low carbon steel (essentially iron) with oxygen as the assist gas. This is by no mean a limitation on the model itself. Other systems can be analyzed simply by replacing the portion of the model that concerns the determination of transport and physical properties as well as adding any additional chemical reactions that may occur.

The oxidation reaction of iron produces three stable oxides: FeO (Wustite), Fe_3O_4 (Magnetite), and Fe_2O_3 (Hematite). The rate at which the oxidation proceeds is, in general, dependent on three physical mechanisms: the mass transfer of oxygen into the molten phase (gas-phase diffusion), diffusion through the iron oxide scale, and the oxidation reaction

rates.

In a typical oxidation process, the thickness of the oxide scale that forms on the surface increases with time. The oxidation process may be rigorous initially, but as the oxide scale thickness increases, the oxidation rate becomes dependent on the diffusion rate of oxygen through the oxide scale. In the case of laser cutting, the oxide scale that forms at the erosion front is constantly removed by the impinging jet. Consequently, the oxidation rate depends only on the gas-phase diffusion and the reaction rates.

In the present study, the oxidation reactions are assumed to be very fast and rate-limited by the gas-phase diffusion of oxygen across the erosion front. The overall reaction at equilibrium (or near-equilibrium) has the following form



and the reaction is highly irreversible (as indicated by its high equilibrium constant) in the temperature range encountered during the laser cutting process.

In the subsequent chapters, the governing equations and the appropriate boundary conditions for each region are presented. Discussions on the physical and transport properties evaluations and on the laser beam characteristics such as spatial variation of the laser beam and laser-material interaction are also included. In addition, details of the $Fe-O_2$ oxidation and how the heat flux due to oxidation is incorporated into the model are described. This is followed by the details of the numerical algorithm adopted in the present study, specifically, the choice for the discretization of the governing equations and the overall solution procedure.

CHAPTER 2. GOVERNING EQUATIONS

The governing equations in the gas and liquid phases are described in this chapter. The choice of nondimensional parameters are also given. In addition, the stress conditions at the gas-liquid interface as well as transport/physical properties and $Fe-O_2$ oxidation reactions are presented.

Gas Phase: Compressible Flow

The rate of momentum transfer from the impinging jet to the molten layer at the erosion front determines the expulsion rate of molten material from the kerf. Thus, the coaxial jet in laser cutting is usually operated at high total pressures. Consequently, the expansion of the deflected jet (or wall jet) can accelerate to supersonic speeds. At the very least, the jet flow will be compressible, even within the kerf. Hence, the appropriate equations for the jet flow would be the Navier-Stokes equations.

The conservation law form of the two-dimensional/axisymmetric Navier-Stokes equations in generalized coordinates using the transformation [34]

$$\tau = t \quad (2.1a)$$

$$\xi = \xi(x, y, t) \quad (2.1b)$$

$$\eta = \eta(x, y, t) \quad (2.1c)$$

can be expressed as

$$\frac{\partial \hat{Q}}{\partial \tau} + \frac{\partial \hat{E}}{\partial \xi} + \frac{\partial \hat{F}}{\partial \eta} = Re^{-1} \left(\frac{\partial \hat{E}_v}{\partial \xi} + \frac{\partial \hat{F}_v}{\partial \eta} \right) + \hat{H} \quad (2.2)$$

where Re is the Reynolds number. The conservative variable vector (\hat{Q}) and the generalized inviscid flux vectors (\hat{E} and \hat{F}) are defined as

$$\hat{Q} = y^k J^{-1} \begin{bmatrix} \rho \\ \rho u \\ \rho v \\ e \end{bmatrix} \quad \hat{E} = y^k J^{-1} \begin{bmatrix} \rho U \\ \rho u U + \xi_x p \\ \rho v U + \xi_y p \\ U(e + p) - \xi_t p \end{bmatrix} \quad \hat{F} = y^k J^{-1} \begin{bmatrix} \rho V \\ \rho u V + \eta_x p \\ \rho v V + \eta_y p \\ V(e + p) - \eta_t p \end{bmatrix}$$

where the Jacobian of the transformation (J) is given by

$$J = \frac{\partial(x, y)}{\partial(\xi, \eta)} \quad (2.3)$$

The contravariant velocities (U and V) are defined as

$$U = \xi_t + \xi_x u + \xi_y v \quad (2.4a)$$

$$V = \eta_t + \eta_x u + \eta_y v \quad (2.4b)$$

The generalized viscous flux vectors (\hat{E}_v and \hat{F}_v) can be expressed as

$$\hat{E}_v = y^k J^{-1} (\xi_x E_v + \xi_y F_v) \quad (2.5a)$$

$$\hat{F}_v = y^k J^{-1} (\eta_x E_v + \eta_y F_v) \quad (2.5b)$$

where

$$E_v = \begin{bmatrix} 0 \\ \tau_{xx} \\ \tau_{xy} \\ f_4 \end{bmatrix} \quad F_v = \begin{bmatrix} 0 \\ \tau_{xy} \\ \tau_{yy} \\ g_4 \end{bmatrix}$$

The components of the stress tensor as well as the definitions of f_4 and g_4 in the above equations are

$$\tau_{xx} = \frac{\mu}{3} \left[4 (\xi_x u_\xi + \eta_x u_\eta) - 2 (\xi_y v_\eta + \eta_y v_\eta) - \frac{2kv}{y} \right] \quad (2.6a)$$

$$\tau_{xy} = \mu (\xi_y u_\eta + \eta_y u_\eta + \xi_x v_\xi + \eta_x v_\eta) \quad (2.6b)$$

$$\tau_{yy} = \frac{\mu}{3} \left[-2 (\xi_x u_\xi + \eta_x u_\eta) + 4 (\xi_y v_\eta + \eta_y v_\eta) - \frac{2kv}{y} \right] \quad (2.6c)$$

$$f_4 = u\tau_{xx} + v\tau_{xy} + \mu Pr^{-1}(\gamma - 1)^{-1} (\xi_x \partial_\xi a^2 + \eta_x \partial_\eta a^2) \quad (2.6d)$$

$$g_4 = u\tau_{xy} + v\tau_{yy} + \mu Pr^{-1}(\gamma - 1)^{-1} (\xi_y \partial_\xi a^2 + \eta_y \partial_\eta a^2) \quad (2.6e)$$

In the preceding equations, the metrics of transformation as well as the velocity gradients have been represented by

$$\frac{\partial \xi}{\partial x} \equiv \xi_x, \quad \frac{\partial u}{\partial x} \equiv u_\xi, \quad \text{etc.}$$

The power k is an index for two types of governing equations with $k = 0$ for two-dimensional flow and $k = 1$ for axisymmetric flow. In the axisymmetric case, x is the axial direction and y is the radial direction in the cylindrical coordinates system. The axisymmetric source term vector (\hat{H}) is defined as

$$\hat{H} = J^{-1} \begin{bmatrix} 0 \\ 0 \\ (p - Re^{-1}\tau_{\theta\theta}) \\ 0 \end{bmatrix} \quad (2.7)$$

where $\tau_{\theta\theta}$ is given as

$$\tau_{\theta\theta} = \frac{\mu}{3} \left[-2(\xi_x u_\xi + \eta_x u_\eta) - 2(\xi_y v_\xi + \eta_y v_\eta) + \frac{4v}{y} \right] \quad (2.8)$$

The choice of nondimensional parameters is arbitrary. In the preceding nondimensionalized system of equations, the nondimensionalized variables t (time), ρ (density), u

and v (velocities), e (total energy), and μ (viscosity) are obtained from

$$t = \frac{\tilde{t}a_\infty}{l} \quad \rho = \frac{\tilde{\rho}}{\rho_\infty} \quad u = \frac{\tilde{u}}{a_\infty} \quad v = \frac{\tilde{v}}{a_\infty} \quad e = \frac{\tilde{e}}{\rho_\infty a_\infty^2} \quad \mu = \frac{\tilde{\mu}}{\mu_\infty}$$

where ρ_∞ , a_∞ , and μ_∞ are the reference density, speed of sound, and viscosity respectively with l as a characteristic length. The tilde notation has been used to indicate the corresponding dimensional variables. Note that the Reynolds number is defined based on a_∞ , i.e.,

$$Re = \frac{\rho_\infty a_\infty l}{\mu_\infty}$$

and therefore the experimental Reynolds number (which is based on u_∞) must be scaled by the Mach number, M_∞ .

Thin-Layer Approximation

In high Reynolds number flows, the effects of viscosity are limited to the region near the wall. Typically in the physical domain, the grid points are clustered in the normal direction but not sufficiently along the wall. Hence, even though the full Navier-Stokes equations are solved, the viscous terms associated with the derivatives along the wall are not properly resolved. However, in most cases where the flow is attached or mildly separated, these derivatives are negligible and can be neglected from the equations altogether [35]. This resulted in the so-called “thin-layer” form of the Navier-Stokes equations. With this approximation, Eqn. 2.2 can be expressed as

$$\frac{\partial \hat{Q}}{\partial \tau} + \frac{\partial \hat{E}}{\partial \xi} + \frac{\partial \hat{F}}{\partial \eta} = Re^{-1} \frac{\partial \hat{S}}{\partial \eta} + \hat{H} \quad (2.9)$$

where the “thin-layer” viscous flux (\hat{S}) is given by

$$\hat{S} = J^{-1} \begin{bmatrix} 0 \\ \eta_x m_1 + \eta_y m_2 \\ \eta_x m_2 + \eta_y m_3 \\ \eta_x (u m_1 + v m_2 + m_4) + \eta_y (u m_2 + v m_3 + m_5) \end{bmatrix} \quad (2.10)$$

with

$$m_1 = \frac{\mu}{3} (4\eta_x u_\eta - 2\eta_y v_\eta) \quad (2.11a)$$

$$m_2 = \mu (\eta_y u_\eta + \eta_x v_\eta) \quad (2.11b)$$

$$m_3 = \frac{\mu}{3} (-2\eta_x u_\eta + 4\eta_y v_\eta) \quad (2.11c)$$

$$m_4 = \mu Pr^{-1} (\gamma - 1)^{-1} \eta_x \partial_\eta (a^2) \quad (2.11d)$$

$$m_5 = \mu Pr^{-1} (\gamma - 1)^{-1} \eta_y \partial_\eta (a^2) \quad (2.11e)$$

The circumferential stress component ($\tau_{\theta\theta}$) in the axisymmetric source term can be simplified to

$$\tau_{\theta\theta} = \frac{\mu}{3} \left[-2\eta_x u_\eta - 2\eta_y v_\eta + \frac{4v}{y} \right] \quad (2.12)$$

Liquid Phase: Incompressible Flow

The fluid dynamics of molten metal has been studied extensively [36–39]. In almost all cases, the molten film is adequately described by assuming incompressible flow. In the present study, the incompressible Navier-Stokes equations are used to model the fluid dynamics of the molten layer. Furthermore, in the presence of laser radiation and coupled with the heat of oxidation reactions, the temperature variation within the molten film may be high enough such that a constant viscosity assumption may not be valid. This is

circumvented by solving the incompressible energy equation for the temperature field from which the viscosity variation can be obtained.

Assuming the same form of transformation to a generalized coordinates as with the governing equations in the gas phase, the nondimensionalized incompressible Navier-Stokes equations in conservation law form are given by

$$\frac{\partial}{\partial \xi} \left(\frac{U}{J} \right) + \frac{\partial}{\partial \eta} \left(\frac{V}{J} \right) = 0 \quad (2.13)$$

$$\frac{\partial}{\partial \tau} (J^{-1} \vec{V}) = -\frac{\partial}{\partial \xi} (\hat{e} - Re^{-1} \hat{e}_v) - \frac{\partial}{\partial \eta} (\hat{f} - Re^{-1} \hat{f}_v) - (J Fr)^{-1} \vec{g} \quad (2.14)$$

$$\frac{\partial}{\partial \tau} (J^{-1} T) + \frac{\partial}{\partial \xi} (J^{-1} UT) + \frac{\partial}{\partial \eta} (J^{-1} VT) = Re^{-1} Pr^{-1} \left(\frac{\partial T^\xi}{\partial \xi} + \frac{\partial T^\eta}{\partial \eta} \right) \quad (2.15)$$

where Re , Fr , Pr , \vec{g} , and \vec{V} are the Reynolds number, the Froude number, the Prandtl number, the gravitational acceleration vector, and the velocity vector respectively. The viscous dissipation terms in the energy equation have been neglected. The generalized flux vectors of the incompressible flow equations can be expressed as

$$\hat{e} = \frac{1}{J} \begin{bmatrix} \xi_x p + uU + \xi_t u \\ \xi_y p + vU + \xi_t v \end{bmatrix} \quad \hat{e}_v = \frac{\mu}{J} \begin{bmatrix} \xi_x \tau_{xx} + \xi_y \tau_{xy} \\ \xi_x \tau_{xy} + \xi_y \tau_{yy} \end{bmatrix}$$

$$\hat{f} = \frac{1}{J} \begin{bmatrix} \eta_x p + uV + \eta_t u \\ \eta_y p + vV + \eta_t v \end{bmatrix} \quad \hat{f}_v = \frac{\mu}{J} \begin{bmatrix} \eta_x \tau_{xx} + \eta_y \tau_{xy} \\ \eta_x \tau_{xy} + \eta_y \tau_{yy} \end{bmatrix}$$

Furthermore, T^ξ and T^η in the energy equation are defined as

$$T^\xi = J^{-1} \mu \left[(\xi_x^2 + \xi_y^2) T_\xi + (\xi_x \eta_x + \xi_y \eta_y) T_\eta \right] \quad (2.16a)$$

$$T^\eta = J^{-1} \mu \left[(\xi_x \eta_x + \xi_y \eta_y) T_\xi + (\eta_x^2 + \eta_y^2) T_\eta \right] \quad (2.16b)$$

In the above equations, the contravariant velocities (U and V) are defined as

$$U = \xi_x u + \xi_y v \quad (2.17a)$$

$$V = \eta_x u + \eta_y v \quad (2.17b)$$

and the incompressible stress tensor components are given by

$$\tau_{xx} = 2\mu(\xi_x u_\xi + \eta_x u_\eta) \quad (2.18a)$$

$$\tau_{xy} = \mu(\xi_y u_\eta + \eta_y u_\xi + \xi_x v_\xi + \eta_x v_\eta) \quad (2.18b)$$

$$\tau_{yy} = 2\mu(\xi_y v_\xi + \eta_y v_\eta) \quad (2.18c)$$

The nondimensionalized values of p , u , v , and μ are given by

$$p = \frac{\tilde{p} - p_r}{\rho_r u_r^2} \quad u = \frac{\tilde{u}}{u_r} \quad v = \frac{\tilde{v}}{u_r} \quad \mu = \frac{\tilde{\mu}}{\mu_r}$$

where p_r , ρ_r , u_r , and μ_r are the reference pressure, density, velocity, and viscosity respectively for the molten layer. Here again, the tilde notation is used to indicate dimensional quantities. The Reynolds number and the Froude number are defined as

$$Re = \frac{\rho_r u_r l}{\mu_r} \quad \text{and} \quad Fr = \frac{u_r^2}{lg}$$

respectively where l is a characteristic length and g is the magnitude of the local gravitational acceleration.

For the rest of this dissertation, the reference to incompressible flow refers to the molten metal flow while the reference to compressible flow refers to the flow of the coaxial gas jet.

Interface Conditions

The interface between the gas and liquid metal (or the erosion front) is considered as a free surface. Although the ratio of gas viscosity to liquid metal viscosity is generally small ($\mathcal{O}(10^{-2})$), the tangential stress on the erosion front may be of the same order of

magnitude as the pressure contribution. However, the normal stress is assumed to be small in comparison with the magnitude of the pressure acting on the erosion front.

Under these assumptions, the stress balance [40] at the free surface can be expressed as

$$p - \frac{2\mu}{Re} \left[n_x^2 \frac{\partial u}{\partial x} + n_x n_y \left(\frac{\partial u}{\partial y} + \frac{\partial v}{\partial x} \right) + n_y^2 \frac{\partial v}{\partial y} \right] = p_g - \frac{\bar{\kappa} \Gamma}{We} \quad (2.19)$$

$$2n_x n_y \mu \left(\frac{\partial u}{\partial x} - \frac{\partial v}{\partial y} \right) + \mu (n_y^2 - n_x^2) \left(\frac{\partial u}{\partial y} + \frac{\partial v}{\partial x} \right) = \tau_{w,g} \quad (2.20)$$

where $\bar{\kappa}$ is the surface curvature, n_x and n_y are the components of the unit normal vector at the free surface, p_g and $\tau_{w,g}$ are the pressure and shearing stress of the impinging coaxial jet at the erosion front, and Γ is the nondimensionalized surface tension coefficient. The Weber number (We) is defined as

$$We = \frac{\rho_r u_r l}{\Gamma_r}$$

where Γ_r is a reference surface tension coefficient.

The kinematic constraint on the surface is such that the fluid particles at the free surface must remain at the free surface. If F is the free surface height—which is a function of both x and t —the condition for the particles on the free surface can be written as

$$\frac{D}{Dt} [F(x, t) - y] = 0 \quad (2.21)$$

It has been assumed that material removal rate through evaporation is small in comparison to the overall rate at which molten material is ejected from the kerf. This is generally true for laser cutting of relatively thick plates where the maximum temperature at the erosion front is usually less than 3000K [41,42]. The critical temperature for mild steels, for instance, is over 3500K.

The energy balance at the erosion front among the heat fluxes due to the laser beam, exothermic heat of oxidation reactions as well as convective and radiative losses can be expressed as

$$k_m \nabla T_m \cdot \hat{n} = q'_R + q'_L + k_g \nabla T_g \cdot \hat{n} - \sigma (T_g^4 - T_{g,\infty}^4) \quad (2.22)$$

where k_m and k_g are the thermal conductivities in the molten metal and gas respectively, σ is Stefan's constant ($5.67 \times 10^{-8} \text{W/m}^2 \cdot \text{K}^4$), \hat{n} is the outward normal vector, and q'_R and q'_L are the heat fluxes due to the oxidation reactions and the laser beam respectively.

Physical Properties

In the present formulation, the governing equations are applicable to the cutting process of any metal with a reactive coaxial gas jet so long as the molten metal obeys the Boussinesq assumption and the gas remains a perfect gas. Therefore, for the purpose of validation and comparison, the laser cutting of low carbon steel (essentially 99.9% iron) with an oxygen jet is chosen as the model case. The transport and physical properties of the molten material are approximated by those for liquid iron. The primary properties which are needed include the coefficient of viscosity, surface tension coefficient, and thermal conductivity, which are all dependent on the temperature of the molten layer.

Liquid Iron

Coefficient of Viscosity The viscosity of molten metals can be obtained from the kinetic theory with an appropriate intermolecular potential function. However, for the present study, a simple exponential representation of viscosity based on experimental data is used. For most liquid metals, the viscosity can be approximated by an Arrhenius type

relationship [43] given by

$$\mu = C \exp\left(\frac{H_\mu}{R_U T}\right) \quad (2.23)$$

where R_U is the universal gas constant and C and H_μ are constants. The constant C is obtained from

$$C = \frac{5.7 \times 10^{-2} (W T_m)^{1/2}}{V_m^{2/3} \exp(H_\mu / R_U T_m)} \quad (2.24)$$

and H_μ is calculated from

$$H_\mu = 1.21 T_m^{1.2} \quad (2.25)$$

where T_m and V_m are the temperature and atomic volume at the melting point, and W is the atomic weight. In the case of liquid iron [44], H_μ is calculated to be 9.9 Kcal/mole and C is calculated to be 0.37 cP (mPa·s). The melting point of iron is 1537°C.

Surface Tension Coefficient The existing surface tension data of molten metals are inconsistent. This is due primarily to the various factors that affect the surface tension. For example, a 0.01% oxygen or 0.005% sulfur impurity in molten iron can cause a 10% reduction in the surface tension value at a temperature of 1550°C [45]. However, these effects are neglected in the present study and the surface tension is assumed to depend only on the surface temperature.

At the critical temperature, the surface between liquid and vapor phase must vanish and the surface tension must approach zero. Accordingly, the van der Waals equation for surface tension can be expressed as [45]

$$\Gamma = \gamma_0 [1 - (T/T_c)]^N \quad (2.26)$$

where γ_0 is a constant and T_c is the critical temperature. The exponent N is given by

$$N = 1 - \frac{2(T_c - T) \partial \rho_L}{3 \rho_L \partial T} \quad (2.27)$$

For liquid iron [45],

$$\gamma_0 = 4.598 \text{ N/m} \quad \text{and} \quad \frac{1}{\rho_L} \frac{\partial \rho_L}{\partial T} = -119 \times 10^{-6} \text{ } ^\circ\text{C}^{-1}$$

Furthermore, the density (ρ_L) and critical temperature (T_c) for liquid iron are approximately 7010 kg/m^3 and 3000°C respectively.

Thermal Conductivity At the present time, few experimental data on the thermal conductivities of liquid metals are available. In addition, the accuracy of measurements for thermal conductivities are relatively poor. However, a simple theoretical relationship [43] exists between electrical and thermal conductivities of solid metals at high temperature¹ such that

$$k = 2.45 \times 10^{-8} \frac{T}{\rho_e} \quad (2.28)$$

where k is the thermal conductivity in $\text{W/m}\cdot\text{K}$, ρ_e is the electric resistivity (reciprocal of electric conductivity). The constant 2.45×10^{-8} is known as the theoretical Lorenz number. Experimental measurements have shown that the Lorenz number remains fairly constant even in the liquid phase. Furthermore, reliable data on electrical conductivities for various liquid metals are available, thus making it possible for the evaluation of liquid metal thermal conductivities. For liquid iron [43], the empirical expression for electric resistivity is given by

$$\rho_e = 1.54 \times 10^{-4} T + 1.081 \quad [\mu\Omega\text{m}] \quad (2.29)$$

Although the resistivity is raised when foreign atoms (such as oxygen in this case) are introduced into the melt, this effect is neglected in the present model.

¹ This equation is known as Wiedemann-Franz-Lorenz Law.

Specific Heat Capacity Accurate data for the heat capacities of liquid metals are not abundant. For most liquid metals the values of heat capacity (C_p) are assumed to be constant over relatively wide ranges of temperature. In general, the influence of temperature on liquid metal heat capacities tends to be small. Hence, for the present model, a constant heat capacity of 41.8 J/mole·K [43] is assumed.

Coaxial Jet

Equation of State The coaxial jet is assumed to behave like a perfect gas. Accordingly, the thermodynamic variables are fully described by the perfect gas equation of state, i.e.,

$$p = \rho RT \quad (2.30)$$

Hence, the pressure p is related to the conservative variable e through

$$p = (\gamma - 1) \left[e - \frac{1}{2}(u^2 + v^2) \right] \quad (2.31)$$

where e is total energy and γ is the ratio of specific heats which is assumed to be 1.4 for air or oxygen.

Coefficient of Viscosity In general, the coefficient of viscosity of fluids varies with temperature and pressure. Since the critical pressures of gases are usually above 10 atm, typical gas flow problems are at low reduced pressures and therefore, the pressure dependence can be ignored.

In the present model, the gas viscosity is assumed to vary with temperature according to Sutherland's Law [46] given as

$$\frac{\mu}{\mu_o} \approx \left(\frac{T}{T_o} \right)^{3/2} \frac{T_o + C_\mu}{T + C_\mu} \quad (2.32)$$

where C_μ is the an effective temperature² which is characteristic of the gas. For oxygen [46], $T_o = 273$ K, $\mu_o = 1.919 \times 10^{-5}$ N·s/m², and $C_\mu = 139$ K. The accuracy is within 2% between 190 K and 2000 K.

Thermal Conductivity The thermal conductivity of gases can be correlated with an expression similar to that for the coefficient of viscosity [46].

$$\frac{k}{k_o} \approx \left(\frac{T}{T_o} \right)^{3/2} \frac{T_o + C_k}{T + C_k} \quad (2.33)$$

For oxygen [46], the Sutherland-law thermal conductivity parameters are $T_o = 273$ K, $k_o = 0.0244$ W/m·K, and $C_k = 240$ K. The accuracy of the correlation is within 2% in the temperature range of 200–1200 K.

Laser Beam Characteristics

The laser beam characteristics that are needed include the spatial variation of the laser power being delivered and the absorption characteristics at the erosion front.

Laser Power The laser beam is assumed to have TEM₀₀ mode. Accordingly, the spatial variation of laser beam density can be described by a Gaussian distribution function given by [47]

$$q'_l(r) = q'' \exp \left[- \left(\frac{r}{r_l} \right)^2 \right] \quad (2.34)$$

where $q'_l(r)$ is the laser heat flux at the radial location r , q'' is the laser power density, and r_l is the radius of the laser beam.

Laser-Material Coupling The presence of shocks and plasma formation in the jet can adversely effect the focusing of the laser beam on the material and other laser beam

² Also called the *Sutherland constant*.

parameters such polarization and beam intensity. These effects are neglected in the present study. Hence, the coupling between the laser radiation and material at the erosion front is determined only by the incident angle such that

$$q'_{ab} = [1 - R(\theta_i)] q'_i \quad (2.35)$$

where q'_{ab} is the absorbed laser heat flux at the erosion front and q'_i is the incident laser heat flux given by Eqn. 2.34. $R(\theta_i)$ is the reflectivity at the erosion front and θ_i is the incident angle between the laser beam and the local outward normal vector at the erosion front. Because of the lack of any data on reflectivity, the values of R used in the present study are approximated by the results obtained by Olsen [48] for a p-polarized CO_2 laser beam striking on the surface of mild steels.

Oxidation Reactions

The heat flux due to the surface oxidation between iron and oxygen, assuming complete oxidation, can be evaluated from

$$q'_R = -(\Delta H_R) \nu J_{O_2} \quad (2.36)$$

where ΔH_R is the heat of formation of the oxide per mole of iron, ν is the stoichiometric ratio of iron to oxygen, and J_{O_2} is the molar flux of oxygen at the erosion front. The oxygen molar flux (moles per unit area and time) is evaluated from

$$J_{O_2} = h_{M,x} \frac{\rho_{O_2}}{W_{O_2}} \quad (2.37)$$

where $h_{M,x}$ is a mass transfer coefficient, ρ_{O_2} is the density of the oxygen jet, and W_{O_2} is the molecular weight of oxygen. The mass transfer coefficient is in turn obtained from the

Sherwood number (Sh) according to

$$h_{M,x} = \frac{Sh_x \mathcal{D}}{x} \quad (2.38)$$

where \mathcal{D} is the self diffusion coefficient of oxygen and x is the distance from the leading edge of the erosion front. As a first approximation, the Sherwood number used in the present study is assumed to resemble that for a flat plate [49]

$$Sh_x = 0.332 Re_x^{1/2} Sc^{1/3} \quad (2.39)$$

where Re_x is the Reynolds number based on the distance x along the erosion front and Sc is the Schmidt number defined as

$$Sc = \frac{\mu}{\rho \mathcal{D}}$$

For the present calculations, a Schmidt number of 0.7868 is obtained based on a reference temperature of 300 K. The diffusivity of oxygen \mathcal{D} has a complex dependency on molecular interaction and collision functions. In the present calculations, \mathcal{D} is obtained from [50]

$$\mathcal{D} = 3.85 \times 10^{-4} \frac{T^{1.5}}{p F_c} \quad (2.40)$$

where T is the temperature in Kelvin, p is the absolute pressure in Pascal, and the collision function F_c is approximated as [50]

$$F_c = 1.76 - 0.332 \log_{10} T \quad (2.41)$$

In principle, the oxidation heat flux can be computed for each of the iron oxide reactions. This, however, would require the modeling of the various oxidation reactions such that the composition of the constituents (or species) that are involved in the reactions can be obtained. Such an undertaking, which would involve the identification of the various

elementary reactions during oxidation, is beyond the level of sophistication intended in the present study. Instead, the composition based on experimental observations by Powell *et al.* [51] is assumed. In their findings for laser cutting of mild steels, FeO accounted for 97.6 percent of the oxides while the remaining 2.4 percent was Fe_2O_3 . Hence in the present calculations, the heat of formation is taken as

$$\Delta H_R = -257.58 \text{ KJ/mol (of iron)}$$

while the stoichiometric ratio (ν) is assumed to be 2.0.

CHAPTER 3. NUMERICAL ALGORITHM

The appropriate discretization of the respective governing equations are presented in this chapter. There are many considerations to weigh when establishing a numerical algorithm for a set of partial differential equations, specifically with regard to the type of scheme (finite-difference or finite-volume) and time integration (implicit or explicit). The merits of each approach have been extensively discussed in the literature and will not be included in this chapter.

The algorithm to be presented is an implicit approximate factorization finite difference scheme. The scheme is first order accurate in time and can be either second or third order accurate in space. The development of the algorithm is presented under two headings: *Temporal Discretization* and *Spatial Discretization*.

Temporal Discretization

The governing equations considered so far has the form given by

$$\frac{\partial \hat{Q}}{\partial \tau} + \frac{\partial \hat{E}}{\partial \xi} + \frac{\partial \hat{F}}{\partial \eta} - Re^{-1} \left(\frac{\partial \hat{E}_v}{\partial \xi} + \frac{\partial \hat{F}_v}{\partial \eta} \right) - \hat{H} = 0 \quad (3.1)$$

where \hat{E} and \hat{F} are the inviscid fluxes, \hat{E}_v and \hat{F}_v are the viscous fluxes while \hat{H} is the source term vector for the axisymmetric case. If the time derivative is replaced by a first

order backward difference, a semi-discrete form of Eqn. 3.1 is given by

$$\frac{\hat{Q}^{n+1} - \hat{Q}^n}{\Delta\tau} + \left[\frac{\partial \hat{E}}{\partial \xi} + \frac{\partial \hat{F}}{\partial \eta} - Re^{-1} \left(\frac{\partial \hat{E}_v}{\partial \xi} + \frac{\partial \hat{F}_v}{\partial \eta} \right) \right]^{n+1} - \hat{H}^{n+1} = 0 \quad (3.2)$$

where the superscript n denotes the time level. Equation 3.2 can be represented by a function with the unknown \hat{Q}^{n+1} , herein taken as $G(\hat{Q}^{n+1}) = 0$. Starting from an initial guess for \hat{Q}^{n+1} , a better estimate can be obtained from the application of Newton-Raphson iteration, i.e.,

$$\left(\frac{\partial \hat{G}}{\partial \hat{Q}} \right)^{n+1,m} \Delta \hat{Q} = -\hat{G}^{n+1,m} \quad (3.3)$$

where the superscript m denotes the iteration level and $\Delta \hat{Q} = (\hat{Q}^{n+1,m+1} - \hat{Q}^{n+1,m})$. The partial derivative of \hat{G} with respect to $\hat{Q}^{n+1,m}$ can be expressed as

$$\left(\frac{\partial \hat{G}}{\partial \hat{Q}} \right) = \Delta\tau^{-1} I + \frac{\partial}{\partial \xi} \frac{\partial \hat{E}}{\partial \hat{Q}} + \frac{\partial}{\partial \eta} \frac{\partial \hat{F}}{\partial \hat{Q}} - Re^{-1} \left(\frac{\partial}{\partial \xi} \frac{\partial \hat{E}_v}{\partial \hat{Q}} + \frac{\partial}{\partial \eta} \frac{\partial \hat{F}_v}{\partial \hat{Q}} \right) - \frac{\partial \hat{H}}{\partial \hat{Q}} \quad (3.4)$$

Artificial Compressibility Method

The temporal discretization presented above is valid as long as the Jacobian $\partial \hat{G} / \partial \hat{Q}$ in Eqn. 3.4 is non-singular. However, this will not be the case for the governing equations in the liquid phase because the continuity equation is uncoupled from the momentum equation. The equations are reproduced here for convenience.

$$\left[\frac{\partial}{\partial \xi} \left(\frac{U}{J} \right) + \frac{\partial}{\partial \eta} \left(\frac{V}{J} \right) \right]^{n+1} = 0 \quad (3.5)$$

$$\frac{\vec{V}^{n+1} - \vec{V}^n}{\Delta\tau} + \left[\frac{\partial}{\partial \xi} (\hat{e} - Re^{-1} \hat{e}_v) + \frac{\partial}{\partial \eta} (\hat{f} - Re^{-1} \hat{f}_v) \right]^{n+1} = 0 \quad (3.6)$$

Hence, if \hat{Q} is defined as $J^{-1}(p, u, v)^t$, the first row in the Jacobian $\partial \hat{G} / \partial \hat{Q}$ will all be zeroes. To circumvent this singularity, an artificial compressibility relation [52–54] is

introduced in place of the continuity equation. This relation is given by

$$\frac{\partial}{\partial \tau'} (J^{-1}p) + \beta \left[\frac{\partial}{\partial \xi} \left(\frac{U}{J} \right) + \frac{\partial}{\partial \eta} \left(\frac{V}{J} \right) \right]^{n+1} = 0 \quad (3.7)$$

where τ' is a pseudo time (i.e., iteration level), β is an artificial compressibility parameter and p is the pressure. The introduction of the pseudo time derivative of pressure essentially removes the singularity by coupling the continuity equation to the momentum equation in the iteration process (or in pseudo time). However, this term does not appear in \hat{G} . Hence, in the combined system,

$$I_m \frac{\hat{Q}^{n+1} - \hat{Q}^n}{\Delta \tau} + \left[\frac{\partial}{\partial \xi} (\hat{E} - Re^{-1} \hat{E}_v) + \frac{\partial}{\partial \eta} (\hat{F} - Re^{-1} \hat{F}_v) \right]^{n+1} = 0 \quad (3.8)$$

where \hat{Q} is the unknown vector ($\hat{Q} = J^{-1}(p, u, v)^t$) and I_m is a modified 3×3 identity matrix with zero as the first diagonal element. The combined flux vectors are given as

$$\hat{E} = \frac{1}{J} \begin{bmatrix} \beta U \\ \xi_x p + uU + \xi_t u \\ \xi_y p + vU + \xi_t v \end{bmatrix} \quad \hat{E}_v = \frac{\mu}{J} \begin{bmatrix} 0 \\ \xi_x \tau_{xx} + \xi_y \tau_{xy} \\ \xi_x \tau_{xy} + \xi_y \tau_{yy} \end{bmatrix}$$

$$\hat{F} = \frac{1}{J} \begin{bmatrix} \beta V \\ \eta_x p + uV + \eta_t u \\ \eta_y p + vV + \eta_t v \end{bmatrix} \quad \hat{F}_v = \frac{\mu}{J} \begin{bmatrix} 0 \\ \eta_x \tau_{xx} + \eta_y \tau_{xy} \\ \eta_x \tau_{xy} + \eta_y \tau_{yy} \end{bmatrix}$$

Spatial Discretization

If the iteration scheme presented as Eqn. 3.3 is convergent, then starting from the previous time step value of \hat{Q} as the initial guess (i.e., $\hat{Q}^{n+1, m=0} = \hat{Q}^n$), the values at the $n + 1$ level would be obtained as the right-hand-side (RHS) of Eqn. 3.3 approaches zero, i.e.,

$$\lim_{m \rightarrow \infty} \hat{G}^{n+1, m} \rightarrow 0 \quad (3.9)$$

Once this has occurred, the value of $\partial\hat{G}/\partial\hat{Q}$ is inconsequential because $\hat{Q}^{n+1,m+1} - \hat{Q}^{n+1,m}$ is zero (or smaller than some specified tolerance). One important implication is that any approximation made in constructing $\partial\hat{G}/\partial\hat{Q}$ (such as due to linearization, omission of various terms or approximate factorization) is also inconsequential as long as the resulting expression remains convergent. Furthermore, the choice for discretizing the left and right hand sides of Eqn. 3.3 need not be the same. This should be evident in the sections that follow.

Spatial Discretization of LHS

As pointed out previously, the discretization of LHS is arbitrary as long as the resulting iterative scheme remains convergent. One approach would be to simply represent the derivatives³ on the LHS by central differences. However, this often leads to unstable schemes unless some form of dissipation is introduced. Alternatively, the derivatives can be represented by upwind differences based on the information provided by the characteristics of the equations. Both approaches are taken in the present study, in particular, the incompressible flow equations are discretized using a central scheme while the compressible flow equations are discretized using an upwind scheme.

Compressible Flow Equations The spatial discretization of the gas phase governing equations utilizes an upwind formulation. Following the Steger-Warming flux vector splitting, a first order discretization of the LHS (i.e., $\partial\hat{G}/\partial\hat{Q}$) is given by

$$\left[\Delta\tau^{-1}I + \nabla_{\xi}\hat{A}^+ + \Delta_{\xi}\hat{A}^- + \nabla_{\eta}\hat{B}^+ + \Delta_{\eta}\hat{B}^- - Re^{-1}J^{-1}(\delta_{\xi}\hat{L} + \delta_{\eta}\hat{M})J \right]^{n+1,m} \quad (3.10)$$

³ It is understood that the viscous derivatives are satisfactorily represented by central differences. It is the inviscid derivatives that provide difficulties in term of determining the stability of the resulting scheme.

with

$$\hat{A}^\pm = \frac{\partial \hat{E}^\pm}{\partial \hat{Q}} \quad \hat{B}^\pm = \frac{\partial \hat{F}^\pm}{\partial \hat{Q}} \quad \hat{L} = \frac{\partial \hat{E}_v}{\partial \hat{Q}} \quad \text{and} \quad \hat{M} = \frac{\partial \hat{F}_v}{\partial \hat{Q}}$$

where ∇ , Δ , and δ are notations for forward, backward, and central differences. Furthermore, the inviscid flux Jacobians are constructed from $\hat{A}^\pm = T_\xi \Lambda_\xi^\pm T_\xi^{-1}$ and $\hat{B}^\pm = T_\eta \Lambda_\eta^\pm T_\eta^{-1}$, where Λ_k is the eigenvalue matrix and T_k and T_k^{-1} are the right and left eigenvector matrices. Note that the Jacobian of the axisymmetric source term vector has been neglected in the formulation. Hence, for the axisymmetric case, the source term vector is added only to the RHS.

Equation 3.10 represents a block penta-diagonal system, and with $\hat{G}^{n+1,m}$, can be solved for the unknown $\Delta \hat{Q}$ at every grid point. A direct inversion⁴ of a block penta-diagonal system would be very expensive in terms of both storage and computation cost. Alternatively, the system of equations can be solved using a line-relaxation method. In this method, the domain is swept in one or two of the two coordinate directions. At each line perpendicular to the sweep direction, a tridiagonal system is formed. For the points not on this line, the implicit matrices on the LHS are multiplied with the latest values of the $\Delta \hat{Q}$ vector, and added to the RHS of the equations. Using this method, the size of the physical time step is bounded by the physical constraints of the problem and not by the numerical stability.

A third alternative method is adopted in the present study. The LHS (Eqn. 3.10) is approximately factorized [55] into two one-dimensional operators such that

$$\Delta \tau \left(\frac{\partial \hat{G}}{\partial \hat{Q}} \right)^{n+1,m} = (\Omega_\xi \Omega_\eta)^{n+1,m} \quad (3.11)$$

⁴ Such as through the use of a strongly implicit procedure (SIP).

where

$$(\Omega_\xi)^{n+1,m} = \left[I + \Delta\tau \left(\nabla_\xi \hat{A}^+ + \Delta_\xi \hat{A}^- - Re^{-1} J^{-1} \delta_\xi \hat{L} J \right) \right]^{n+1,m} \quad (3.12a)$$

$$(\Omega_\eta)^{n+1,m} = \left[I + \Delta\tau \left(\nabla_\eta \hat{B}^+ + \Delta_\eta \hat{B}^- - Re^{-1} J^{-1} \delta_\eta \hat{M} J \right) \right]^{n+1,m} \quad (3.12b)$$

The approximate factorization essentially reduces Eqn. 3.10 to two implicit operators each of which is block tridiagonal. The solution algorithm now consists of two one-dimensional sweeps, one in the ξ and one in the η direction.

For the thin-layer Navier-Stokes equations, the one-dimensional operators, Ω_ξ and Ω_η can be reduced to

$$(\Omega_\xi)^{n+1,m} = \left[I + \Delta\tau \left(\nabla_\xi \hat{A}^+ + \Delta_\xi \hat{A}^- \right) \right]^{n+1,m} \quad (3.13a)$$

$$(\Omega_\eta)^{n+1,m} = \left[I + \Delta\tau \left(\nabla_\eta \hat{B}^+ + \Delta_\eta \hat{B}^- - Re^{-1} J^{-1} \delta_\eta \hat{M} J \right) \right]^{n+1,m} \quad (3.13b)$$

where the viscous Jacobian \hat{M} is now defined as

$$\hat{M} = \frac{\partial \hat{S}}{\partial \hat{Q}} \quad (3.14)$$

Incompressible Flow Equations The discretization of the governing equations in the liquid phase proceeds in a similar way but with central differences instead of upwind representations. Hence, the LHS for the liquid phase equations, after the approximate factorization, becomes

$$\Delta\tau \left(\frac{\partial \hat{G}}{\partial \hat{Q}} \right)^{n+1,m} = (\Omega_\xi \Omega_\eta)^{n+1,m} \quad (3.14)$$

where

$$(\Omega_\xi)^{n+1,m} = \left[I + \Delta\tau \left(\delta_\xi \hat{A} - Re^{-1} J^{-1} \delta_\xi \hat{L} J \right) \right]^{n+1,m} \quad (3.15a)$$

$$(\Omega_\eta)^{n+1,m} = \left[I + \Delta\tau \left(\delta_\eta \hat{B} - Re^{-1} J^{-1} \delta_\eta \hat{M} J \right) \right]^{n+1,m} \quad (3.15b)$$

and \hat{A} , \hat{B} , \hat{L} , and \hat{M} are the Jacobian matrices of the modified incompressible Navier-Stokes equation. The energy equation is similarly discretized and factorized to yield two scalar tridiagonal systems in the ξ and η directions.

Spatial Discretization of RHS

Since it is the discretized form of $\hat{G}^{n+1,m}$ in Eqn. 3.3 that is actually driven to zero at each time level, it is desirable to evaluate $\hat{G}^{n+1,m}$ as accurately as possible. Although first order discretizations are available, the accuracy provided is not sufficient for a typical grid points distribution. Therefore, second order or higher discretization is used in the present study.

Compressible Flow Equations As mentioned previously, an upwind formulation for the RHS is adopted in the present development for the inviscid terms. In particular, Roe's flux-difference splitting scheme is used. The viscous terms are represented using central differences. The details of Roe's scheme for the inviscid terms are shown for the terms in the ξ direction. The same procedure is similarly applied to the terms in the η direction.

The partial derivative of the inviscid flux \hat{E} can be represented (with $\Delta\xi = 1$) by

$$\frac{\partial \hat{E}}{\partial \xi} = \hat{E}_{i+\frac{1}{2}} - \hat{E}_{i-\frac{1}{2}} \quad (3.16)$$

As in the Steger-Warming flux vector splitting, the flux at a face is split according to its eigenvalues, for example,

$$\hat{E}_{i+\frac{1}{2}} = \hat{E}_{i+\frac{1}{2}}^+ + \hat{E}_{i+\frac{1}{2}}^- \quad (3.17)$$

For a 1st order upwind scheme, the fluxes are evaluated as

$$\hat{E}_{i+\frac{1}{2}}^+ = \hat{E}_i^+ \quad \text{and} \quad \hat{E}_{i+\frac{1}{2}}^- = \hat{E}_{i+1}^-$$

and Eqn. 3.17 can be expressed as

$$\hat{E}_{i+\frac{1}{2}} = \frac{1}{2} (\hat{E}_i + \hat{E}_{i+1}) + \frac{1}{2} \Delta \hat{E}_{i+\frac{1}{2}}^- - \frac{1}{2} \Delta \hat{E}_{i+\frac{1}{2}}^+ \quad (3.18)$$

where the flux differences are defined as

$$\Delta \hat{E}_{i+\frac{1}{2}}^+ = \hat{E}_{i+1}^+ - \hat{E}_i^+ \quad (3.19a)$$

$$\Delta \hat{E}_{i+\frac{1}{2}}^- = \hat{E}_{i+1}^- - \hat{E}_i^- \quad (3.19b)$$

In a smooth region (i.e., delimited by the i and $i + 1$ grid points), the flux differences can be evaluated simply through Eqns. 3.19a and 3.19b. However, if the region contains a discontinuity, the flux differences must be evaluated from the solutions of a Riemann problem. Otherwise, non-physical discontinuities may exist in the final solution. But unfortunately, the solution of the Riemann problem is tedious even for one dimensional flow equations. Hence, approximate solutions (such as by Osher [56] and by Roe [57]) have been proposed.

In the present study, Roe's scheme is adopted. Accordingly, the flux differences are evaluated from

$$\Delta \hat{E}_{i+\frac{1}{2}}^\pm = \hat{A}_{i+\frac{1}{2}}^\pm (\hat{Q}_{i+1} - \hat{Q}_i) \quad (3.20)$$

where $\hat{A}_{i+\frac{1}{2}}^\pm$ is constructed using Roe-averaged variables defined as

$$\rho_{i+\frac{1}{2}} = \sqrt{\rho_{i+1} \rho_i} \quad (3.21a)$$

$$u_{i+\frac{1}{2}} = \frac{\sqrt{\rho_{i+1}} u_{i+1} + \sqrt{\rho_i} u_i}{\beta} \quad (3.21b)$$

$$v_{i+\frac{1}{2}} = \frac{\sqrt{\rho_{i+1}} v_{i+1} + \sqrt{\rho_i} v_i}{\beta} \quad (3.21c)$$

$$(h_T)_{i+\frac{1}{2}} = \frac{\sqrt{\rho_{i+1}} (h_T)_{i+1} + \sqrt{\rho_i} (h_T)_i}{\beta} \quad (3.21d)$$

with $\beta = \sqrt{\rho_{i+1}} + \sqrt{\rho_i}$.

The 1st order scheme above amounts to representing the flux by a piecewise constant within an interval between any two adjacent faces. Hence, a linear piecewise representation of the flux would lead to a 2nd order flux at the face, while a quadratic piecewise representation would lead to a third order flux at the face. This idea of constructing an expression for the flux within the interval and evaluating the expression at the extrema of the interval is known as the MUSCL⁵ approach. Thus in the present upwind scheme, higher order representations of $\hat{E}_{i+\frac{1}{2}}^+$ and $\hat{E}_{i+\frac{1}{2}}^-$ are given by

$$\hat{E}_{i+\frac{1}{2}}^+ = \hat{E}_i^+ + \frac{1}{4} \left[(1 - \kappa) \Delta \hat{E}_{i-\frac{1}{2}}^+ + (1 + \kappa) \Delta \hat{E}_{i+\frac{1}{2}}^+ \right] \quad (3.22a)$$

$$\hat{E}_{i+\frac{1}{2}}^- = \hat{E}_{i+1}^- - \frac{1}{4} \left[(1 + \kappa) \Delta \hat{E}_{i+\frac{1}{2}}^- + (1 - \kappa) \Delta \hat{E}_{i+\frac{3}{2}}^- \right] \quad (3.22b)$$

In the above expressions, the face values can be viewed as a combination of backward and forward extrapolations. The value of κ determines the order of the extrapolation. In particular, $\kappa = -1$ corresponds to a linear one-sided extrapolation at the face from two grid points in the upwind direction, leading to a second order fully one-sided scheme such that

$$\hat{E}_{i+\frac{1}{2}}^+ = \hat{E}_i^+ + \frac{1}{2} \Delta \hat{E}_{i-\frac{1}{2}}^+ \quad (3.23a)$$

$$\hat{E}_{i+\frac{1}{2}}^- = \hat{E}_{i+1}^- - \frac{1}{2} \Delta \hat{E}_{i+\frac{3}{2}}^- \quad (3.23b)$$

and Eqn. 3.17 becomes

$$\hat{E}_{i+\frac{1}{2}} = \frac{1}{2} (\hat{E}_{i+1} + \hat{E}_i) + \frac{1}{2} (\Delta \hat{E}_{i-\frac{1}{2}}^+ - \Delta \hat{E}_{i+\frac{1}{2}}^+ + \Delta \hat{E}_{i+\frac{1}{2}}^- - \Delta \hat{E}_{i+\frac{3}{2}}^-) \quad (3.24)$$

For $\kappa = \frac{1}{3}$, $\hat{E}_{i+\frac{1}{2}}^+$ and $\hat{E}_{i+\frac{1}{2}}^-$ are given by

$$\hat{E}_{i+\frac{1}{2}}^+ = \hat{E}_i^+ + \frac{1}{6} \Delta \hat{E}_{i-\frac{1}{2}}^+ + \frac{1}{3} \Delta \hat{E}_{i+\frac{1}{2}}^+ \quad (3.25a)$$

$$\hat{E}_{i+\frac{1}{2}}^- = \hat{E}_{i+1}^- - \frac{1}{3} \Delta \hat{E}_{i+\frac{1}{2}}^- - \frac{1}{6} \Delta \hat{E}_{i+\frac{3}{2}}^- \quad (3.25b)$$

⁵ Monotonic Upstream-centred Schemes for Conservation Laws.

and Eqn. 3.17, with the above expressions, becomes

$$\hat{E}_{i+\frac{1}{2}} = \frac{1}{2} (\hat{E}_{i+1} + \hat{E}_i) + \frac{1}{6} (\Delta \hat{E}_{i-\frac{1}{2}}^+ - \Delta \hat{E}_{i+\frac{1}{2}}^+ + \Delta \hat{E}_{i+\frac{1}{2}}^- - \Delta \hat{E}_{i+\frac{3}{2}}^-) \quad (3.26)$$

This scheme is referred to as the 3rd order upwind biased scheme. Note that the only difference between Eqn. 3.24 and Eqn. 3.26 is in the coefficient of the flux differences.

It is observed that 2nd and higher orders upwind schemes are not sufficient to avoid the appearance of oscillations about discontinuities in the flow solution. One approach for removing the oscillations is to limit the *gradients* or here, the flux differences in the extrapolations, i.e.,

$$\hat{E}_{i+\frac{1}{2}}^+ = \hat{E}_i^+ + \frac{1}{4} \left[(1 - \kappa) \psi \left(r_{i-\frac{1}{2}}^+ \right) \Delta \hat{E}_{i-\frac{1}{2}}^+ + (1 + \kappa) \psi \left(r_{i+\frac{1}{2}}^- \right) \Delta \hat{E}_{i+\frac{1}{2}}^+ \right] \quad (3.27a)$$

$$\hat{E}_{i+\frac{1}{2}}^- = \hat{E}_{i+1}^- - \frac{1}{4} \left[(1 + \kappa) \psi \left(s_{i+\frac{1}{2}}^+ \right) \Delta \hat{E}_{i+\frac{1}{2}}^- + (1 - \kappa) \psi \left(s_{i+\frac{3}{2}}^- \right) \Delta \hat{E}_{i+\frac{3}{2}}^- \right] \quad (3.27b)$$

where r^\pm and s^\pm are flux ratios defined as

$$r_{i-\frac{1}{2}}^+ = \frac{\langle \Delta \hat{E}_{i-\frac{1}{2}}^+, \Delta \hat{E}_{i+\frac{1}{2}}^+ \rangle}{\langle \Delta \hat{E}_{i-\frac{1}{2}}^+, \Delta \hat{E}_{i-\frac{1}{2}}^+ \rangle} \quad r_{i+\frac{1}{2}}^- = \frac{\langle \Delta \hat{E}_{i+\frac{1}{2}}^+, \Delta \hat{E}_{i-\frac{1}{2}}^- \rangle}{\langle \Delta \hat{E}_{i+\frac{1}{2}}^+, \Delta \hat{E}_{i+\frac{1}{2}}^+ \rangle} \quad (3.28a)$$

and

$$s_{i+\frac{1}{2}}^+ = \frac{\langle \Delta \hat{E}_{i+\frac{1}{2}}^-, \Delta \hat{E}_{i+\frac{3}{2}}^- \rangle}{\langle \Delta \hat{E}_{i+\frac{1}{2}}^-, \Delta \hat{E}_{i+\frac{1}{2}}^- \rangle} \quad s_{i+\frac{3}{2}}^- = \frac{\langle \Delta \hat{E}_{i+\frac{3}{2}}^-, \Delta \hat{E}_{i+\frac{1}{2}}^- \rangle}{\langle \Delta \hat{E}_{i+\frac{3}{2}}^-, \Delta \hat{E}_{i+\frac{3}{2}}^- \rangle} \quad (3.28b)$$

where $\langle \rangle$ denotes the scalar product of the flux difference vector and $\psi(a)$ is a TVD limiter.

The choice for $\psi(a)$ in the present study is Roe's Superbee Limiter defined as

$$\psi(a) = \max[0, \min(2a, 1), \min(a, 2)] \quad (3.29)$$

Hence, for the 2nd order scheme, the TVD flux at the face becomes

$$\begin{aligned} \hat{E}_{i+\frac{1}{2}} = & \frac{1}{2} (\hat{E}_i + \hat{E}_{i+1}) - \frac{1}{2} \Delta \hat{E}_{i+\frac{1}{2}}^+ + \frac{1}{2} \Delta \hat{E}_{i+\frac{1}{2}}^- + \\ & \frac{1}{2} \psi \left(r_{i-\frac{1}{2}}^+ \right) \Delta \hat{E}_{i-\frac{1}{2}}^+ - \frac{1}{2} \psi \left(s_{i+\frac{3}{2}}^- \right) \Delta \hat{E}_{i+\frac{3}{2}}^- \end{aligned} \quad (3.30)$$

while for the 3rd order upwind biased scheme, the TVD flux is given by

$$\begin{aligned} \hat{E}_{i+\frac{1}{2}} = & \frac{1}{2} (\hat{E}_i + \hat{E}_{i+1}) - \frac{1}{2} \Delta \hat{E}_{i+\frac{1}{2}}^+ + \frac{1}{2} \Delta \hat{E}_{i+\frac{1}{2}}^- + \frac{1}{3} \psi(r_{i+\frac{1}{2}}^-) \Delta \hat{E}_{i+\frac{1}{2}}^+ + \\ & \frac{1}{6} \psi(r_{i-\frac{1}{2}}^+) \Delta \hat{E}_{i-\frac{1}{2}}^+ - \frac{1}{3} \psi(s_{i+\frac{1}{2}}^+) \Delta \hat{E}_{i+\frac{1}{2}}^- - \frac{1}{6} \psi(s_{i+\frac{3}{2}}^-) \Delta \hat{E}_{i+\frac{1}{2}}^- \end{aligned} \quad (3.31)$$

Similar expressions can be obtained for $\hat{E}_{i-\frac{1}{2}}$.

The viscous terms are evaluated using central differences, for example,

$$\frac{\partial \hat{E}_v}{\partial \xi} = (\hat{E}_v)_{i+\frac{1}{2}} - (\hat{E}_v)_{i-\frac{1}{2}} \quad (3.32)$$

In evaluating both the inviscid and viscous terms on the RHS, all metrics terms are calculated using arithmetic averages between the grid points.

Incompressible Flow Equations Consistent with the formulation on the LHS, central differences are used to represent both the inviscid and viscous flux derivatives in the RHS.

Accordingly,

$$\frac{\partial \hat{E}}{\partial \xi} = \frac{1}{2} (\hat{E}_{i+1} - \hat{E}_{i-1}) \quad (3.33)$$

$$\frac{\partial \hat{E}_v}{\partial \xi} = (\hat{E}_v)_{i+\frac{1}{2}} - (\hat{E}_v)_{i-\frac{1}{2}} \quad (3.34)$$

The primitive variables as well as the metrics at the face are calculated using arithmetic averages between the delimiting grid points.

In order to ensure stability, the following constant coefficient 4th order artificial dissipation is added to the discretized form of RHS.

$$- \epsilon \Delta \tau J^{-1} [(\nabla_\xi \Delta_\xi)^2 + (\nabla_\eta \Delta_\eta)^2] J \hat{Q}^{n+1,m} \quad (3.35)$$

The parameter ϵ is chosen to be order $\mathcal{O}(1)$. A similar central difference scheme is used for discretizing the RHS of the energy equation.

Inviscid and Viscous Jacobians

To complete the discretization of the governing equations, the flux Jacobians on the LHS of Eqn. 3.3 need to be defined.

Compressible Flow Equations

The similarity transformation of the inviscid flux Jacobians in Eqn. 3.10 are

$$\hat{A}^{\pm} = T_{\xi} \Lambda_{\xi}^{\pm} T_{\xi}^{-1} \quad \text{and} \quad \hat{B}^{\pm} = T_{\eta} \Lambda_{\eta}^{\pm} T_{\eta}^{-1}$$

where

$$\Lambda_{\xi} = \text{diag} \left[U, U, U + a\sqrt{\xi_x^2 + \xi_y^2}, U - a\sqrt{\xi_x^2 + \xi_y^2} \right] \quad (3.36a)$$

$$\Lambda_{\eta} = \text{diag} \left[V, V, V + a\sqrt{\eta_x^2 + \eta_y^2}, V - a\sqrt{\eta_x^2 + \eta_y^2} \right] \quad (3.36b)$$

with

$$T_{\kappa} = \begin{bmatrix} 1 & 0 & \alpha & \alpha \\ u & \tilde{\kappa}_y \rho & \alpha(u + \tilde{\kappa}_x a) & \alpha(u - \tilde{\kappa}_x a) \\ v & -\tilde{\kappa}_x \rho & \alpha(v + \tilde{\kappa}_y a) & \alpha(v - \tilde{\kappa}_y a) \\ \frac{\phi^2}{\gamma-1} & \rho(\tilde{\kappa}_y u - \tilde{\kappa}_x v) & \alpha \left[\frac{\phi^2 + a^2}{\gamma-1} + a\tilde{\theta} \right] & \alpha \left[\frac{\phi^2 + a^2}{\gamma-1} - a\tilde{\theta} \right] \end{bmatrix} \quad (3.37a)$$

and

$$T_{\kappa}^{-1} = \begin{bmatrix} (1 - \phi^2/a^2) & (\gamma-1)u/a^2 & (\gamma-1)v/a^2 & -(\gamma-1)/a^2 \\ -(\tilde{\kappa}_y u - \tilde{\kappa}_x v)/\rho & \tilde{\kappa}_x/\rho & -\tilde{\kappa}_x/\rho & 0 \\ \beta(\phi^2 - a\tilde{\theta}) & \beta[\tilde{\kappa}_x a - (\gamma-1)u] & \beta[\tilde{\kappa}_y a - (\gamma-1)v] & \beta(\gamma-1) \\ \beta(\phi^2 + a\tilde{\theta}) & -\beta[\tilde{\kappa}_x a + (\gamma-1)u] & -\beta[\tilde{\kappa}_y a + (\gamma-1)v] & \beta(\gamma-1) \end{bmatrix} \quad (3.37b)$$

In the above, $\alpha = (\sqrt{2}a)^{-1}\rho$, $\beta = (\sqrt{2}\rho a)^{-1}$, $\tilde{\theta} = \bar{\kappa}_x u + \bar{\kappa}_y v$, $\bar{\kappa}_x = \kappa_x / \sqrt{\kappa_x^2 + \kappa_y^2}$, $\bar{\kappa}_y = \kappa_y / \sqrt{\kappa_x^2 + \kappa_y^2}$, and $\phi^2 = \frac{1}{2}(u^2 + v^2)$. The symbol κ is the general representation of either ξ or η depending on \hat{A} or \hat{B} .

The exact viscous Jacobians would result in a nine-point finite difference stencil at a given grid point due to the cross derivative terms in the viscous flux. One option is to actually neglect the viscous Jacobians in the LHS. This formulation is still convergent but it degrades the convergence rate during subiteration. A second option (and the one used in the present scheme) is to approximate the viscous Jacobians. In this approximation, only the streamwise terms in the viscous Jacobians are retained. This approximation amounts to using the exact viscous Jacobians for the thin-layer Navier-Stokes equations. The result is a convenient five-point stencil instead of the nine-point stencil.

The general form of the thin-layer Navier-Stokes viscous Jacobian is

$$\hat{L} \quad \text{or} \quad \hat{M} = \begin{bmatrix} 0 & 0 & 0 & 0 \\ m_{21} & \alpha_1 \partial_\kappa(\rho^{-1}) & \alpha_1 \partial_\kappa(\rho^{-1}) & 0 \\ m_{31} & \alpha_2 \partial_\kappa(\rho^{-1}) & \alpha_3 \partial_\kappa(\rho^{-1}) & 0 \\ m_{41} & m_{42} & m_{43} & m_{44} \end{bmatrix} \quad (3.38)$$

where

$$m_{21} = -\alpha_1 \partial_\kappa(u/\rho) - \alpha_2 \partial_\kappa(v/\rho) \quad (3.39a)$$

$$m_{31} = -\alpha_2 \partial_\kappa(u/\rho) - \alpha_3 \partial_\kappa(v/\rho) \quad (3.39b)$$

$$m_{41} = \alpha_4 \partial_\kappa \left[-(e/\rho^2) + (u^2 + v^2)/\rho \right] - \alpha_1 \partial_\kappa(u^2/\rho) - 2\alpha_2 \partial_\kappa(uv/\rho) - \alpha_3 \partial_\kappa(v^2/\rho) \quad (3.39c)$$

$$m_{42} = -\alpha_4 \partial_\kappa(u/\rho) - m_{21} \quad (3.39d)$$

$$m_{43} = -\alpha_4 \partial_\kappa(v/\rho) - m_{31} \quad (3.39e)$$

$$m_{44} = \alpha_4 \partial_\kappa (\rho^{-1}) \quad (3.39f)$$

and

$$\alpha_1 = \mu \left[(4/3) \kappa_x^2 + \kappa_y^2 \right] \quad \alpha_2 = (\mu/3) \kappa_x \kappa_y \quad (3.39g)$$

$$\alpha_3 = \mu \left[\kappa_x^2 + (4/3) \kappa_y^2 \right] \quad \alpha_4 = \gamma \mu P r^{-1} (\kappa_x^2 + \kappa_y^2) \quad (3.39h)$$

Similarly, the symbol κ is the general representation for either ξ or η depending on \hat{L} or \hat{M} .

Incompressible Flow Equations

In the liquid phase, the general form of the Jacobian for the inviscid flux is

$$\hat{A} \quad \text{or} \quad \hat{B} = \begin{bmatrix} 0 & \beta \kappa_x & \beta \kappa_y \\ \kappa_x & \kappa_x u + \theta + \kappa_t & \kappa_y u \\ \kappa_y & \kappa_x v & \kappa_y v + \theta + \kappa_t \end{bmatrix} \quad (3.40)$$

where θ is the contravariant velocity (defined as $\kappa_x u + \kappa_y v$) and the symbol κ is used similarly as in the gas phase to indicate either \hat{A} or \hat{B} . Since a central difference scheme is used for the liquid phase, the similarity transformation of the above Jacobian is not required.

The exact viscous Jacobians would again result in a nine-point finite difference stencil. To retain the five-point stencil, only the appropriate streamwise terms in the viscous Jacobians are retained in Ω_ξ and Ω_η . This approximation resulted in the following general expression for the viscous Jacobians,

$$\hat{L} \quad \text{or} \quad \hat{M} = \begin{bmatrix} 0 & 0 & 0 \\ 0 & \alpha_1 \partial_\kappa & \alpha_2 \partial_\kappa \\ 0 & \alpha_2 \partial_\kappa & \alpha_3 \partial_\kappa \end{bmatrix} \quad (3.41)$$

where

$$\alpha_1 = \mu (2\kappa_x^2 + \kappa_y^2) \quad \alpha_2 = \mu \kappa_x \kappa_y \quad \alpha_3 = \mu (\kappa_x^2 + 2\kappa_y^2) \quad (3.42)$$

The derivatives of the heat diffusion terms in the RHS of the energy equation are developed in a similar manner.

Implementation of Boundary Conditions

Because of the variety of boundary conditions to be considered in the present study, the boundary conditions are treated explicitly in the numerical algorithm. The implementation of these boundaries conditions are described briefly in this section.

Free Surface Conditions

The liquid-gas interface conditions which were presented in Chapter 3 can be expressed⁶ in the generalized coordinates as

$$\bar{A} \frac{\partial \vec{V}}{\partial \xi} + \bar{B} \frac{\partial \vec{V}}{\partial \eta} = J^{-1} \bar{R} \quad (3.43)$$

$$p = p_g - \frac{2\mu}{Re} \frac{\partial u_n}{\partial n} - \frac{\bar{\kappa}}{We} \quad (3.44)$$

where

$$\begin{aligned} \frac{\partial u_n}{\partial n} = & (\xi_x n_x^2 + \xi_y n_x n_y) \frac{\partial u}{\partial \xi} + (\eta_x n_x^2 + \eta_y n_x n_y) \frac{\partial u}{\partial \eta} + \\ & (\xi_x n_x n_y + \xi_y n_y^2) \frac{\partial v}{\partial \xi} + (\eta_x n_x n_y + \eta_y n_y^2) \frac{\partial v}{\partial \eta} \end{aligned} \quad (3.45)$$

and the coefficient matrices \bar{A} and \bar{B} are defined as

$$\bar{A} \quad \text{or} \quad \bar{B} = \begin{bmatrix} \kappa_x & \kappa_y \\ 2\kappa_x n_x n_y + \kappa_y (n_y^2 + n_x^2) & \kappa_x (n_y^2 + n_x^2) - 2\kappa_y n_x n_y \end{bmatrix} \quad (3.46)$$

⁶ The continuity equation is solved along with the stress balance equations.

The source in Eqn. 3.43 is defined as $\vec{R} = (0, \tau_{w,g})^t$. Again, the general notation of κ is used to represent ξ or η depending on \vec{A} or \vec{B} .

In the discretization, Eqn. 3.43 is approximated using central difference for the ξ derivative term and first order backward difference for the η derivative term. Similarly in Eqn. 3.44, central differences are used to represent the partial derivatives with respect to ξ and first order backward differences are used for the partial derivatives with respect to η . In the solution procedure, the velocity vector at the free surface \vec{V} is obtained from solving Eqn. 3.43. The pressure at the free surface is then updated using Eqn. 3.44 with the latest values of \vec{V} , p_g , and $\bar{\kappa}$.

The location of the free surface (F) is updated in an explicit manner after the velocity vector at the free surface has been calculated. The semi-discrete form of the kinematic condition can be expressed as

$$F^{n+1} = F^n + \Delta\tau \left[v - u \left(\xi_x \frac{\partial F}{\partial \xi} \right) \right] \quad (3.47)$$

Again, central difference is used to discretize the derivative with respect to ξ .

The interface energy balance, upon transformation to the generalized coordinates, can be expressed as

$$(n_x \xi_x + n_y \xi_y) \frac{\partial T}{\partial \xi} + (n_x \eta_x + n_y \eta_y) \frac{\partial T}{\partial \eta} = S \quad (3.48)$$

where S is the source term that includes the convective and radiative heat losses as well as the heat fluxes due to oxidation reactions and the laser beam. The derivatives are discretized using central difference in the ξ direction and first order backward difference in the η direction.

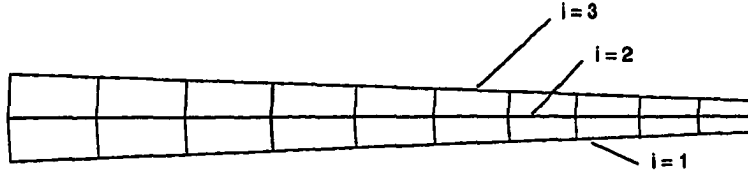


Figure 3.1: Implementation of symmetry boundary conditions by reflecting the $i = 3$ line about the symmetry line $i = 2$

Symmetry/Periodic Conditions

In the present study, symmetry and periodic boundary conditions are encountered in the ξ direction only. For a symmetry boundary, the computational domain is extended one line beyond the symmetry line ($i = 2$) by reflecting the $i = 3$ line about the symmetry line as shown in Fig. 3.1.

At a constant η line, the block tridiagonal equation for a grid point ($i = 2$) on the symmetry line can be written as

$$\hat{L}_{2,j}\Delta\hat{Q}_{1,j} + \hat{D}_{2,j}\Delta\hat{Q}_{2,j} + \hat{U}_{2,j}\Delta\hat{Q}_{3,j} = \hat{R}_{2,j} \quad (3.49)$$

where $\hat{L}_{2,j}$, $\hat{D}_{2,j}$, and $\hat{U}_{2,j}$ are the lower, diagonal, and upper matrices while $\hat{R}_{2,j}$ is the RHS vector. If the symmetry line coincides with the x axis,

$$\Delta\hat{Q}_{1,j} = N\Delta\hat{Q}_{3,j} \quad (3.50)$$

where N is a diagonal matrix defined as

$$N = \text{diag}[1, 1, -1, 1]$$

Hence, the block tridiagonal equation for $i = 2$ becomes

$$\hat{D}\Delta\hat{Q}_{2,j} + (\hat{L}_{2,j}N + \hat{U}_{2,j})\Delta\hat{Q}_{3,j} = \hat{R}_{2,j} \quad (3.51)$$

which can now, along with the block tridiagonal equations of the interior points, be solved with a tridiagonal solver.

For periodic boundary (say at $i = 1$), the block tridiagonal equation at $i = 1$ can be written as

$$\hat{L}_{1,j}\Delta\hat{Q}_{I,j} + \hat{D}_{1,j}\Delta\hat{Q}_{1,j} + \hat{U}_{1,j}\Delta\hat{Q}_{2,j} = \hat{R}_{1,j} \quad (3.52)$$

where I is the number of grid points in the ξ direction. Since $\Delta\hat{Q}_{I,j}$ also appears in the block tridiagonal equation for the $i = I$ point, the tridiagonal system becomes a periodic system and the whole system for a constant η line is solved using a periodic block tridiagonal solver.

Inflow/Outflow Conditions

For subsonic compressible flow, the locally one dimensional Riemann invariants are used at the inlet and outlet boundaries. The invariants given in terms of the normal velocity component are

$$R_1 = V_n - \frac{2a}{\gamma - 1} \quad (3.53a)$$

$$R_2 = V_n + \frac{2a}{\gamma - 1} \quad (3.53b)$$

associated with the characteristic velocities $\lambda_1 = V_n - a$ and $\lambda_2 = V_n + a$ respectively. For a subsonic inlet, $\lambda_2 > 0$ and therefore R_2 is specified as a physical condition. The numerical condition is provided by extrapolating R_1 from the interior of the domain. Hence, at the

inlet boundary, V_n and a are obtained from

$$V_n = \frac{1}{2}(R_1 + R_2) \quad (3.54a)$$

$$a = \frac{1}{4}(\gamma - 1)(R_1 - R_2) \quad (3.54b)$$

Two other physical conditions needed to fully defined the conditions at the inlet are obtained by specifying the tangential velocity V_t and entropy⁷ S . To ensure that total freestream enthalpy is conserved, Eqn. 3.54b is replaced with

$$h_{T,\infty} = \frac{a}{\gamma - 1} + \frac{1}{2}V_n^2 \quad (3.55)$$

where $h_{T,\infty}$ is the freestream total enthalpy. For supersonic inlets, all conditions are specified.

For subsonic outflow, $\lambda_1 < 0$ so R_1 is fixed while R_2 , V_t , and S are extrapolated from the interior. In the present implementation, R_1 is replaced by specifying the exit pressure. In the case where the flow is supersonic, the boundary conditions at the exit are extrapolated from the interior domain.

For incompressible flow calculations, the inlet conditions are established by fixing p_T (total pressure) and V_t . The static pressure is extrapolated from the interior. In the outflow, V_t and V_n are extrapolated from the interior and the static pressure is fixed to a known exit pressure.

Wall Conditions

For a rigid wall, tangency must be satisfied for inviscid flow and the no slip condition for viscous flow. In the present study, the surface is always mapped to a constant η line. The

⁷ Here, the entropy is defined as $\ln(p/\rho^\gamma)$.

Cartesian velocity vector on the surface is related to the normal and tangential components by

$$\begin{pmatrix} u \\ v \end{pmatrix} = \frac{1}{\sqrt{\eta_x^2 + \eta_y^2}} \begin{bmatrix} \eta_y & \eta_x \\ -\eta_x & \eta_y \end{bmatrix} \begin{pmatrix} V_t \\ V_n \end{pmatrix} \quad (3.56)$$

For inviscid flow calculations, V_t is extrapolated from the interior of the computational domain while V_n is set to zero. In the viscous case, both V_t and V_n are set to zero.

The pressure on the wall is obtained by imposing the boundary layer approximation for the normal momentum equation, namely,

$$\frac{\partial p}{\partial n} \approx 0 \quad (3.57)$$

For an adiabatic wall, the normal density gradient is set to zero and for a constant temperature wall, the density at the wall is calculated from the equation of state.

Overall Solution Procedure

The schematic diagram of the overall solution procedure is illustrated in Fig. 3.2. The various steps can be summarized as follow:

1. The total pressure and total density distributions on the workpiece surface are obtained by solving the axisymmetric jet impingement problem with the specified operating conditions and stand-off distance for the nozzle. The total pressure and total density distributions are used as inlet boundary conditions for the jet flow within the kerf.
2. The solutions in the molten layer and the jet flow within kerf are obtained in an iterative process. An initial profile for the erosion front is assumed and based on this profile, the solution in the gas jet is obtained and used as the starting solution in the iteration.

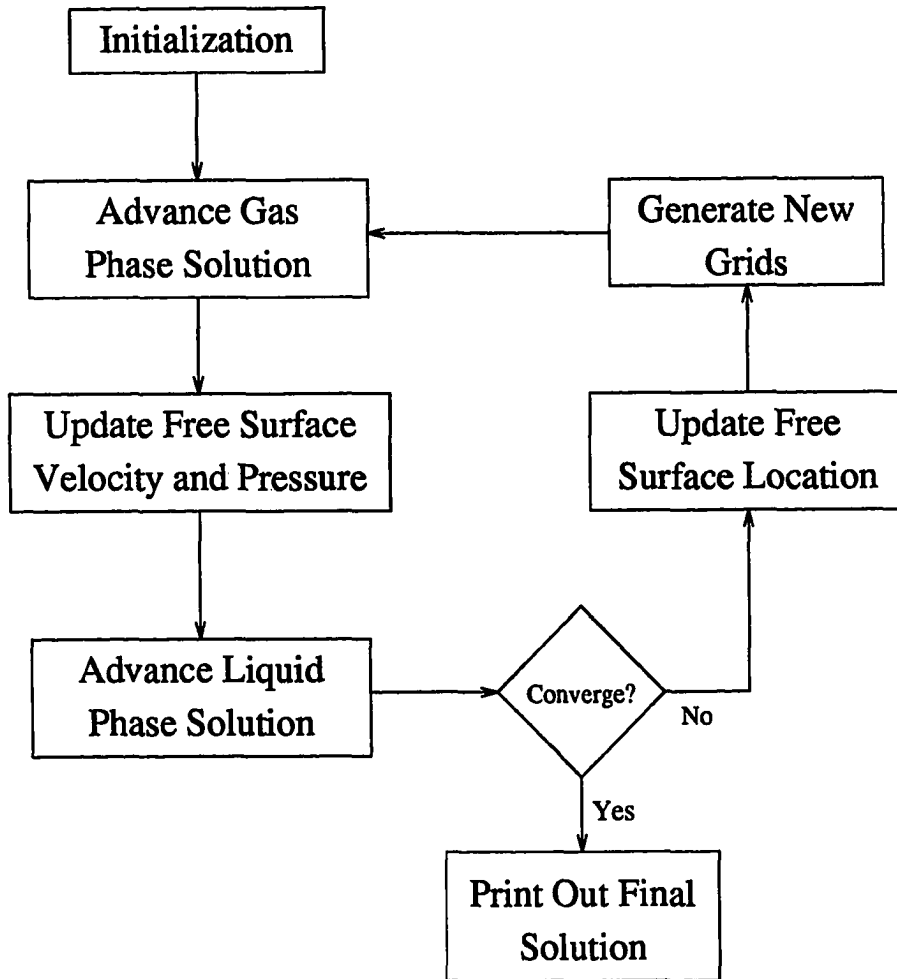


Figure 3.2: Schematic of the overall solution procedure

3. The interface conditions are then solved with the latest gas phase pressure and shear stress for the new liquid phase velocity and pressure at the free surface. The new conditions at the free surface are then used to solve the incompressible Navier-Stokes equations in the molten layer. The temperature field within the molten layer is updated and various temperature dependent properties are reevaluated.
4. The location of the free surface is then updated by solving Eqn. 3.47. The molten layer and gas jet grids are regenerated and Steps 2–4 are repeated until convergence.

It is found that better convergence is obtained if Steps 3 and 4 are repeated until the maximum numerical residual (as determined by the modified continuity equation, $\beta \nabla \cdot \vec{V}$) within the molten layer is below some specified tolerance before the gas jet solution is recomputed.

CHAPTER 4. RESULTS AND DISCUSSION

The numerical algorithm and solution procedure presented in the previous chapter are used for the numerical study of reactive gas assisted laser cutting. Before discussing the results obtained for the laser cutting simulations, results of several test cases are presented as a validation step for the computer code. The test cases that are chosen include both steady and unsteady calculations and cover a wide range of flow regime.

Incompressible Flow

The incompressible flow results are obtained for a non-rotating circular cylinder in cross flow at low Reynolds numbers. The flow features are characterized by the generation of steady and unsteady vorticity in the proximity of the cylinder and its kinematic and dynamic convection and redistribution downstream of the cylinder.

Circular Cylinder $Re = 40$

At Reynolds number of 40, the flow over a circular cylinder is characterized by a steady twin-vortex behind the cylinder. Because of the symmetry in the flow pattern, the computational domain is restricted to the upper half of the cylinder. A 50×53 O-type grid is used for the calculation as shown in Fig. 4.1. The flow is started impulsively from rest and since only the steady state solution is of interest, no sub-iteration between time levels is used.

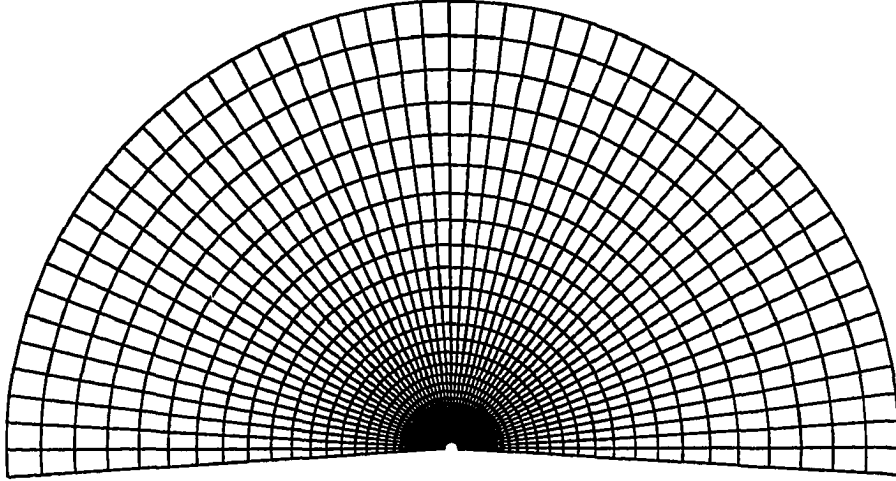


Figure 4.1: 50×53 O-type grid for the upper half of the circular cylinder

The comparison of pressure coefficient on the surface of the cylinder obtained by the present calculation with those by Pletcher and Tenpas [58] and by Rhie [59] is presented in Fig. 4.2. The comparison is excellent over the entire surface of the cylinder. Fig. 4.3 shows the skin friction coefficient distribution along with experimental data of Acrivos *et al.* [60] for the unseparated region. The skin friction for this comparison has been defined as

$$c_f = \frac{\tau_w}{\sqrt{Re}} \quad (4.1)$$

Again, good comparison is observed. The streamlines and pressure contour plots are shown in Figs. 4.4 and 4.5 respectively. The flow features are well defined by the present calculation. The reattachment of the recirculation region is observed at $2.3D$ downstream of the cylinder. This compares well with the results of Lim [61] where the reattachment

distance was obtained at $2.2D$.

Circular Cylinder $Re = 200$

It is known that $Re = 40$ represents the upper limit beyond which the flow over the circular cylinder becomes unsteady. Therefore, at $Re = 200$, the flow is now characterized by the periodic shedding of vortices. These vortices are convected downstream of the cylinder to form what is known as the Karman vortex street. Since the flow is no longer symmetrical, the flow is computed using a 100×35 O-type grid around the complete cylinder. The computational domain is shown in Fig. 4.6.

The flow is again started impulsively from rest and quickly developed into a symmetrical flow pattern similar to that observed for the $Re = 40$ case. In principle, the generation of an asymmetrical configuration is possible without the addition of a numerical disturbance but it will take a longer time for an established periodic solution to be obtained. In the present calculation, the asymmetrical configuration is triggered by introducing an asymmetric disturbance at $t = 21$. The disturbance can be expressed as

$$21 < t \leq 22 \quad u_w = 0.15; \quad 22 < t \leq 23 \quad u_w = -0.25 \quad (4.2)$$

where u_w is the cylinder surface velocity. The main effect of the disturbance is to modify the value of ζ_w (k component vorticity on the wall). The wake then evolves towards a periodic configuration as shown in Fig. 4.7 which gives the time evolution of lift and drag coefficients due to the pressure field. When the flow has reached the periodic configuration, the lift coefficient amplitude is observed to vary between ± 0.33 .

The results shown are obtained by marching the impulsively started solution with a nondimensional time step (Δt) of 0.005. At each time step, sub-iterations are carried out

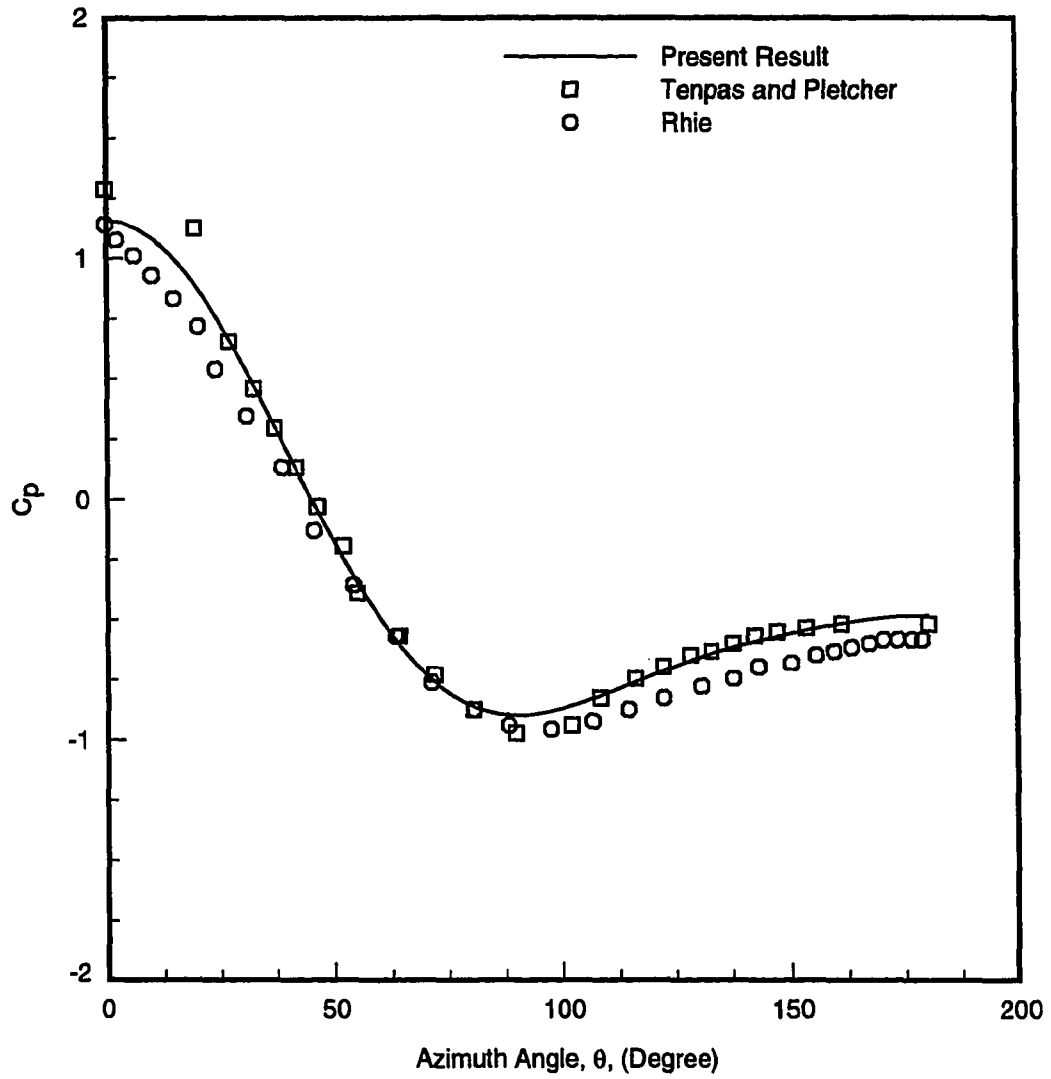


Figure 4.2: Comparison of pressure coefficient distributions on the circular cylinder at $Re = 40$

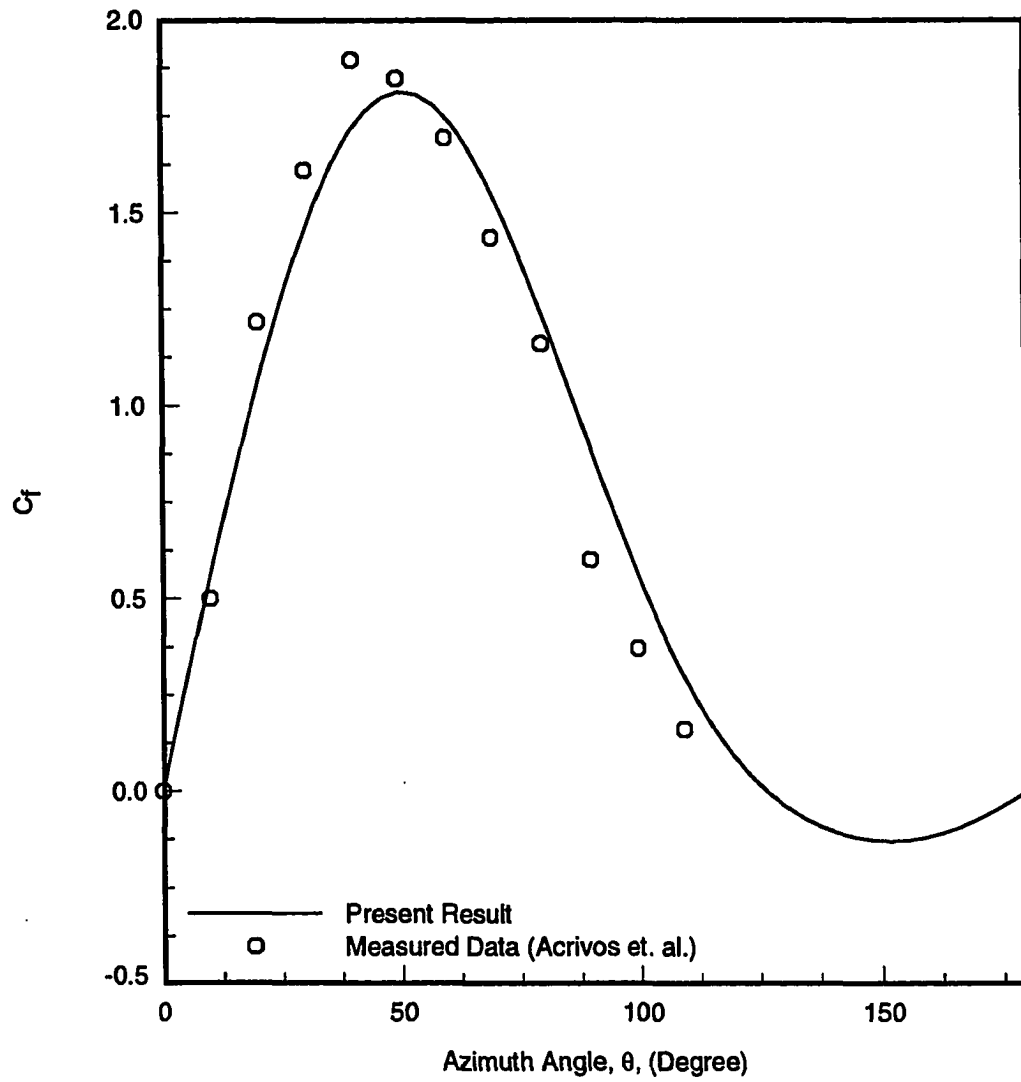


Figure 4.3: Comparison of skin friction coefficient distributions on the circular cylinder at $Re = 40$



Figure 4.4: Streamlines of the flow over the circular cylinder at $Re = 40$

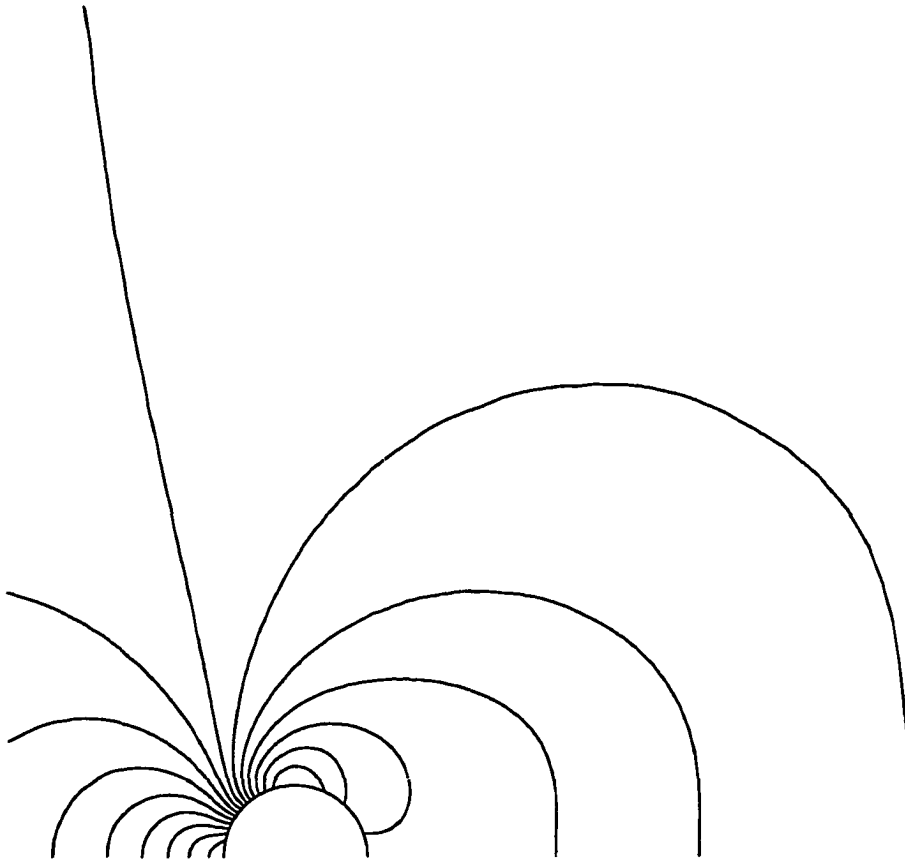


Figure 4.5: Pressure contours for the flow over the circular cylinder at $Re = 40$

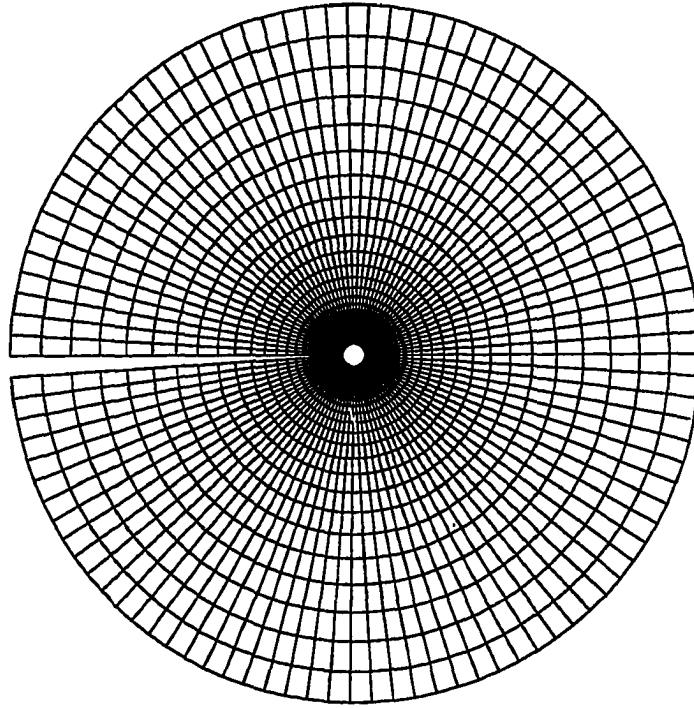


Figure 4.6: 100×35 O-type grid for the complete circular cylinder

until the maximum divergence of the velocity $\beta \nabla \vec{V}^{n+1,m+1}$ is less than 8×10^{-4} . This ensures mass continuity at each time step. A more stringent convergence criteria did not produce any noticeable difference in the final periodic solution. During the initial transient, the maximum number of sub-iterations is limited to 20 since only the final periodic solution is of interest. But, this number rapidly decreases to an average of 2 iterations per time step once the the solution becomes fully periodic.

The streamlines at 5 time levels are shown in Fig. 4.8 corresponding to $t = 160.00$, 161.44, 162.88, 164.32, and 165.76 respectively. The figure shows the alternate shedding

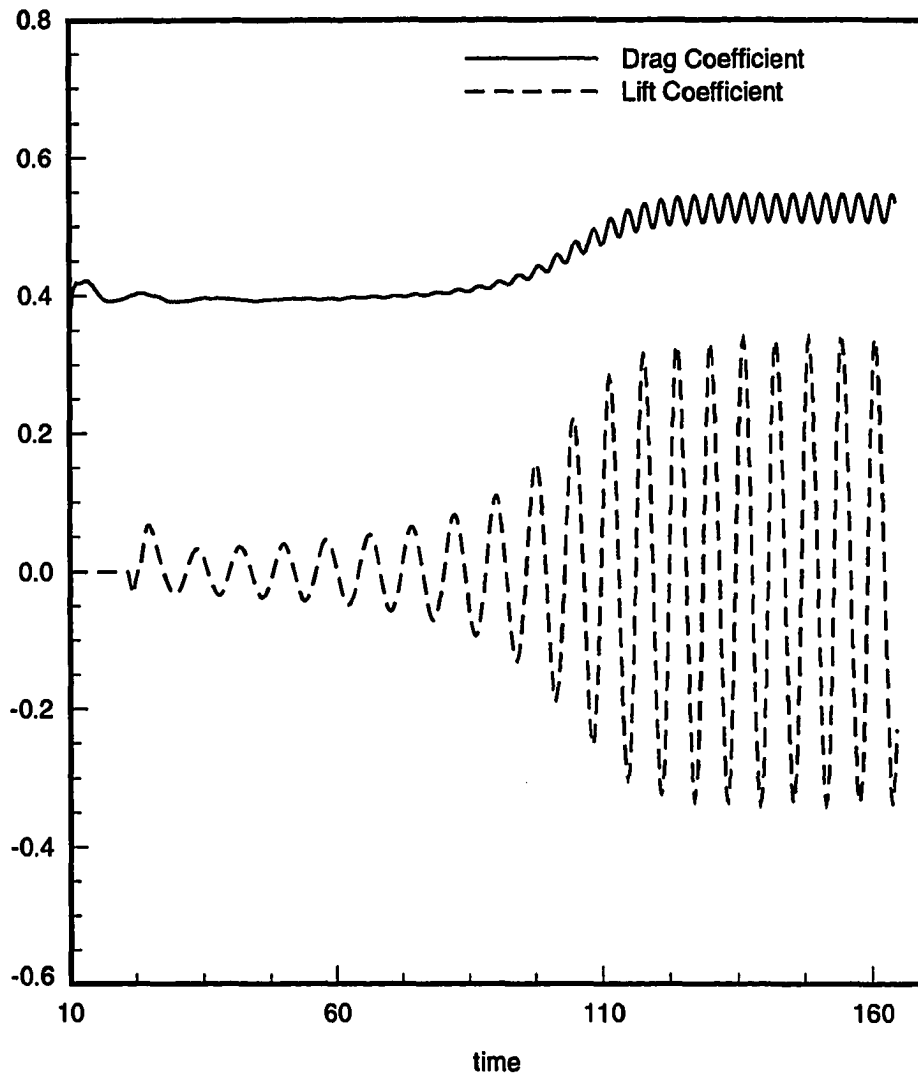


Figure 4.7: Time evolution of lift and drag coefficients on the circular cylinder at $Re = 200$

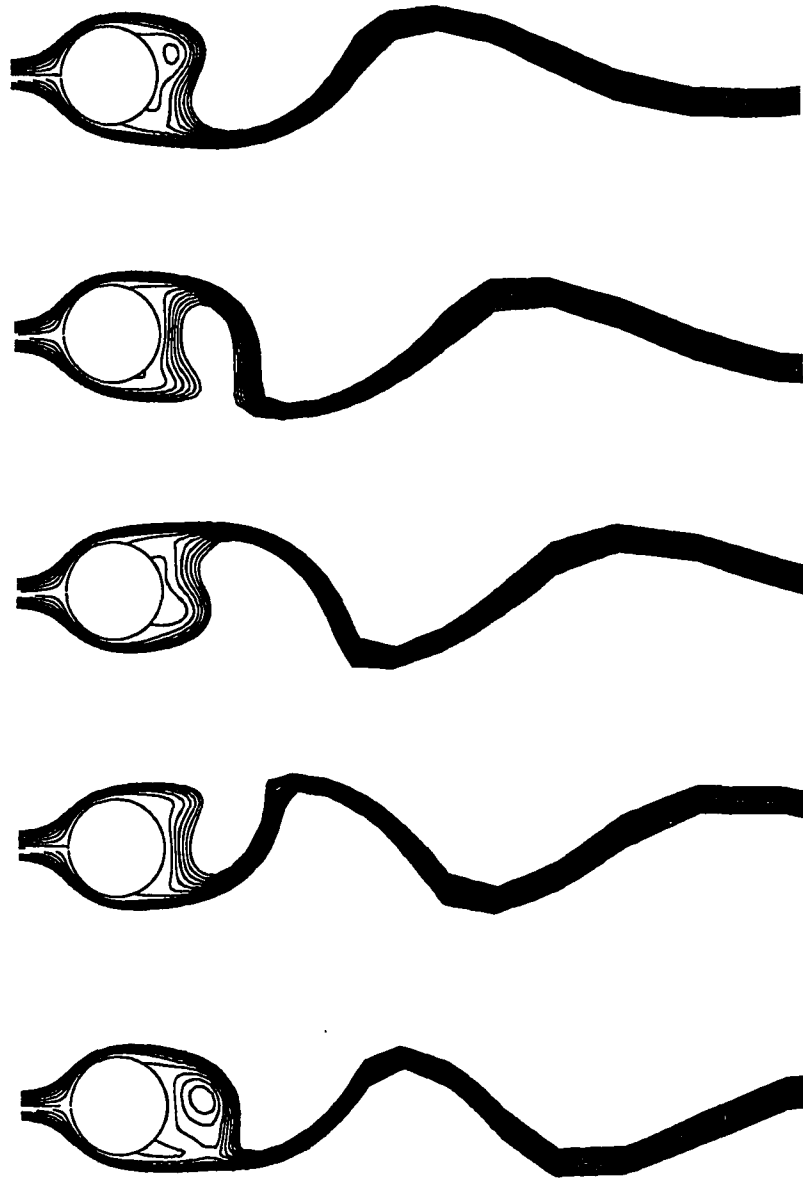


Figure 4.8: Streamlines of the flow over the circular cylinder at $t = 160.00, 161.44, 162.88, 164.32,$ and 165.76 at $Re = 200$

of vortices and the convection of these vortices downstream of the cylinder to form a trail of staggered vortices in the Karman vortex street. The Strouhal number in the present calculation is estimated to be 0.16. This corresponds well with existing numerical as well as experimental range of 0.15 to 0.19 [62].

Compressible Flow

Four test cases are presented to validate the numerical algorithm for solving compressible flows. These cases are chosen to evaluate the merits of the algorithm on time accuracy, shock capturing, and the ability to remove oscillations around discontinuity. These test cases are computed using the 3rd order upwind biased scheme, unless otherwise stated.

Shock Tube

The classical shock tube problem is an excellent test case for any unsteady Euler solver because the solution simultaneously contains a shock wave, a contact discontinuity, and an expansion fan. The initial configuration consists of two gases in a long tube at different pressures and densities separated by a diaphragm. At the bursting of the diaphragm, the pressure discontinuity propagates to the right in the low pressure gas and simultaneously, an expansion fan propagates to the left in the high pressure gas. At the same time, a contact discontinuity separating the two gas regions propagates to the right of the tube. An exact solution based on characteristics considerations [63] can be obtained for this problem.

In the present calculation, the problem is solved on a 100×10 cartesian grid with symmetry boundary conditions applied in the y direction. The domain is extended from $x = 0$ to $x = 1.00$ with the diaphragm located at $x = 0.5$. The initial pressure and density

ratios of the two gases are chosen as

$$\frac{p_L}{p_R} = 10 \quad \frac{\rho_L}{\rho_R} = 8 \quad (4.3)$$

Figure 4.9 shows the nondimensionalized pressure distributions in the tube at $t = 0.211$ along with the exact solution. The present result is obtained with Roe's "Superbee" limiter. It is found that without the limiter, the solution exhibits an expansion shock at the initial diaphragm location. Nevertheless, the present result presented in Fig. 4.9 shows the correct locations of the various discontinuities at time $t = 0.211$. In addition, the introduction of the flux limiter essential removes any oscillation around the discontinuity and the solution exhibits a smooth transition between the various regions of the flow. The comparison of Mach number and density distributions with the exact solution are shown in Figs. 4.10 and 4.11 respectively. The contact discontinuity separating the two gases is evident in these plots.

Supersonic Flow in a 10° Double-Wedge Channel

The supersonic flow over a 10° double-wedge protuberance in the lower wall of an otherwise straight two dimensional channel serves as the validation case for the ability of the present algorithm to handle complex multiple-shocks system. It also served as the basis for evaluating the effects of the flux limiter.

The height of the channel is chosen to be $0.6L$ where L is the chord length of the wedge. The computational domain is extended one chord length upstream and downstream of the wedge. The domain is discretized into 91×40 grid points as shown in Fig. 4.12. The inlet Mach number M_∞ is taken as 2.0.

Figures 4.13 and 4.14 compare the pressure coefficient distributions on the lower and upper surface of the channel with that obtained by the OVERFLOW solver of Buning *et*

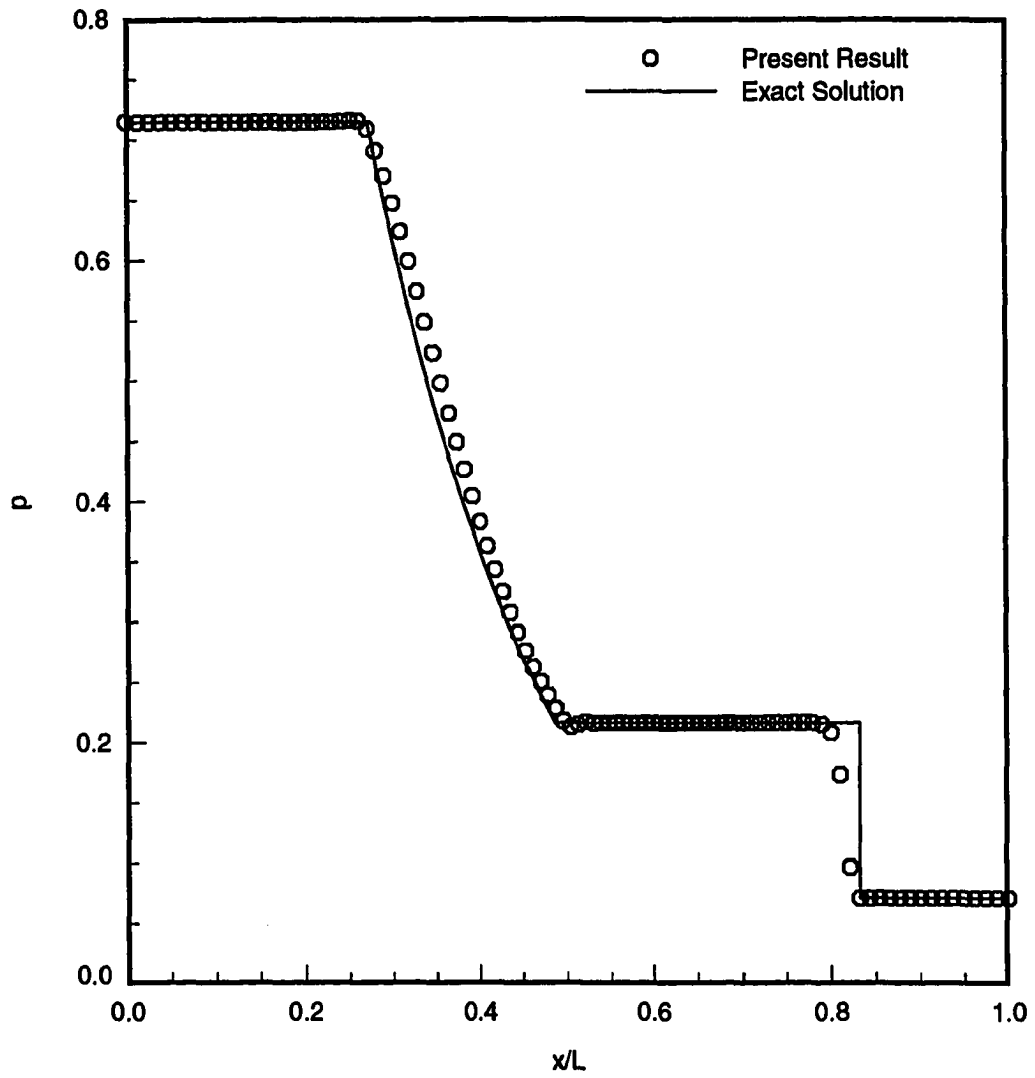


Figure 4.9: Comparison of pressure distributions in the shock tube at $t = 0.211$ using the 3rd order upwind biased scheme

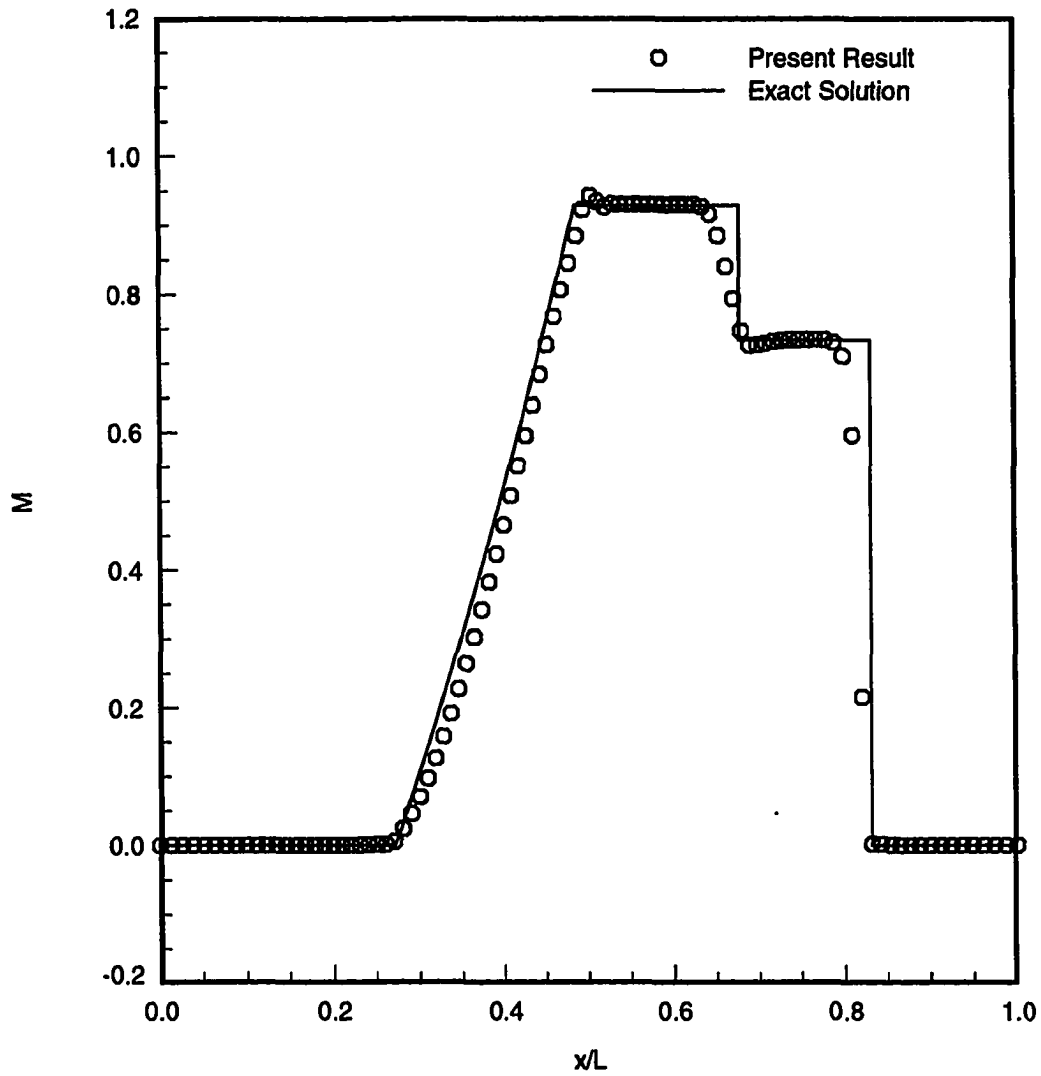


Figure 4.10: Comparison of Mach number distributions in the shock tube at $t = 0.211$ using the 3rd order upwind biased scheme

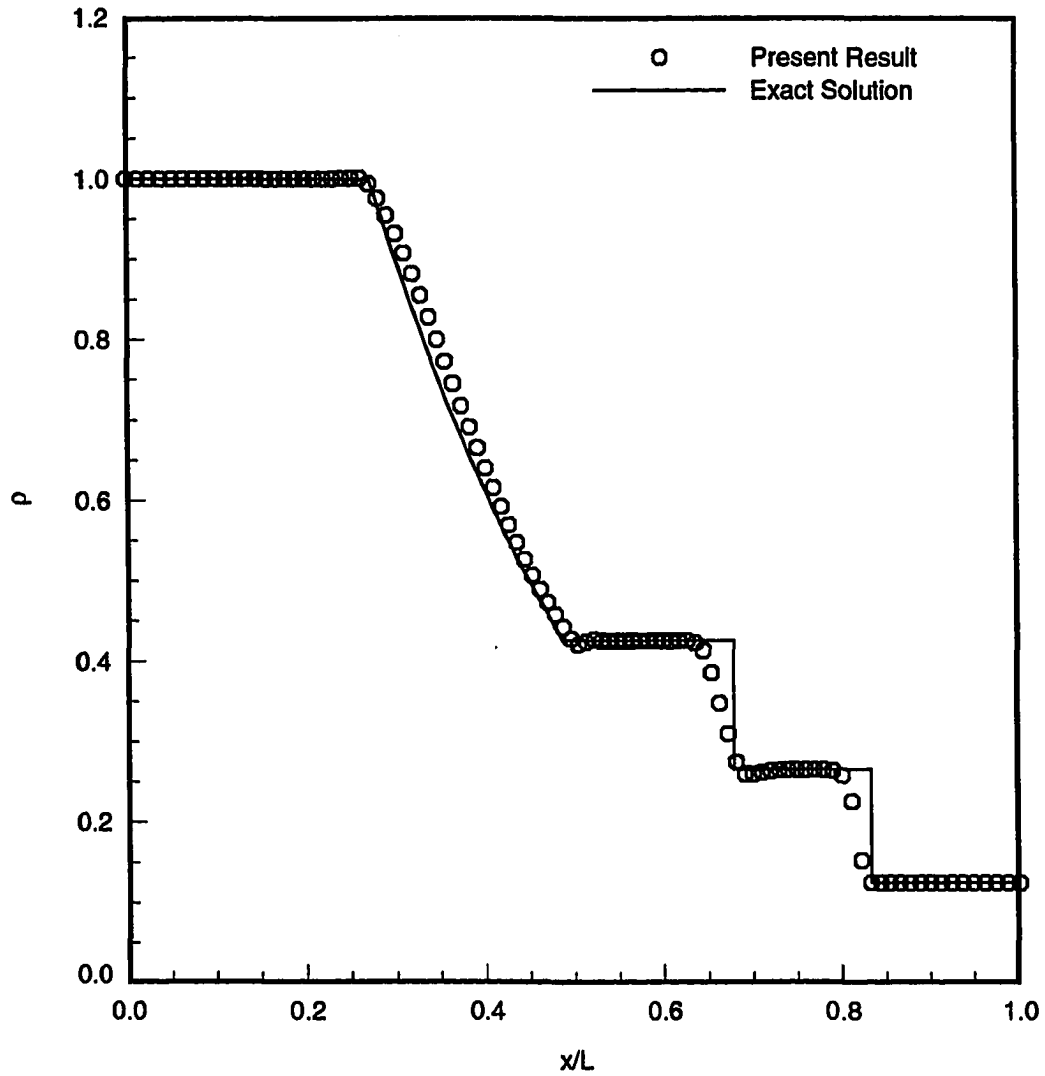


Figure 4.11: Comparison of density distributions in the shock tube at $t = 0.211$ using the 3rd order upwind biased scheme

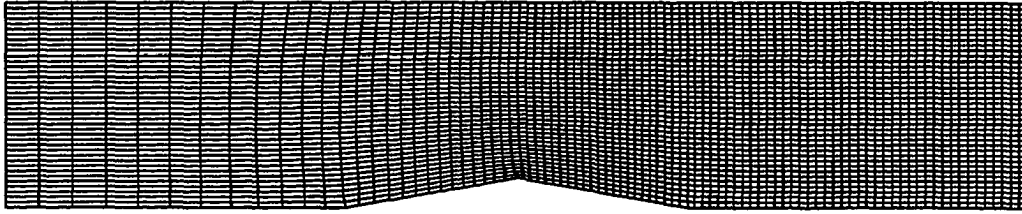


Figure 4.12: 91×40 grid for the 10° double-wedged channel

al. [64]. The comparison is generally good except for the oscillations around the reflected shocks off the lower and upper surfaces of the channel.

The effects of introducing flux limiter are illustrated in Figs. 4.15 and 4.16 which show the Mach number distributions on the lower and upper walls respectively. The results show a marked improvement in the quality of the captured discontinuities. The oscillations which are present in the 3rd order upwind biased scheme are essentially removed—as opposed to being damped out in the case where artificial dissipation is added—with the addition of the flux limiter.

The pressure coefficient contours for the case with and without the flux limiter are shown in Figs. 4.17(a) and 4.17(b) respectively. The multiple-shock system in the channel are well captured with the 3rd order upwind biased scheme. However, the scheme without the flux limiter shows excessive oscillations in the vicinity of the discontinuities (Fig. 4.17(b)). But the oscillations are removed if the extrapolation of the flux differences are limited by the flux limiter (Fig. 4.17(a)).

Axisymmetric Flow over SOCBT Projectile

The flow around the SOCBT (Secant-Ogive-Cylinder-Boattail) projectile is investi-

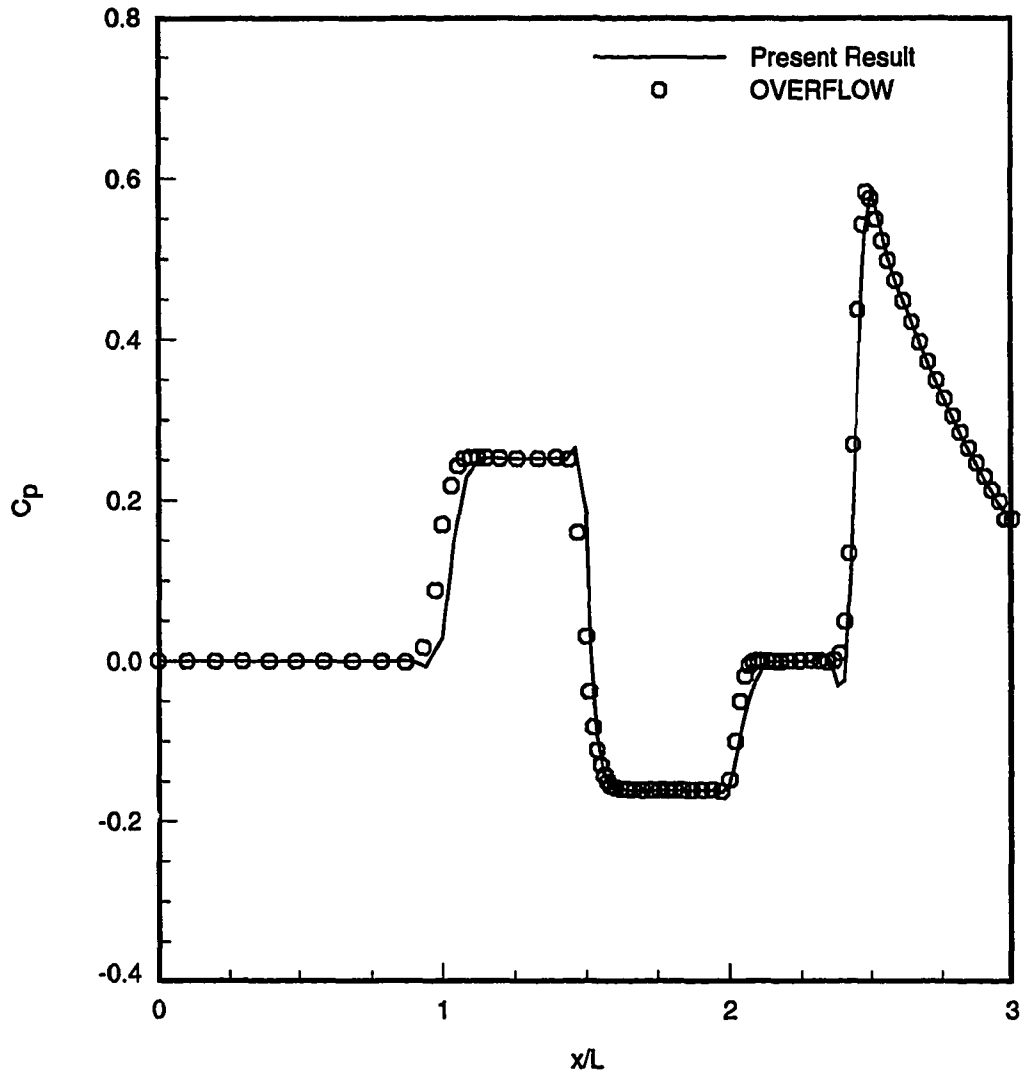


Figure 4.13: Comparison of pressure coefficient distributions on the lower surface at $M_\infty = 2.0$

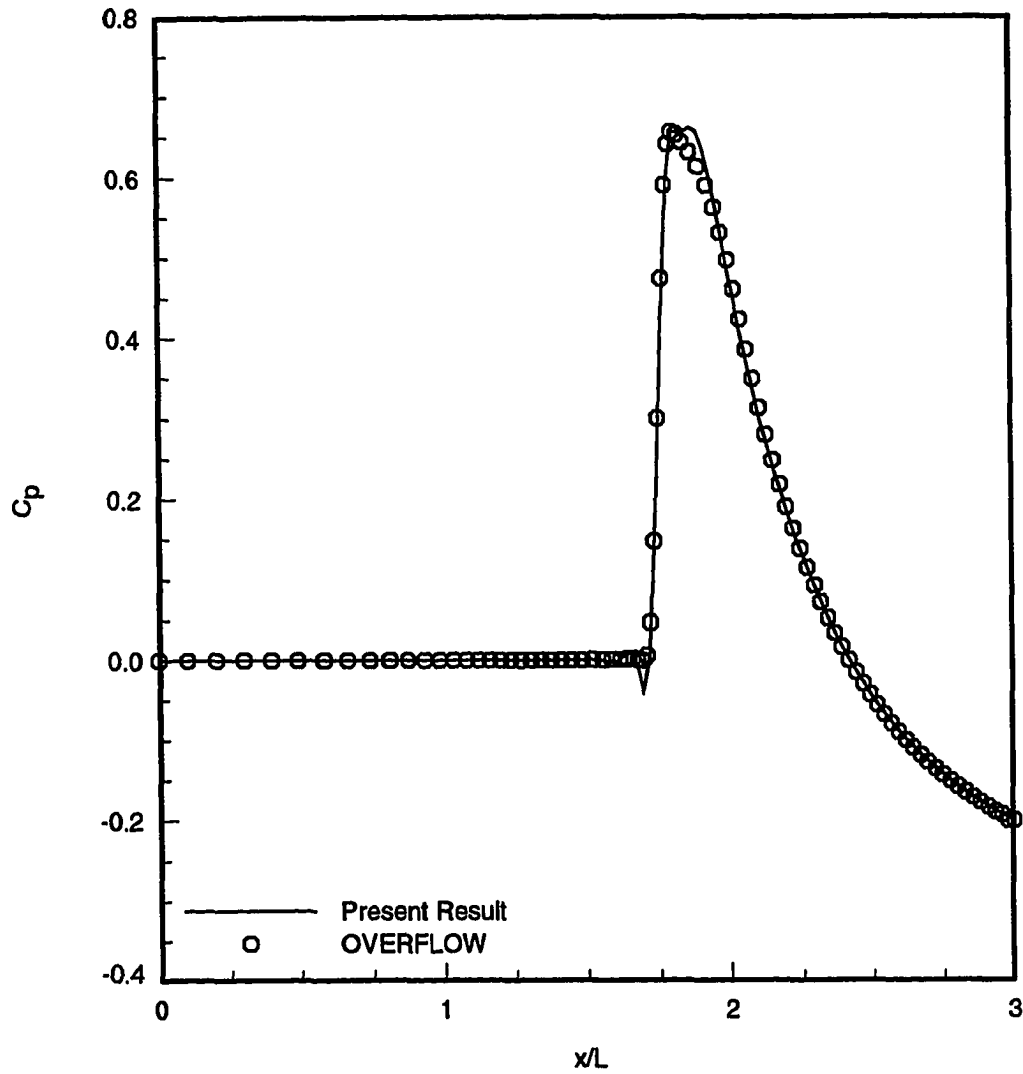


Figure 4.14: Comparison of pressure coefficient distributions on the upper surface at $M_\infty = 2.0$

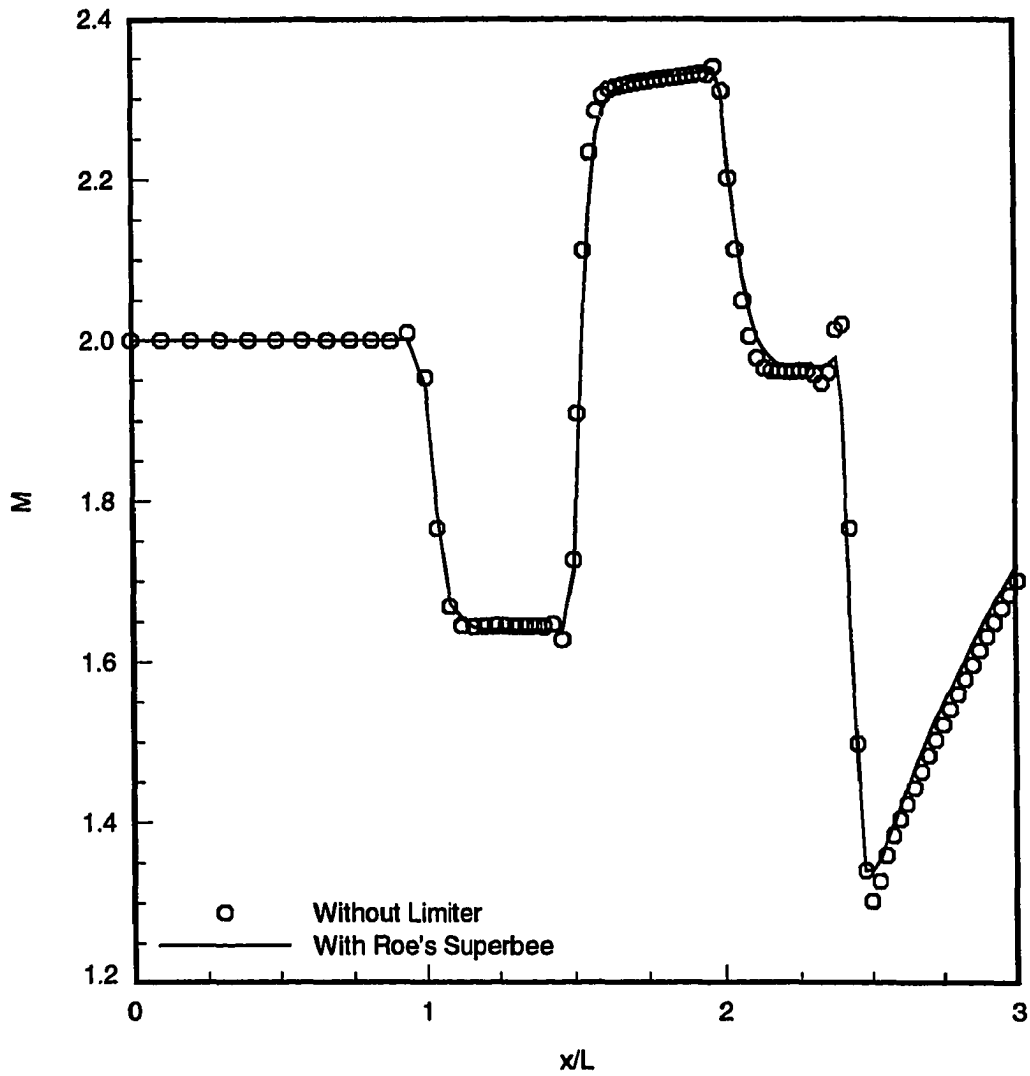


Figure 4.15: Comparison of Mach number distributions on the lower wall using the 3rd order upwind biased scheme with and without Roe's "Superbee" limiter

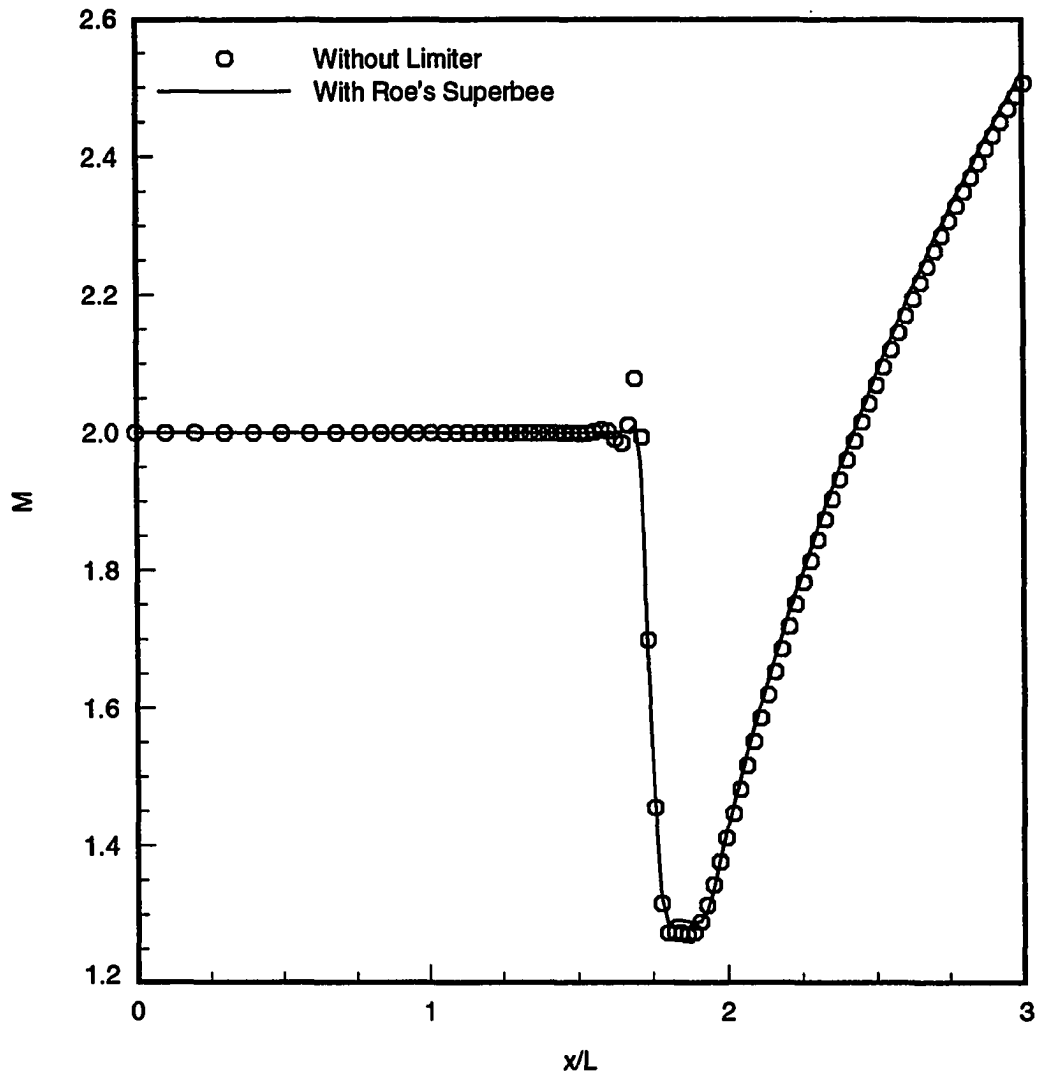
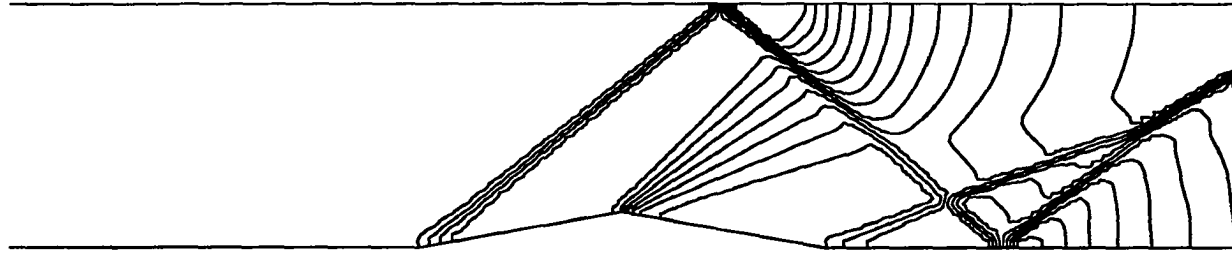
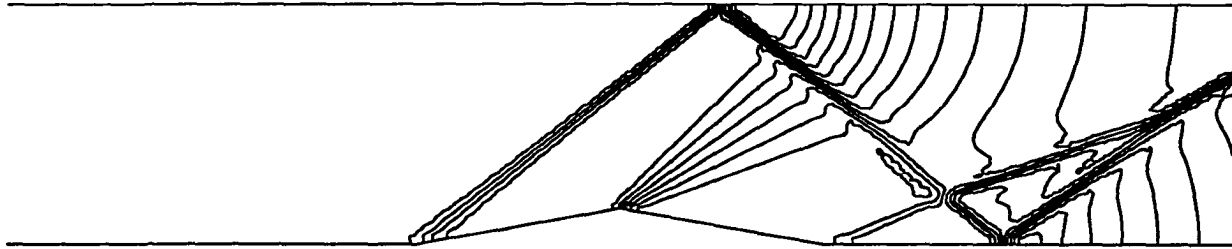


Figure 4.16: Comparison of Mach number distributions on the upper wall using the 3rd order upwind biased scheme with and without Roe's "Superbee" limiter



(a) With Roe's "Superbee" limiter



(b) Without limiter

Figure 4.17: Comparison of pressure coefficient contours in the channel with and without Roe's "Superbee" limiter

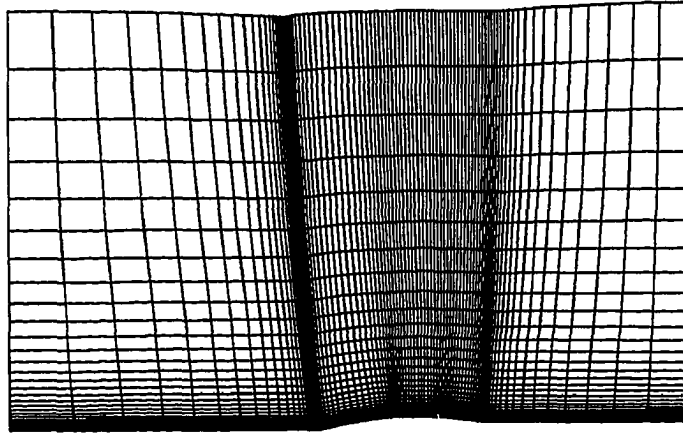


Figure 4.18: 89×30 hyperbolic grid around the SOCBT projectile

gated to assess the accuracy of the axisymmetric algorithm. The projectile in this test case has a 3-caliber secant-ogive part, 2-caliber cylinder and a 1-caliber 7-degree boattail which is attached to a sting. The transonic flow pass the projectile at $M_\infty = 0.96$ and at zero angle of attack is obtained only for the inviscid solution. A 89×30 hyperbolic grid is used for the computation. The grid is shown in Fig. 4.18.

The comparison of pressure coefficient distributions on the surface of the projectile is shown in Fig. 4.19. The excellent agreement between the present inviscid result and the measured data [65] is due to the high Reynolds number nature of the flow where the boundary layer is very thin (requires first wall normal spacing of $2 \times 10^{-5} D$ to resolve). Note that both results, with and without the limiter, are shown in Fig. 4.19. The pressure contours in the vicinity of the projectile is shown in Fig. 4.20. The flow is characterized by two stationary shock waves on the cylinder and boattail part of the projectile. Once again, these shocks are well captured with the present algorithm.

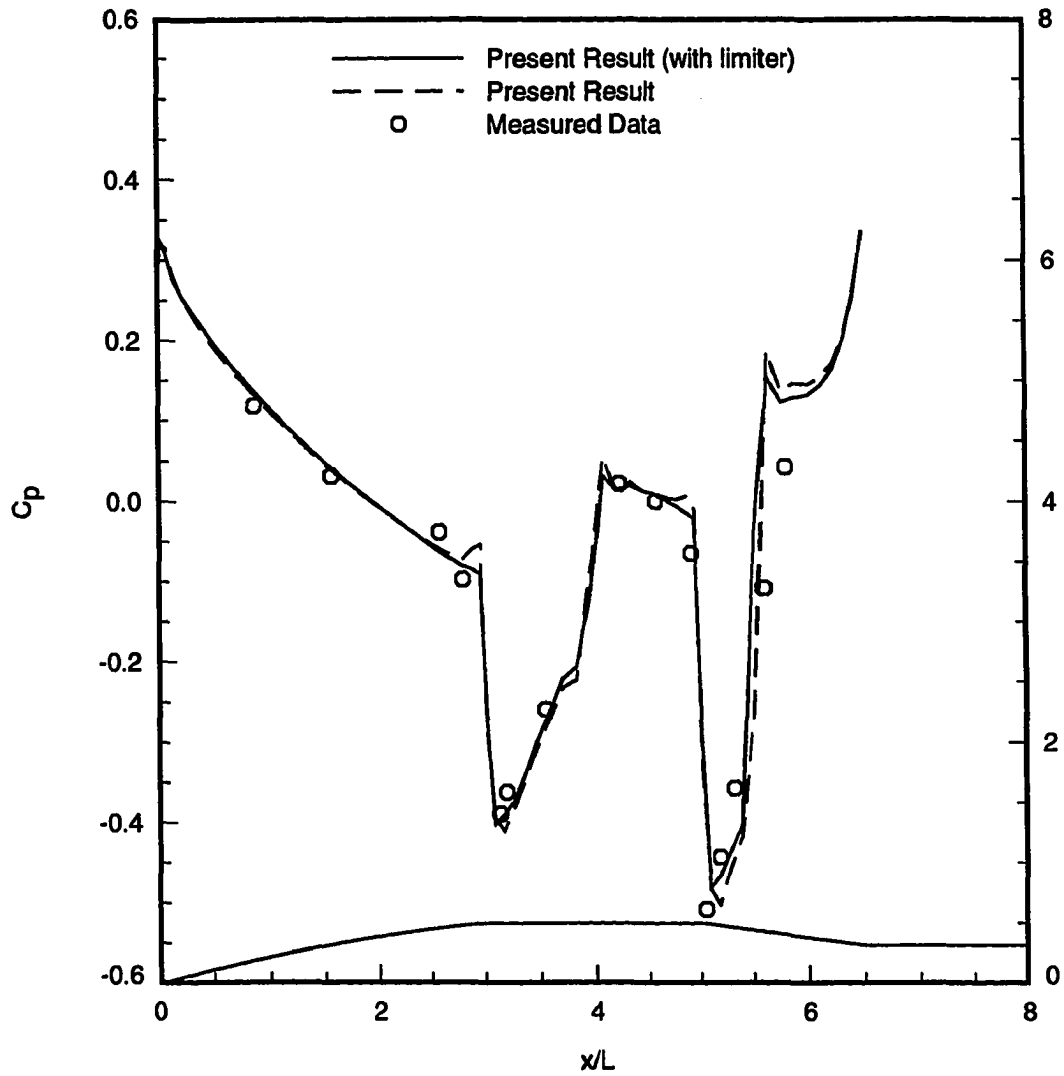


Figure 4.19: Comparison of surface pressure coefficients at $M_\infty = 0.96$ with measured data for the SOCBT projectile

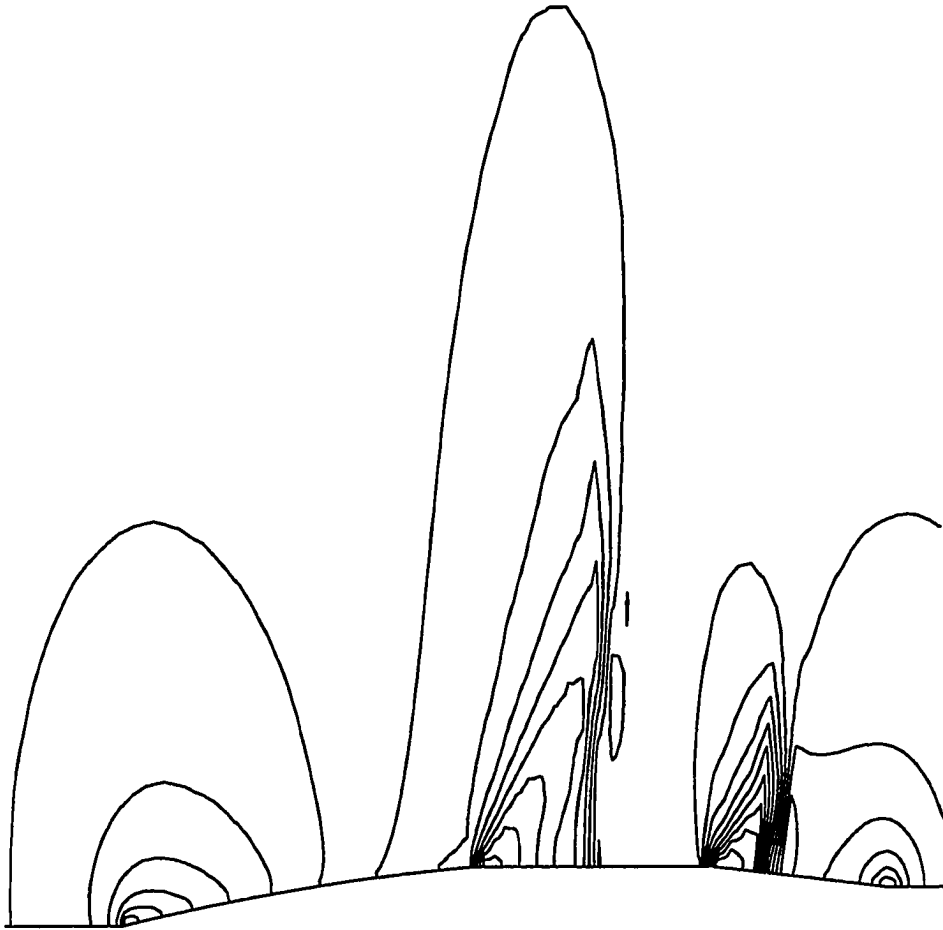


Figure 4.20: Pressure contours near the SOCBT projectile at $M_\infty = 0.96$

Shock-Boundary Layer Interaction

The merits of the numerical algorithm have been demonstrated for inviscid calculations. The results so far indicate that the present formulation for the inviscid calculations is valid. Good comparison is obtained in all cases and sharp discontinuities are observed in the computed results. The last test case is intended to verify the viscous calculation of the present algorithm. The thin-layer approximation is used in this case.

The shock/boundary layer interaction problem considered here has been studied extensively [66–70]. In this problem, the freestream Mach number (M_∞) is 2.0 while the Reynolds number based on the distance from the edge to the location of shock impingement is 0.296×10^6 . The angle of the impinging shock is 32.6 degree with respect to the flat plate.

A 72×65 grid with mild grid clustering in the horizontal direction near the impingement location is used for the present calculation. The vertical grid spacings are chosen to properly include the important physical mechanisms of the shock-boundary layer interaction. The following vertical grid spacings based on triple-deck theory [66] are used

$$\Delta y_j = 1.5625 \times 10^{-4} \quad 1 \leq j \leq 4 \quad (4.4a)$$

$$\Delta y_j = 1.1868 \Delta y_{j-1} \quad 5 \leq j \leq 33 \quad (4.4b)$$

$$\Delta y_j = 3.75 \times 10^{-2} \quad 33 < j \leq 65 \quad (4.4c)$$

The top boundary is basically chosen such that the reflected shock wave from the wall does not intercept the top boundary. Hence it is appropriate to specify all variables at the inflow and top boundary.

The nondimensionalized pressure distribution on the surface is shown in Fig. 4.21 while the skin friction coefficient distribution is shown in Fig. 4.22. The present results

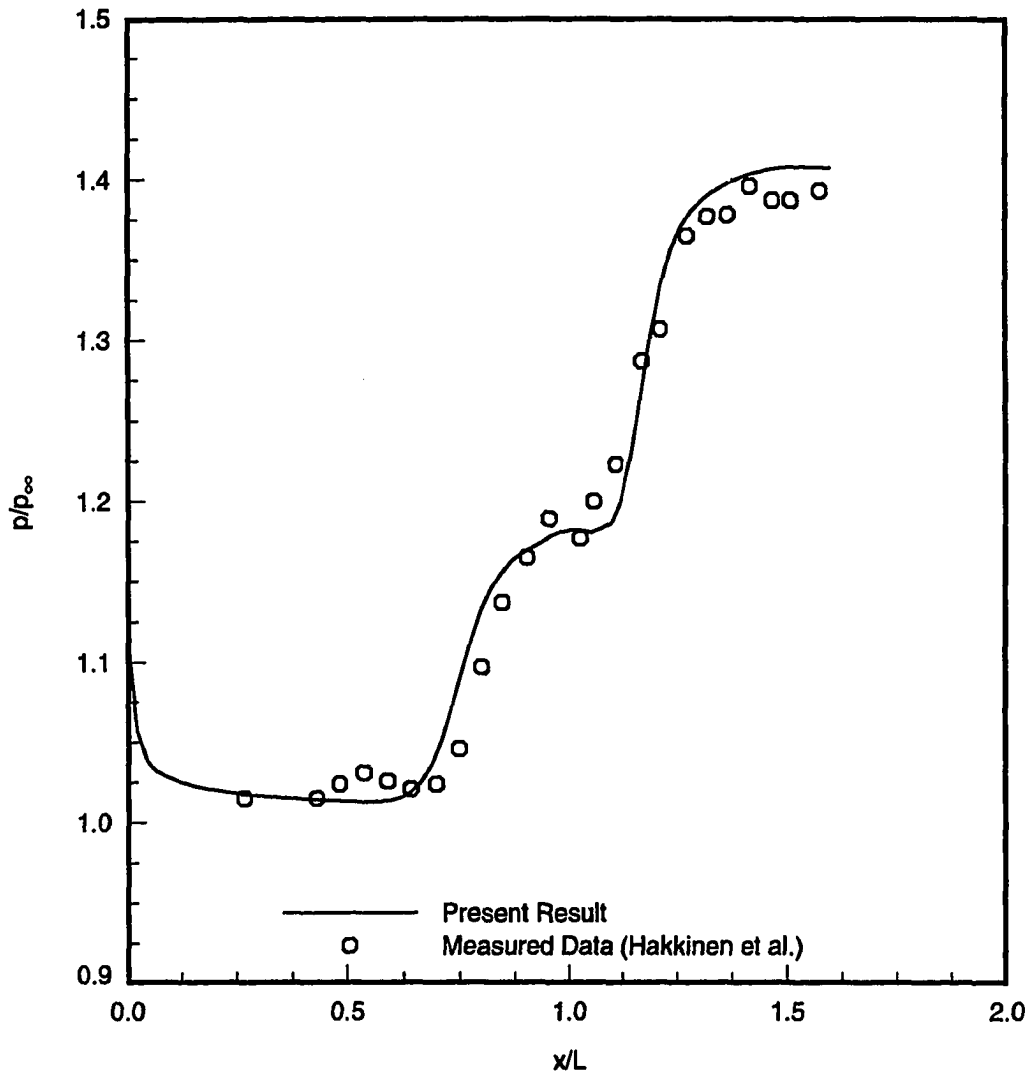


Figure 4.21: Comparison of pressure distributions on the surface of the flat plate in the shock impingement problem

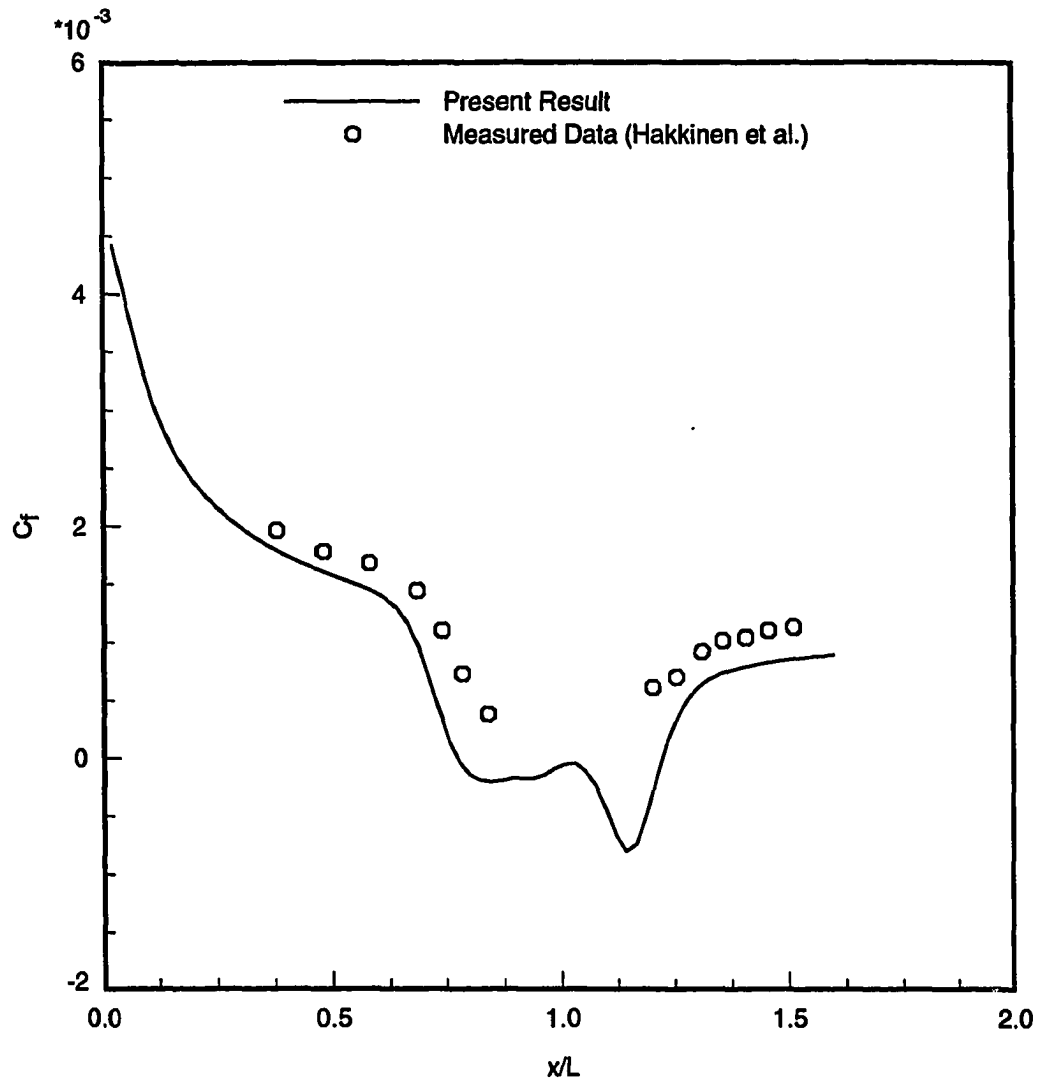


Figure 4.22: Comparison of skin friction distributions on the surface of the flat plate in the shock impingement problem

show a strong agreement with the measured data of Hakkinen *et al.* [71]. It can be seen, as indicated by the negative values of skin friction coefficient, that the strength of the impinging shock is strong enough to cause the laminar boundary layer to separate. This is further illustrated by the vector plot (see Fig. 4.23) near the separated region. The separated region in turn causes the formation of a separation shock ahead. The flow then reattaches through a reattachment shock and hence further raise the pressure on the wall (see Fig. 4.21). These features are clearly seen in the pressure contours of the shock impingement as shown in Fig. 4.24.

Reactive Gas Assisted Laser Cutting

The accuracy of the numerical algorithm adopted for the present study is demonstrated on numerous test cases. As pointed out, the present results in all test cases are in good agreement with published results. For the rest of this dissertation, results for reactive gas assisted laser cutting of a 6.35 mm thick low carbon (AISI 1008) steel plate with an oxygen jet are presented.

It should be pointed out that experimental data on laser cutting of metals are focussed primarily on the global parameters such as the maximum cutting speed or the maximum cutting depth that can be achieved for a given set of cutting conditions. However, these parameters are independent variables in the present calculations and they are specified as part of the test conditions. The computational results that will be presented are, in general, difficult to obtain or quantify through experiments. For example, the present calculations will yield, among many others, the profile of the erosion front. It is very difficult, if not impossible, to characterize this profile through experimentation due to inaccessibility of the cut kerf during the cutting process. Hence, considerable efforts have been taken

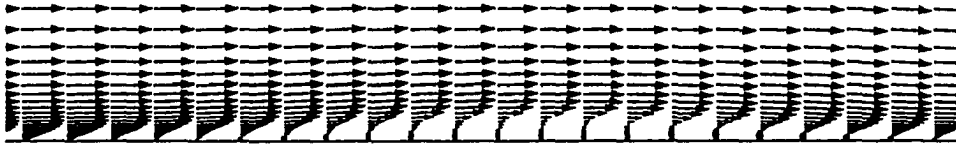


Figure 4.23: Velocity vectors of the separated region in the shock impingement problem

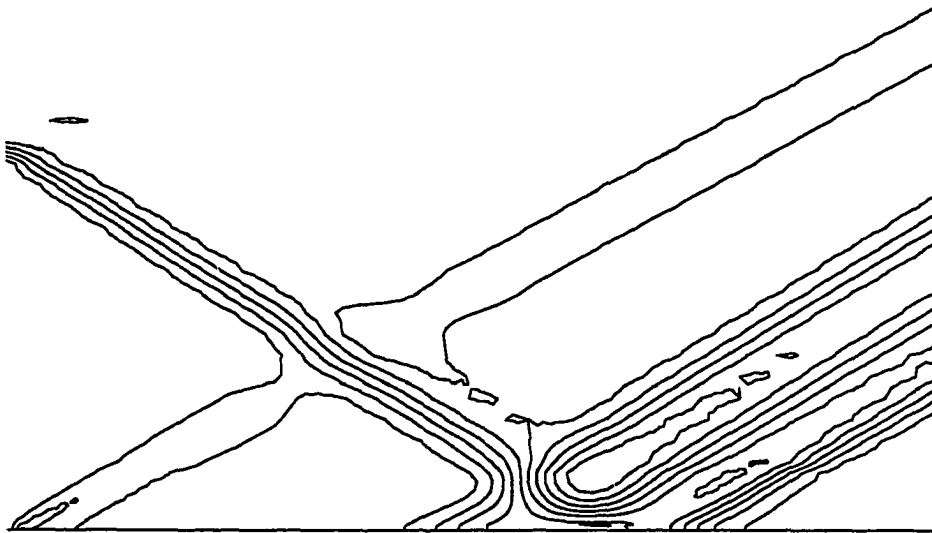


Figure 4.24: Pressure contours in the shock impingement problem

Table 4.1: Summary of cutting parameters used in the modal laser cutting case considered in the present study

Laser Power Density (q'')	1.41×10^{10} W/m ²
Beam Radius (r_l)	0.15 mm
Workpiece Thickness (t)	6.35 mm (0.25 inch)
Cutting Speed (u_c)	16.9 mm/s (40 inch/min)
Inclination Angle (θ_i)	5°

to show the validity the computer codes in the previous sections. Therefore, the merits of the computational results for laser cutting can only come from a qualitative argument that the results are plausible under the test conditions and are congruent with the various mechanisms that occur during the cutting process. This is consistent with the objective of the present work which is the development of a model that will provide considerable details of the cutting process which otherwise are subjected only to conjectures.

The various cutting conditions assumed in this model test case are summarized in Table 4.1. These cutting conditions represent a realistic case and are not arbitrarily assumed for the purpose of demonstrating the capabilities of the present model. However, the physical and transport properties of the low carbon steel (essentially 99.9 percent iron for AISI 1008) are approximated by that for liquid iron. Also, the inclination angle of 5° is determined based on experimental observations (see the Appendix).

The choices for the reference conditions in the molten layer are quite obvious with the exception of the reference velocity. An improper choice could lead to a stiff system consisting of the molten layer and the gas jet equations. For example (and this is in retrospect), if the reference velocity were taken as the cutting speed, the nondimensionalized pressure within the molten layer was of the order of 10^4 and consequently, a slight variation

in gas pressure at the erosion front would result in a large change in the driving force for the molten layer. Convergence was never attained for this choice of reference velocity. Therefore, for the present calculations, the molten layer reference velocity is chosen as 1 m/s. This value is based on the expected maximum velocity in the molten layer. With this reference velocity and a reference temperature of 1810 K, the nondimensionalization of the molten layer conditions resulted in

$$Re = 3070.0 \quad We = 9.50 \quad Fr = 40.0 \quad \text{and} \quad Pr = 0.133$$

The reference length is taken as the diameter of the nozzle exit such that both regions (the molten layer and the gas jet) have a common reference length.

The geometry of the nozzle is shown in Fig. 4.25. The nozzle has an inlet diameter (D) of 2.54 mm and the stand-off distance is set at 2.54 mm too. The nozzle is operated at a total pressure of $1.68p_\infty$. For purpose of nondimensionalization, the reference temperature and velocity are 300 K and 330 m/s respectively for the gas jet. The reference velocity corresponds to a reference Mach number of 1. The same reference conditions are used for the flow within the kerf. This yields a Reynolds number (Re) of 52,000 for the gas flow.

Axisymmetric Jet Impingement Solutions

In the overall solution strategy, the jet flow above the workpiece is obtained in an independent step. Specifically, the jet flow in this region is approximated by an axisymmetric jet impingement problem. In a strict sense, the jet flow consists of the oxygen jet emerging from the nozzle and impinging on the surface of the workpiece with air in the surrounding. A distinction between the oxygen jet and the surrounding air (and subsequently their mixing) can be made but in the present model, they are treated as if they are the same.

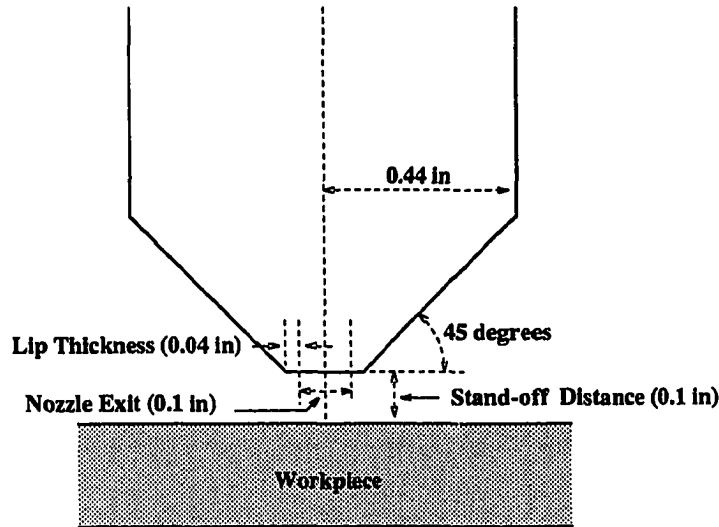


Figure 4.25: Nozzle geometry assumed in the jet impingement calculations

This should not give rise to any difficulty since from a fluid dynamics point of view, the distinction between the two (e.g., viscosity etc) is minimal. However, this will not be the case if there were chemical reactions involving both oxygen and air in the flow field.

The physical domain is extended approximately 30 diameters from the nozzle exit. A 60×40 grid is used for the calculation (see Fig 4.26). It can be shown from isentropic relations that the exit conditions will be choked only if $p_T/p_\infty > 1.89$ where p_T is the total pressure of the nozzle. Hence, the exit Mach number is below sonic speed for the present case. Therefore, three inlet conditions (total pressure p_T , total density ρ_T , and radial velocity v) are specified while a fourth condition (static pressure p) is extrapolated from the computational domain. The results are obtained using the complete Navier-Stokes equations. In light of the additional dissipation provided, the jet impingement results are obtained using the 2nd order upwind scheme.

The Mach contours in the vicinity of the nozzle exit is shown in Fig. 4.27. The

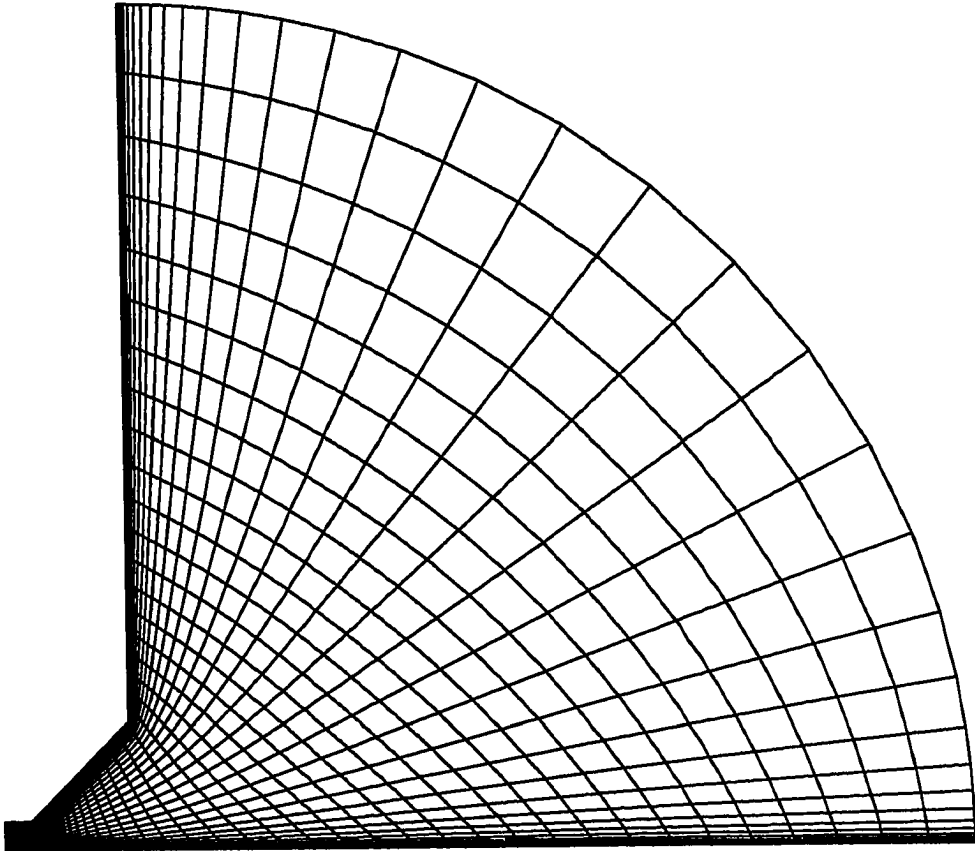


Figure 4.26: 60×40 grid for the jet impingement calculations

boundary of the jet is clearly defined in the contour plot. The maximum local Mach number is 0.85 and the entire flow region remains subsonic. The entrainment effects of the jet is clearly depicted in the vector field as shown in Fig. 4.28. More importantly in the overall strategy is the stagnation pressure on the surface of the workpiece which is shown in Fig. 4.29. The distribution shows the expected trend where the stagnation pressure on the workpiece decreases rapidly as the jet expands beyond the impingement area. Furthermore, the region of high stagnation pressure is confined within one diameter from the nozzle centerline.

Laser Cutting Solutions

The solutions for the molten layer and the jet flow within the kerf are obtained in an iterative manner as described previously. A major difficulty arises in the choices for the starting solutions in both regions. This is compounded by the lack of any previous investigation which would at least yield a qualitative description of the flow within the molten layer.

The present solutions are obtained by first assuming a profile for the erosion front. The converged solution for the gas jet within the kerf based on this initial profile is used as the starting solution in the iteration process. For the molten layer, the entire layer is assumed initially to be moving at the cutting speed in the cut direction. These choices seem to work effectively but even so, the pressure and shear stress values at the erosion front have to be relaxed in the initial phase of the iteration process.

Gas Jet The Mach number, temperature, and pressure contours of the gas jet within the kerf are shown in Fig. 4.30. As expected, the features of the flow are confined within the boundary of the jet. The boundary is clearly shown in the Mach contours (Fig. 4.30(a)).

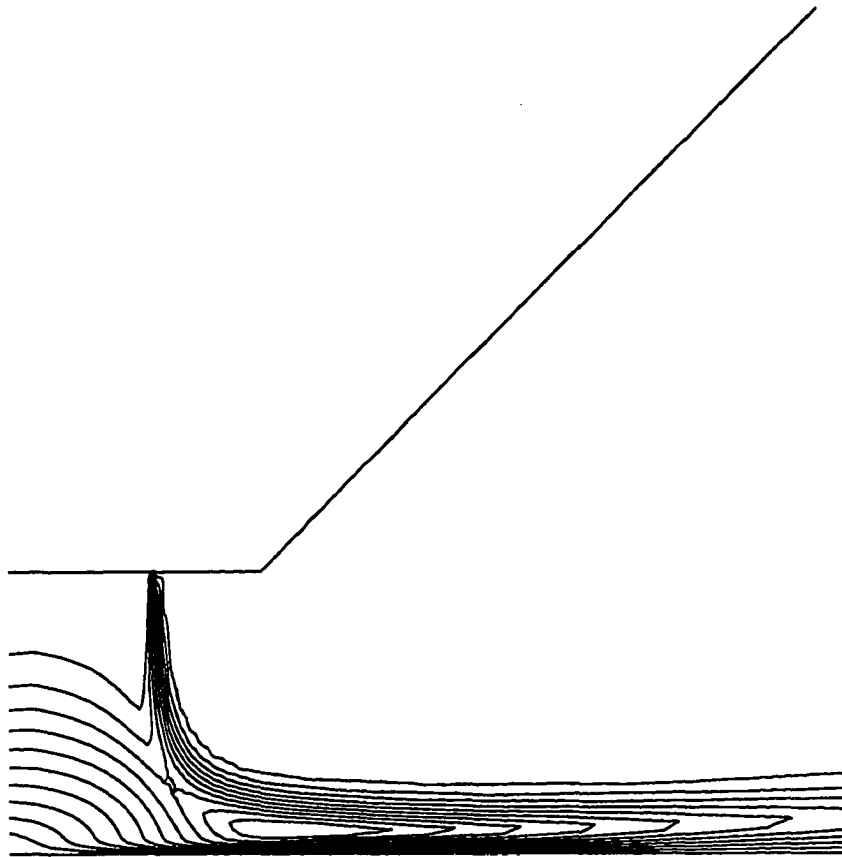


Figure 4.27: Mach contours in the vicinity of the nozzle exit

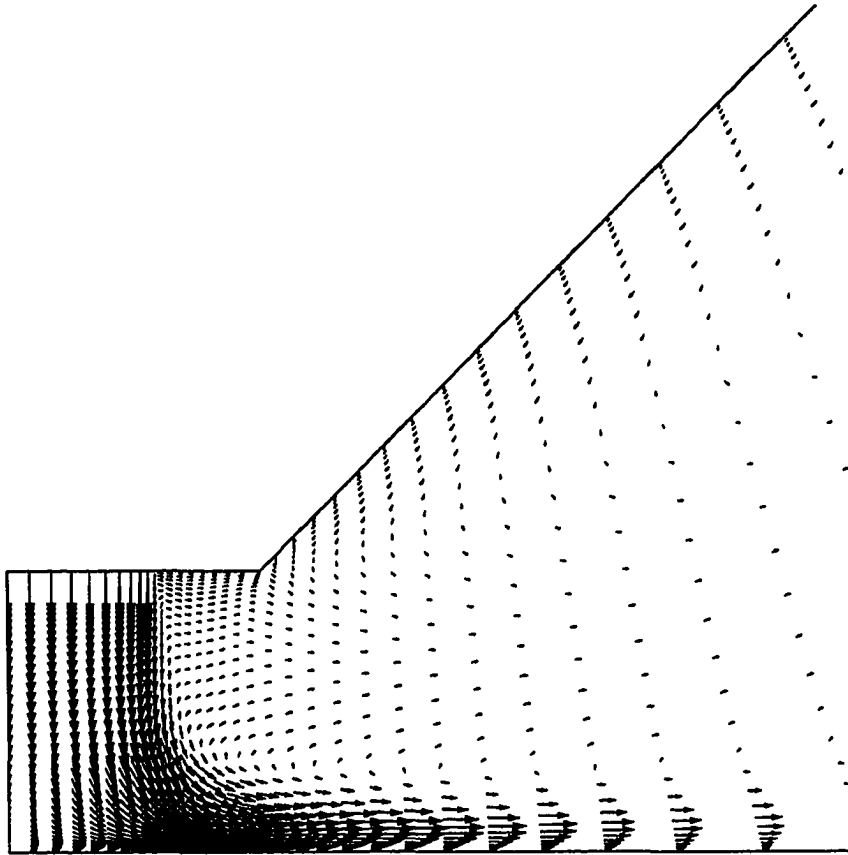


Figure 4.28: Velocity vectors in the vicinity of the nozzle exit showing the entrainment effects

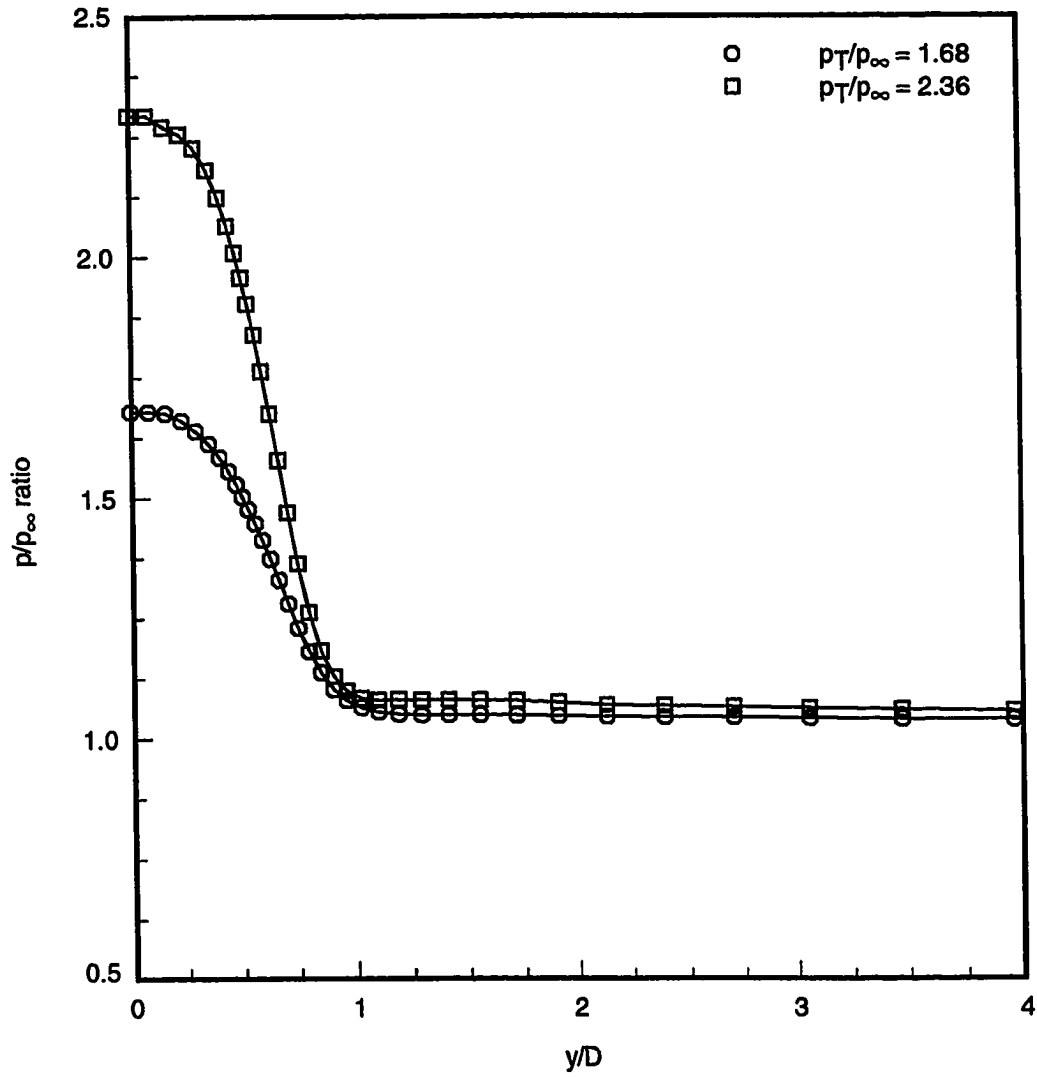


Figure 4.29: Stagnation pressure on the surface of the workpiece

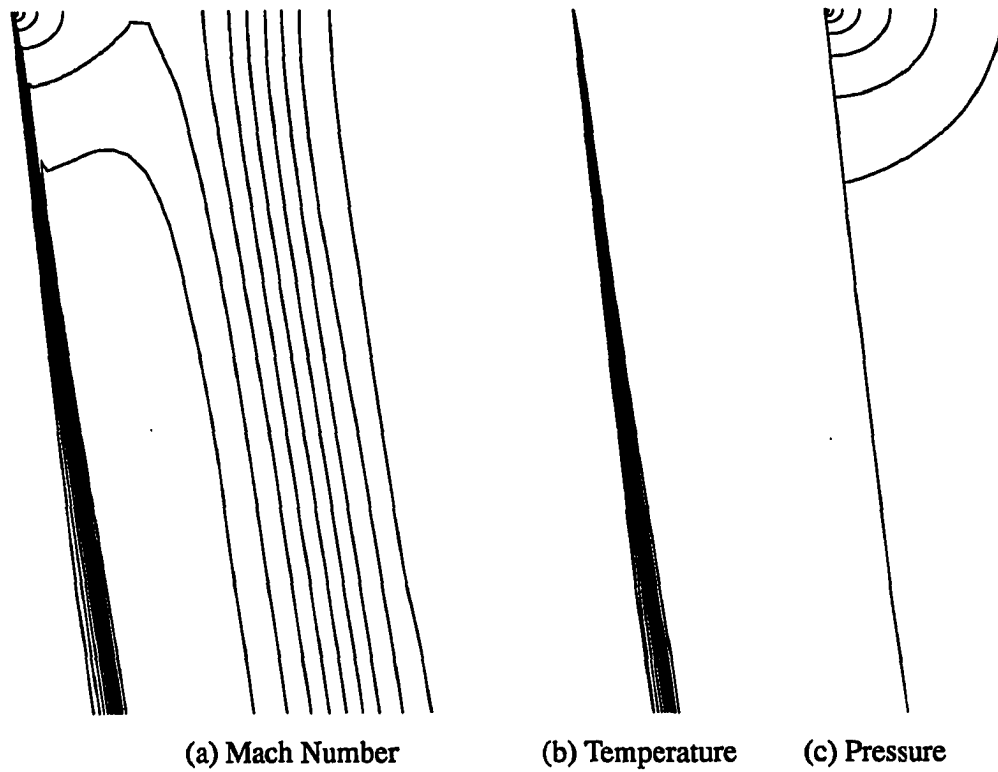


Figure 4.30: Various contour plots of the gas jet flow field within the kerf

The maximum Mach number is 0.89 and this occurs approximately at the location $x/D = 1.7$. The location of the maximum Mach number is attributed to the narrowing of the jet due to the developing boundary layer. Despite the high temperature gradients on the erosion front, no flow separation is observed in the flow field. The temperature contours plot (Fig. 4.30(b)) shows the extent of the developing thermal boundary layer while the pressure contours plot (Fig. 4.30(c)) shows the rapid expansion of the gas jet within the kerf.

The pressure and shearing stress distributions on the erosion front are shown in Fig. 4.31. Note that the pressure and shearing stress (or skin friction) values are nondimen-

sionalized as

$$c_p = \frac{p - p_\infty}{\frac{1}{2}\rho_\infty a_\infty^2} \quad \text{and} \quad c_f = \frac{\tau}{\frac{1}{2}\rho_\infty a_\infty^2}$$

For most part, the pressure values are close to the exit pressure. The minimum pressure point on the erosion front occurs near $x/D = 1.6$ and this corresponds well with the location where the maximum Mach number is observed. In addition, the slight increase in the shearing stress in the midspan of the erosion front is due to the temperature distribution.

The effects due to pressure and shearing stress on the overall material removal through ejection can be ascertained from their distributions along the erosion front. In principle, the effectiveness would depend on the forces that are generated by the pressure and shearing stress in the direction of molten flow. The axial force coefficients due to pressure and shearing stress along the erosion front are shown in Fig. 4.32. The axial force coefficients along the erosion front are computed from

$$c_{a,p} = -\frac{p \sin \phi}{\frac{1}{2}\rho_\infty a_\infty^2} \quad \text{and} \quad c_{a,\tau} = \frac{\tau \cos \phi}{\frac{1}{2}\rho_\infty a_\infty^2}$$

where ϕ is the angle between the x axis and the local tangent line at the erosion front, p and τ are the pressure and shearing stress respectively. The integration of the distributions shown in Fig. 4.32 along the arclength of the erosion front yields

$$C_{a,p} = 0.1687 \quad \text{and} \quad C_{a,\tau} = 0.0139$$

These values would indicate that the force due to pressure gradient is responsible for the effective ejection of the molten material from the cut kerf. However, a closer inspection of the distributions in Fig. 4.32 shows that $c_{a,p}$ is one order or more less than $c_{a,\tau}$ beyond $x/D = 1.0$. The large $C_{a,p}$ value is due to the high pressure values near the leading edge of the erosion front. This observation clearly defines the roles play by both pressure and shearing

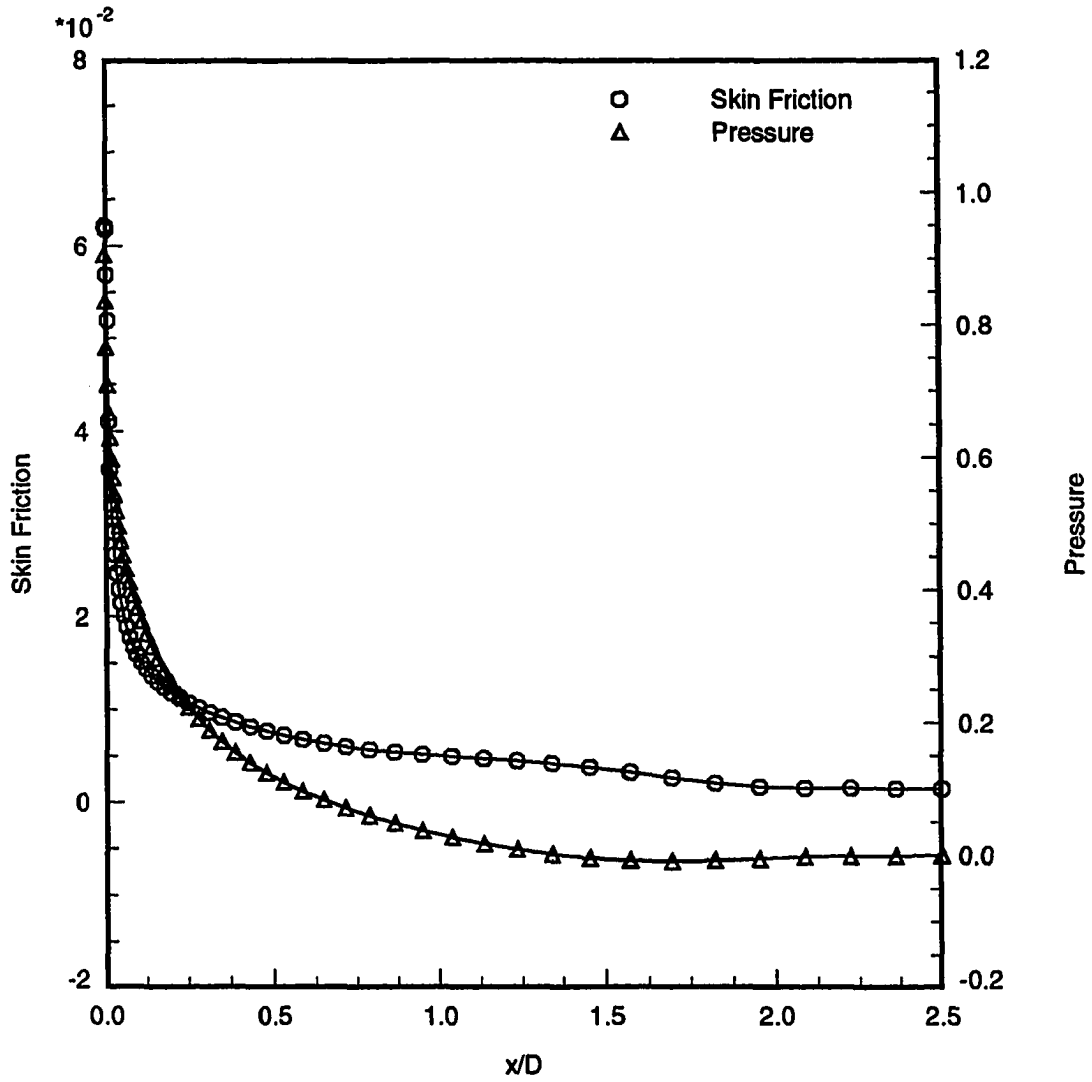


Figure 4.31: Nondimensionalized pressure and shearing stress on the erosion front due to the gas jet

stress in the overall removal mechanism. The high pressure value near the leading edge produces a relatively large ejection force while the shearing force effectively maintains a thin molten layer by continuously accelerating the fluid particles along the erosion front in the direction of the overall molten layer flow.

Molten layer The profile of the erosion front is shown in Fig. 4.33 in terms of the streamlines plot. Due to the narrowness of the molten layer, the streamlines are shown in 4 sections, each of which is $0.625t$, where t is the thickness of the plate. This steady state erosion front profile is determined when the residual defined by

$$\text{Residual} = \sqrt{\sum_{i=2}^{I-1} \sum_{j=2}^{J-1} |u_{i,j}^{n+1} - u_{i,j}^n|^2} \quad (4.5)$$

has dropped 4 orders of magnitude. The thickness of the layer varies from 0 at the top to approximately 1.5×10^{-4} m at the bottom. Therefore, for most part, the thickness of the molten layer is of the order of 10^{-5} m. This is consistent with the results obtained by Vicanek *et al.* [72]. However, contrary to the expectation of a somewhat curved erosion front [32, 72], the profile of the erosion front is observed to be relatively flat. The incident angle of the laser beam distribution along the erosion front is shown in Fig. 4.34. The incident angle varies within the range of 82° to 84° . This can be attributed to the magnitude of the pressure and shearing forces that act on the erosion front. Any waviness in the erosion front will essentially be smoothed out. Furthermore, the contribution due to surface tension is small in comparison to the effects due to pressure and shearing stress of the gas jet.

On the other hand, an argument can be made that the planar profile of the erosion front is a direct consequence of a planar melt interface that is assumed in the present model. However, experimental observations, such as the one performed in parallel with this study, do show a planar melt interface. This can be attributed to the thickness (or more

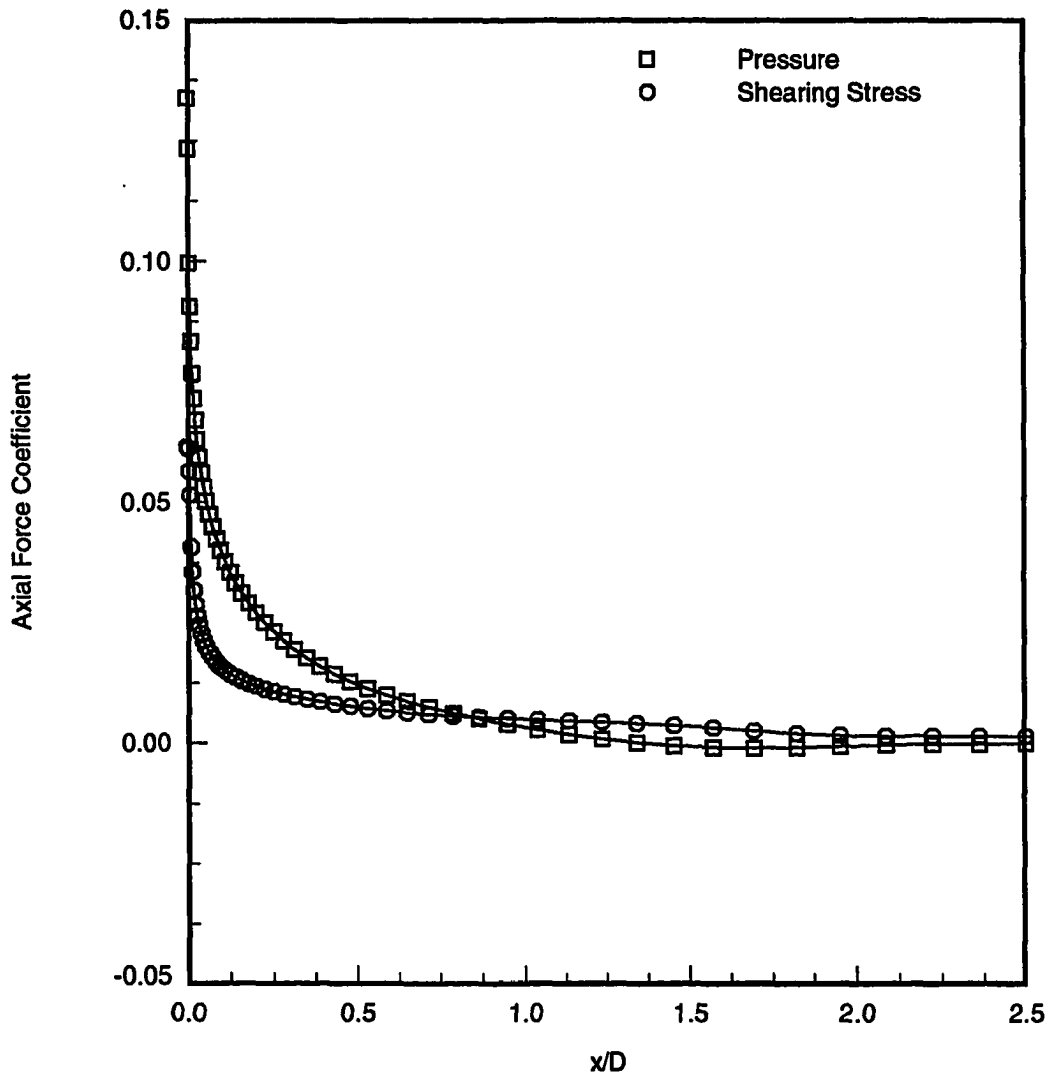


Figure 4.32: Axial force coefficient distributions on the erosion front due to pressure and shearing stress of the gas jet

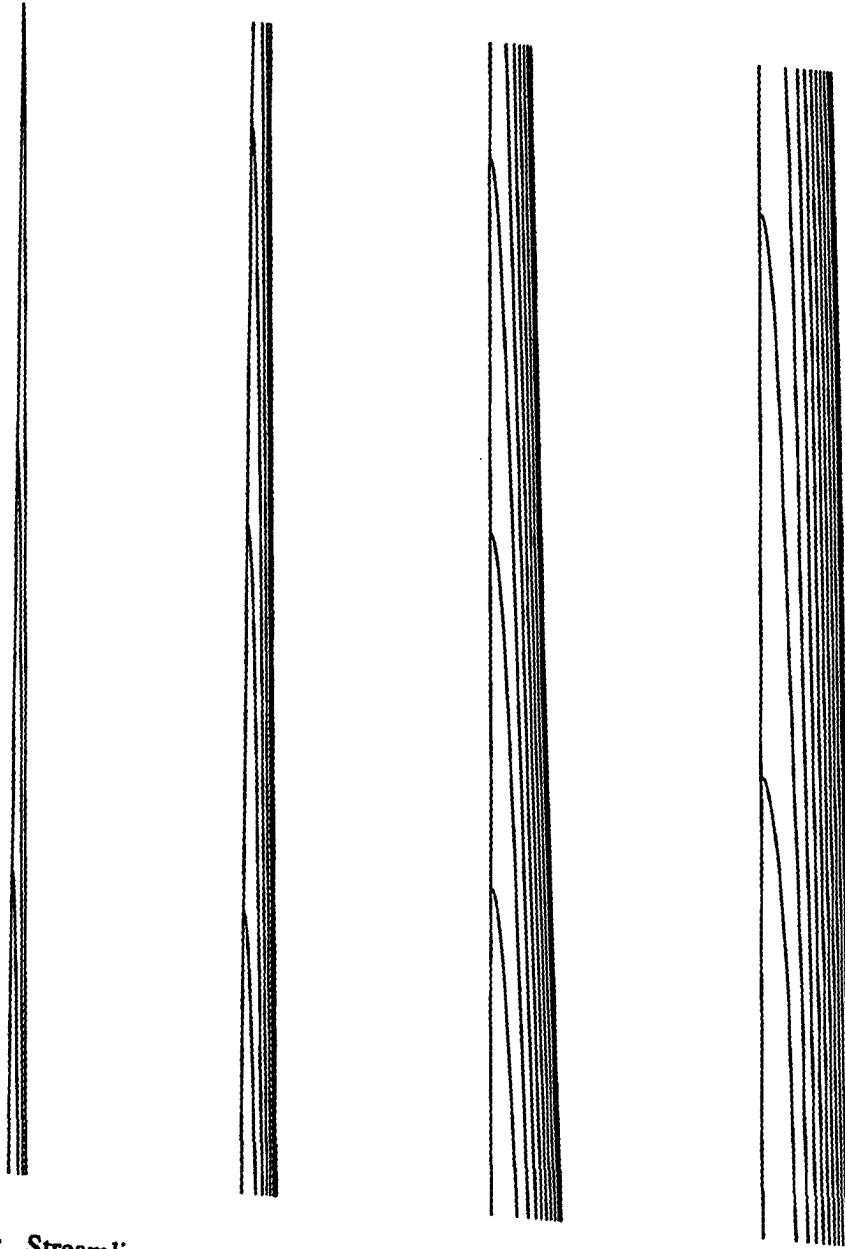


Figure 4.33: Streamlines within the molten layer shown in sections of $0.625t$ from left to right

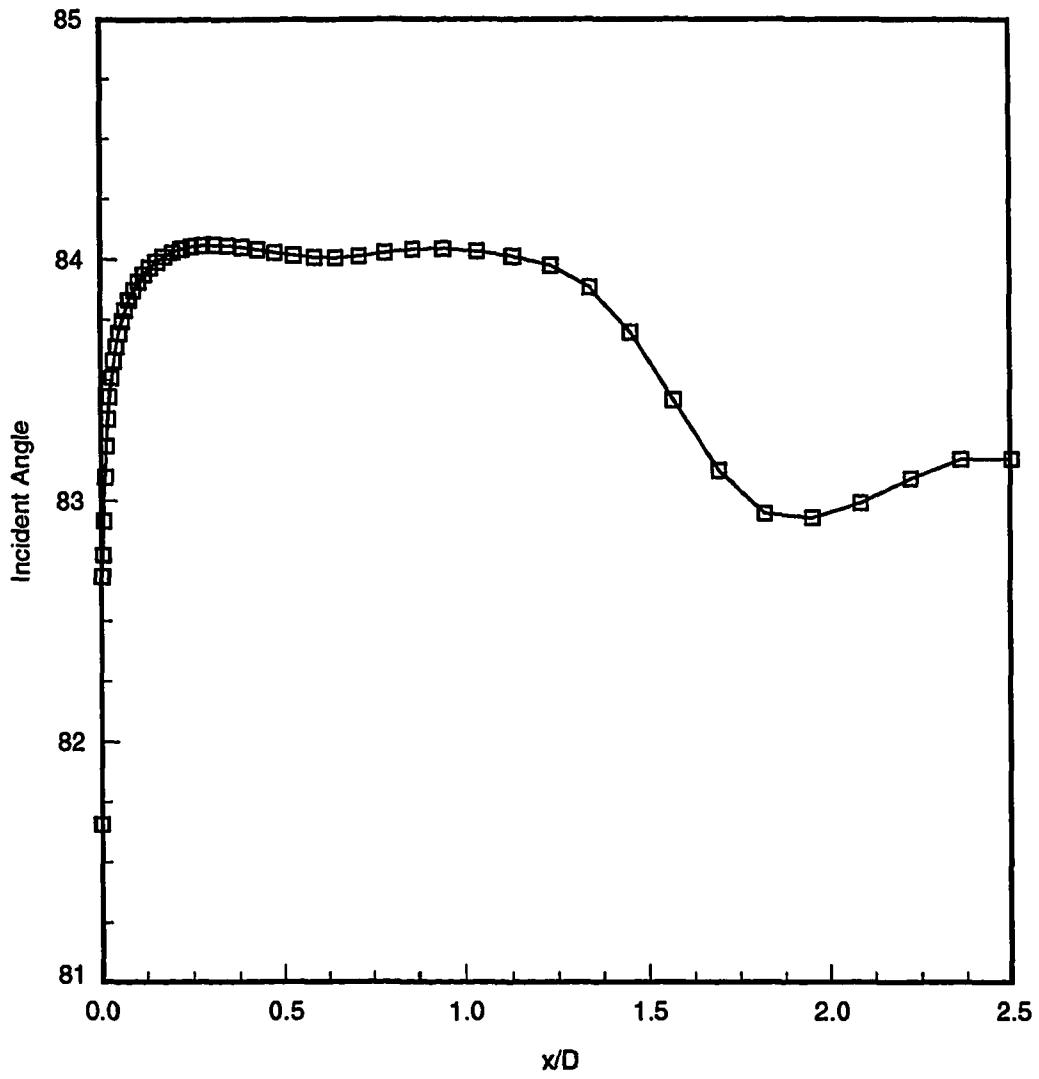


Figure 4.34: Variation of laser beam incident angle along the erosion front

appropriately here, the “thinness”) of the molten layer and the nature of the laser-material coupling at the erosion front. First, the “thinness” would imply a more effective heat transfer across the molten layer to the melt interface. It also implies that the shape of the erosion front would conform closely to the shape of the melt interface. Second, any curvature in the melt interface represents an unstable condition. This can be illustrated in Fig. 4.35. For a concave profile, the incident angle would be bigger—in comparison to a planar profile—at the top ($\alpha > \beta$) and would be smaller at the bottom ($\alpha < \beta$) of the erosion front. Hence, the laser-material coupling (recall that reflectivity is a direct function of the angles of incident α and β) is enhanced at the bottom and is degraded at the top relative to a planar profile. The energy balance would produce positive v_n (see Fig. 4.35) at the top and negative v_n at the bottom of the melt interface. Recall that v_n is the relative velocity of the melt interface with respect to the cutting speed. Consequently, the concave profile would tend to become planar. A similar argument can be made for a convex profile and the same conclusion is arrived at.

It has been suggested [73] that the striation pattern (see Fig. 4.36) on the edges of the kerf is caused by the unsteady motion of the molten layer. Vicanek *et al.* [72], based on stability analysis, concluded that the instability of the molten layer is more prominent when there is a large pressure gradient on the surface of the erosion front. However, this instability is not observed in the present calculation even though the pressure distribution on the erosion front, as shown in Fig. 4.31, shows a large pressure gradient. Furthermore, the “thinness” ($\mathcal{O}(10^{-5} \text{ m})$) of the molten layer at the leading edge, despite any oscillatory motion, could not account for the apparent wavelength ($\mathcal{O}(10^{-4} \text{ m})$) of the striation ripples. Rather, the striation pattern is caused, as suggested by Arata *et al.* [7], by the continuous melting in the direction perpendicular to the cut direction after the laser beam has passed.

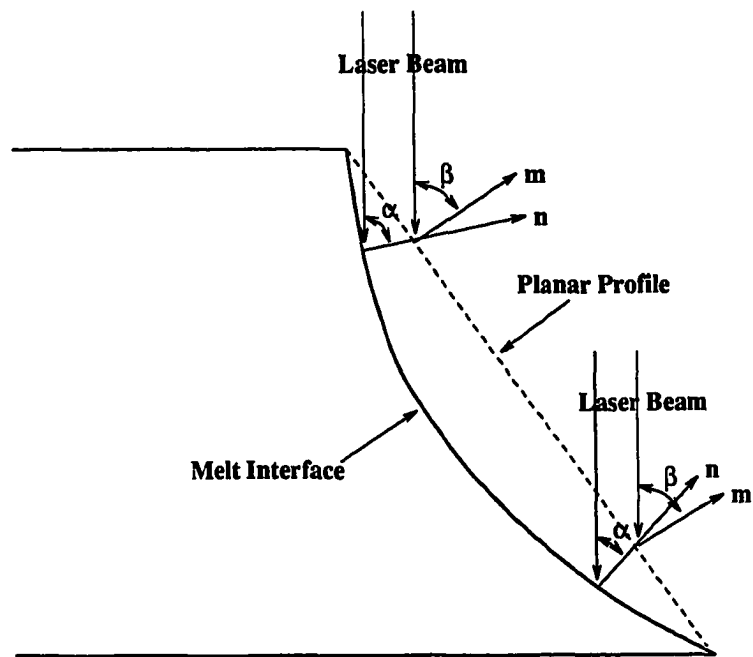


Figure 4.35: Curvature effects on the laser-material coupling at the melt interface

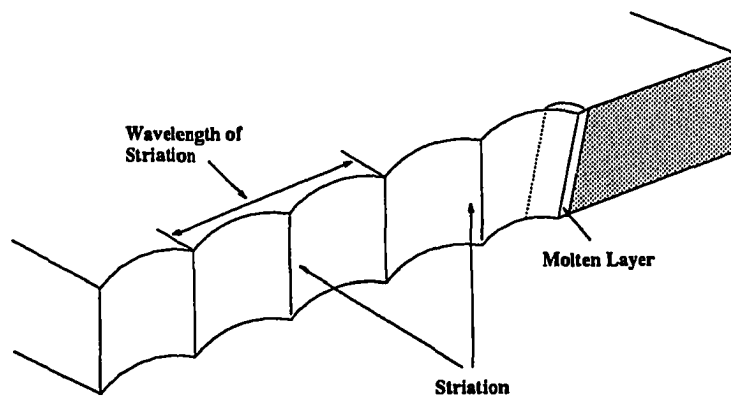


Figure 4.36: Typical striation pattern on the edges of the kerf

Therefore, any instability, if it occurred, is a *result* of the striation and not the *cause* for the striation.

This can be illustrated in the time evolution plot (see Fig. 4.37) of the erosion front profiles subjected to a pressure perturbation (a 10 percent increase in the pressure distribution) at the erosion front. The series of waves that are generated propagate downstream on the erosion front and eventually, the profile becomes planar. Had the perturbation been of a periodic nature, a sustained oscillatory motion of the molten layer would have been obtained. The perturbation in the pressure distribution could certainly be realized by the periodic variation of the kerf width as a result of striation. This, in effect, creates a pulsated flow through the kerf.

The nondimensionalized heat flux due to the various sources are shown in Fig. 4.38. The heat fluxes are nondimensionalized according to

$$q' = \frac{\bar{q}' D}{k_m T_m}$$

where D , k_m , and T_m are the reference length, thermal conductivity at T_m , and the melting point of iron respectively. The majority of the heat input, at least in the present modal case, is provided by the laser beam. However, it is interesting to note the distributions of both sources along the erosion front. Because of the spatial variation of the laser intensity, the heat flux in the vicinity of the leading edge is provided primarily by oxidation reactions between the molten material and the oxygen jet. The total contribution due to oxidation is only 18 percent of the total contribution due to laser beam. This, perhaps, indicates an non-optimum cutting conditions. As will be shown later, a large fraction of the total heat input is lost through conduction into the solid phase. It is reported that at optimum cutting conditions, the contribution due to oxidation could be as large as 60 percent [15]. On the other hand, convective heat loss is small except near the leading edge, and radiative heat

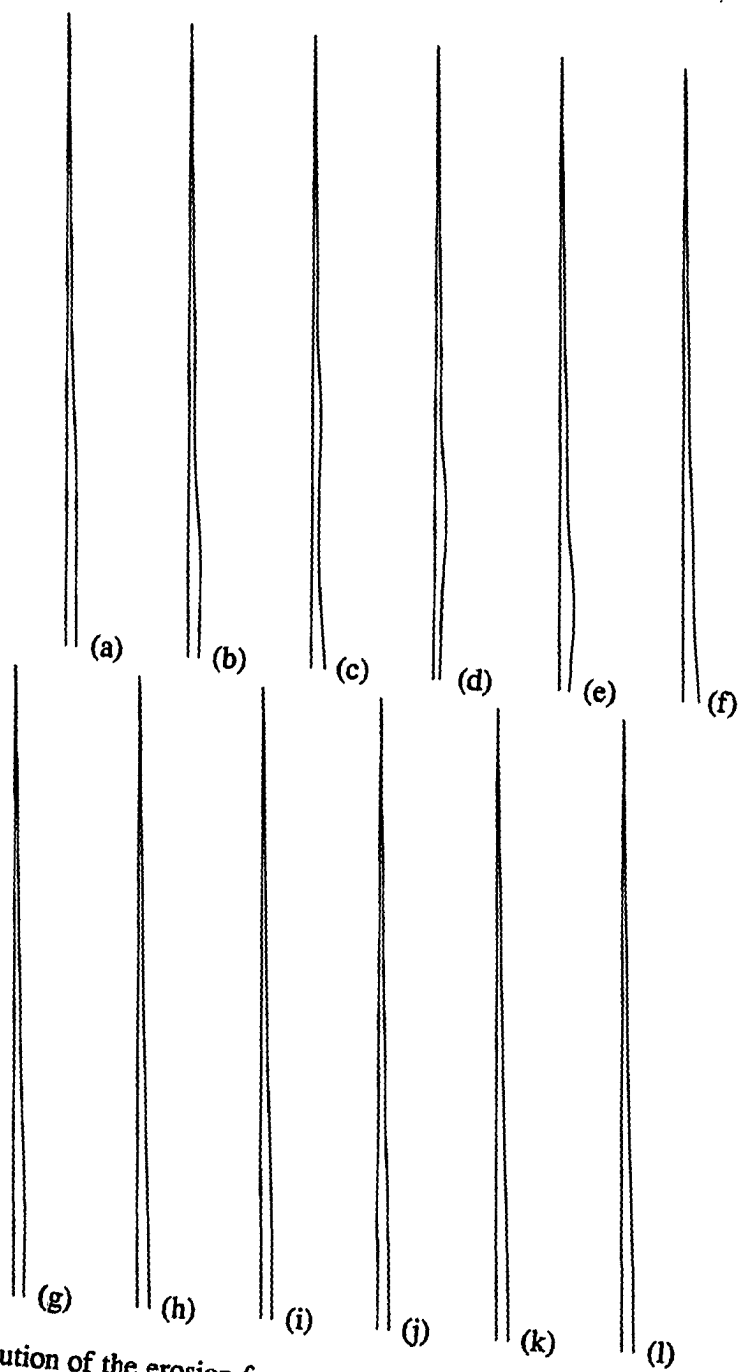


Figure 4.37: Evolution of the erosion front profile subjected to a sustained pressure disturbance ($\Delta t = 0.16$)

loss is almost negligible.

The temperature distribution on the erosion front is shown in Fig. 4.39. The location of the peak temperature corresponds to the location of the peak laser beam energy input. For the present case, the maximum temperature is calculated to be approximately 3300 K. It should be pointed out that the present calculation considers only the two-dimensional plane of the molten layer and therefore, lateral heat losses are not included. This implies that the temperature of 3300 K represents the theoretical maximum temperature that can be attained given the present cutting conditions. Hence, the assumption to neglect any material lost due to evaporation can certainly be justified because the temperatures are below the critical point.

The nondimensionalized temperature distributions (T/T_m) across the molten layer at various x/D locations are shown in Fig. 4.40. Note that the y direction is scaled with the thickness of the molten layer (Y) at the respective x/D locations. The corresponding nondimensionalized velocity magnitude distributions (V/u_r) is shown in Fig. 4.41.

The temperature variation within the molten layer is small near the leading edge but as the thickness increases, so does the temperature variation. Furthermore, the variation is relatively linear except for the region near the trailing end of the molten layer. Similar characteristics are observed for the velocity magnitude distributions. The linear variations of temperature imply that conduction is the mode for which heat is transferred from the erosion front to the melt interface. This is to be expected since the normal velocity component is almost zero, hence, convection heat transfer does not occur. It is interesting to note that the maximum velocity did not occur at the exit end of the molten layer. This is due to back pressure that is imposed as the exit boundary condition. Essentially, the fluid particles in the molten layer decelerate to match the exit pressure.

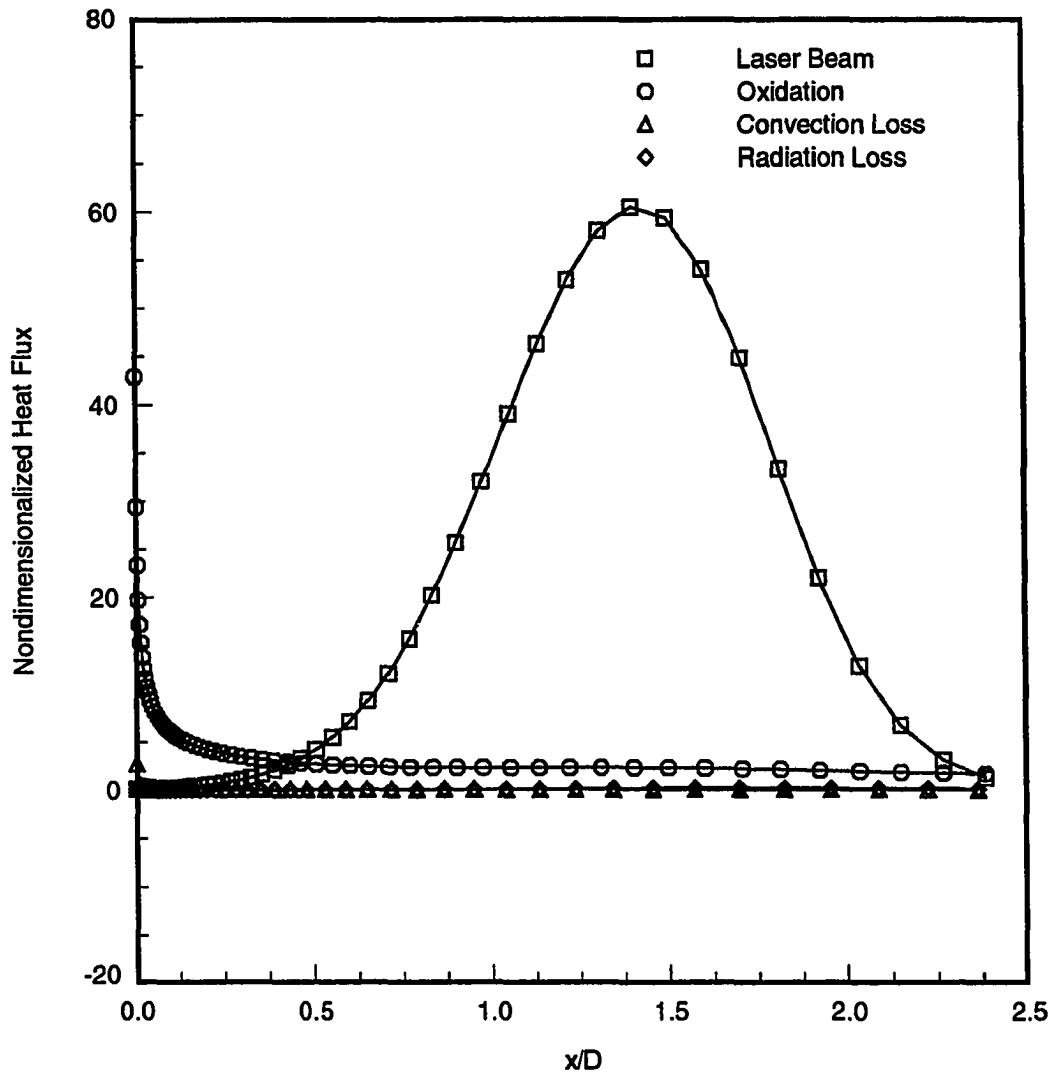


Figure 4.38: Nondimensionalized heat flux at the erosion front due to laser beam, oxidation, convection, and radiation losses

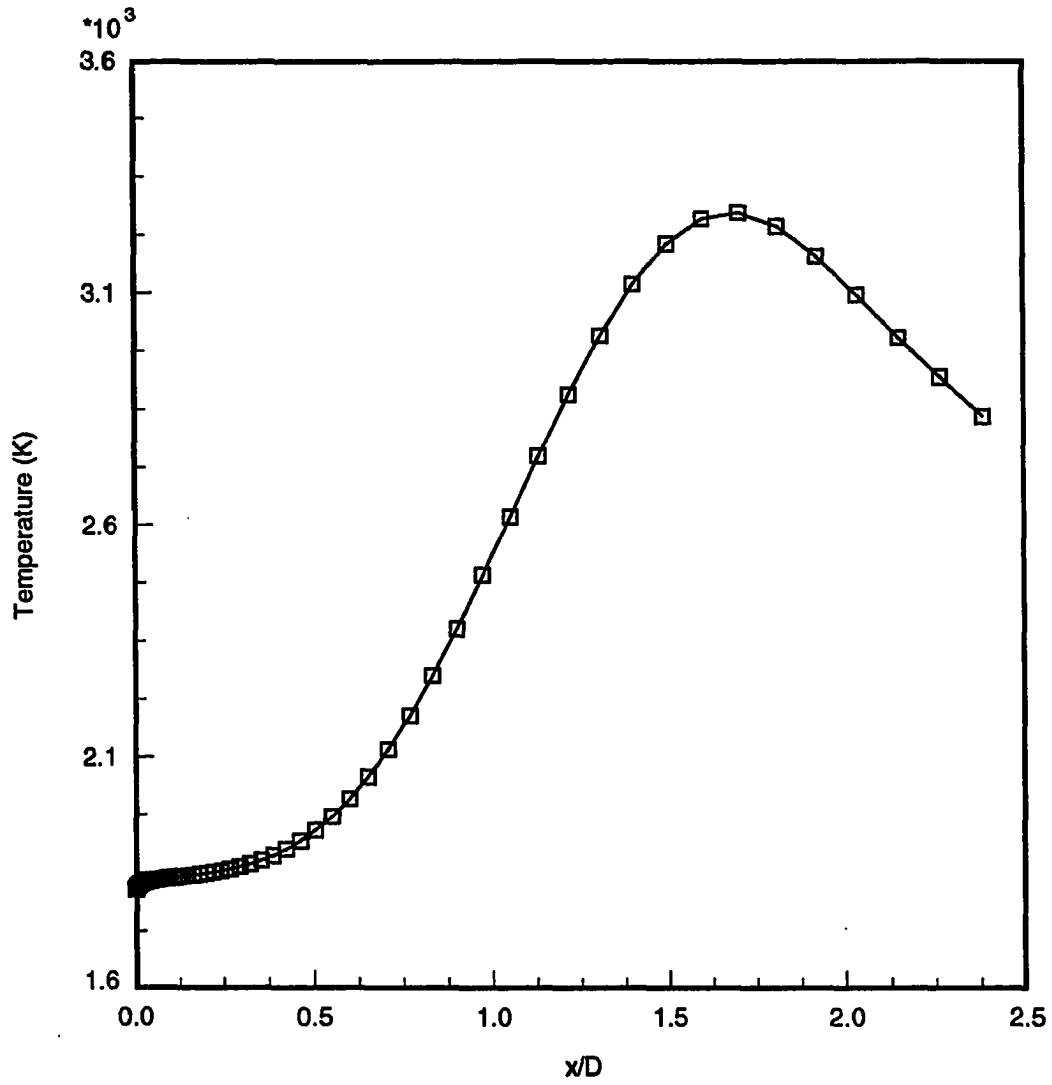


Figure 4.39: Temperature distribution at the erosion front

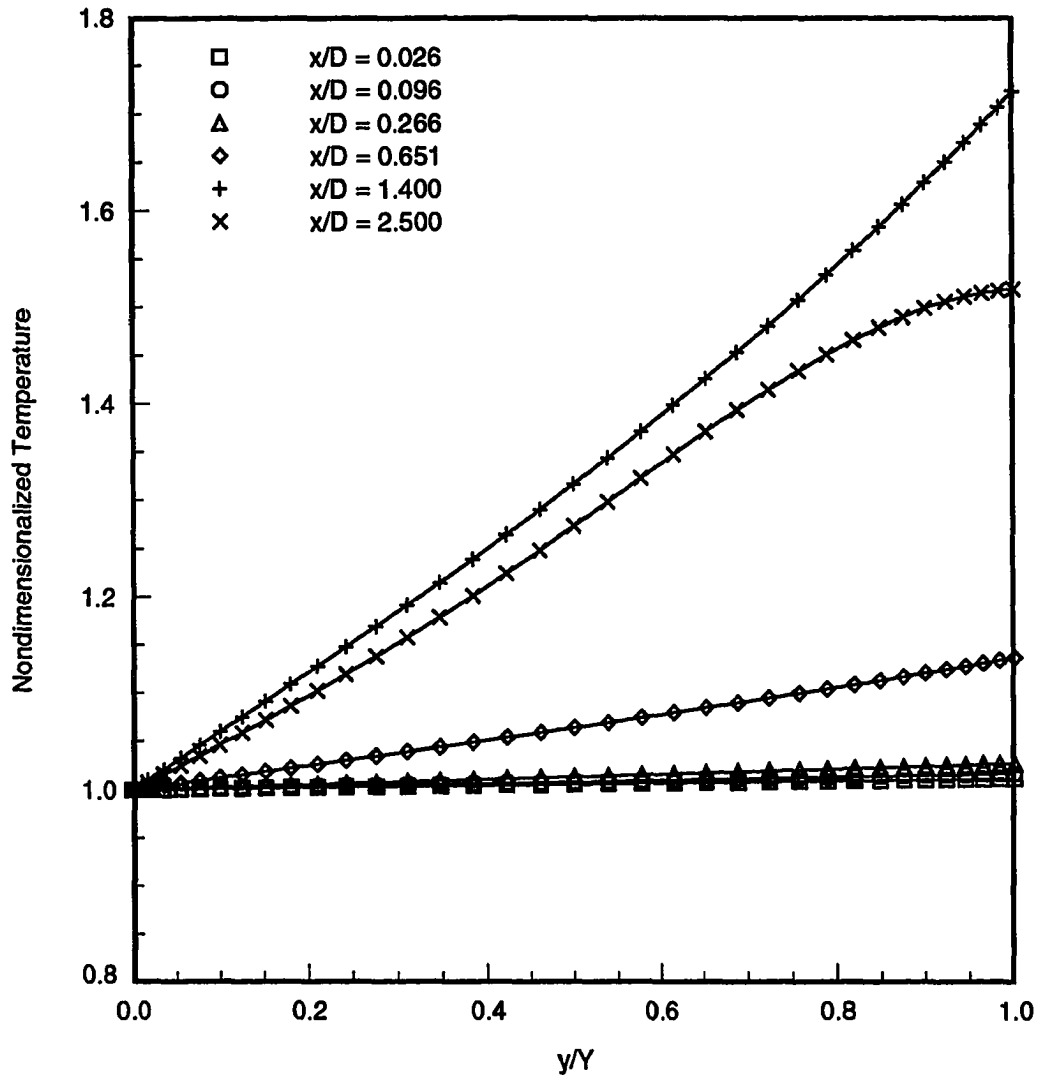


Figure 4.40: Nondimensionalized temperature across the molten layer at various x/D locations

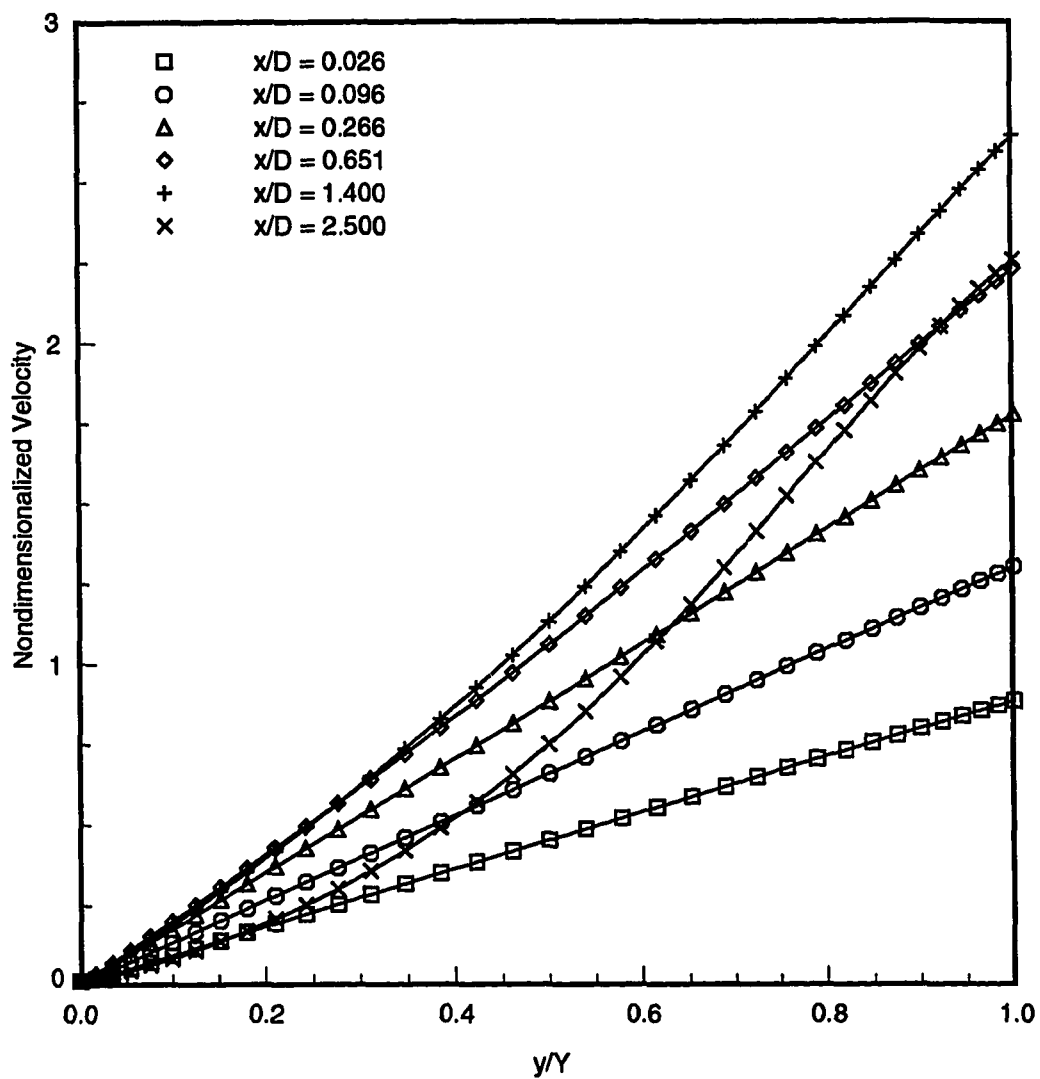


Figure 4.41: Nondimensionalized velocity magnitude across the molten layer at various x/D locations

The nondimensionalized total heat flux input at the erosion front and the nondimensionalized heat flux lost due to conduction into the solid phase at the melt interface are shown in Fig. 4.42. The conduction heat flux is defined as

$$q'_c = \left(\nabla T_l - \frac{\vec{v}_c}{Ste} \right) \cdot \hat{n} \quad (4.6)$$

The Stefan number (Ste) in the present context is defined as

$$Ste = \frac{\alpha_r C_p T_r}{D \Delta H_f u_r}$$

where ΔH_f is the latent heat of fusion, u_r is the reference velocity, α_r is the reference thermal diffusivity, T_r is the reference temperature, and C_p is the heat capacity. With the melting point as the reference, the Stefan number is calculated to be 0.013. The nondimensionalized advection heat flux due to the ejection of the molten material at the exit plane of the molten layer is shown in Fig. 4.43. The advection heat flux is calculated from

$$q'_a = \frac{D u_r}{\alpha_r} u_e T \quad (4.7)$$

where u_e is the velocity at the exit plane of the molten layer.

In principle, the heat input in the laser cutting process is used to heat up the solid phase material to the melting point and to bring about a phase change. Any excess heat is lost through conduction into the solid phase and through advection with the ejected material. The magnitude of each can be obtained by integrating the respective distributions shown in Figs. 4.42 and 4.43. The percentages for the conduction loss, advection loss, and phase change are summarized in Table 4.2. By far, conduction loss represents 50 percent of the total heat input. Advection loss accounts for about 45 percent and a mere 5 percent is actually used in the phase change. This is also indicated by the value of the Stefan number.

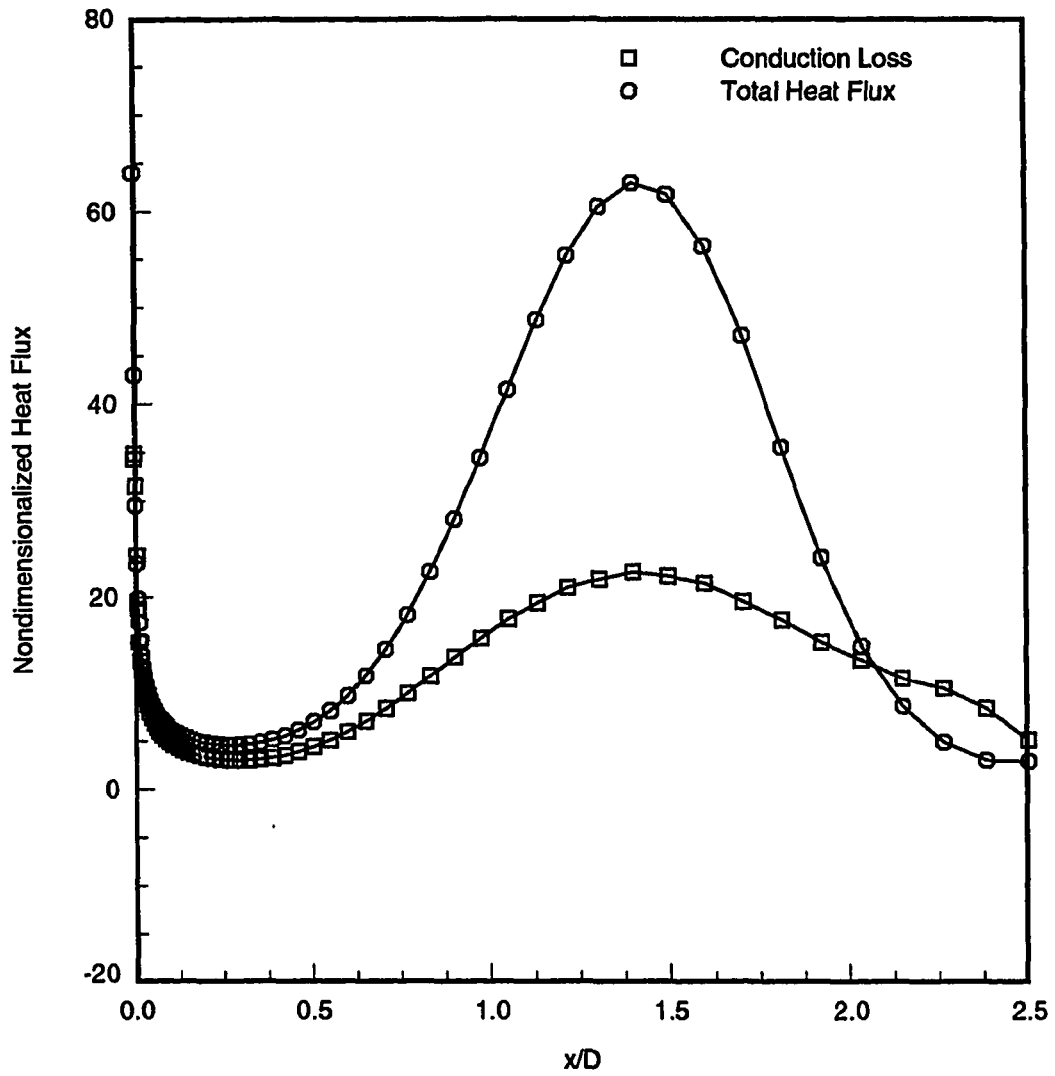


Figure 4.42: Nondimensionalized heat flux due to laser beam and oxidation, and conduction loss in the solid phase

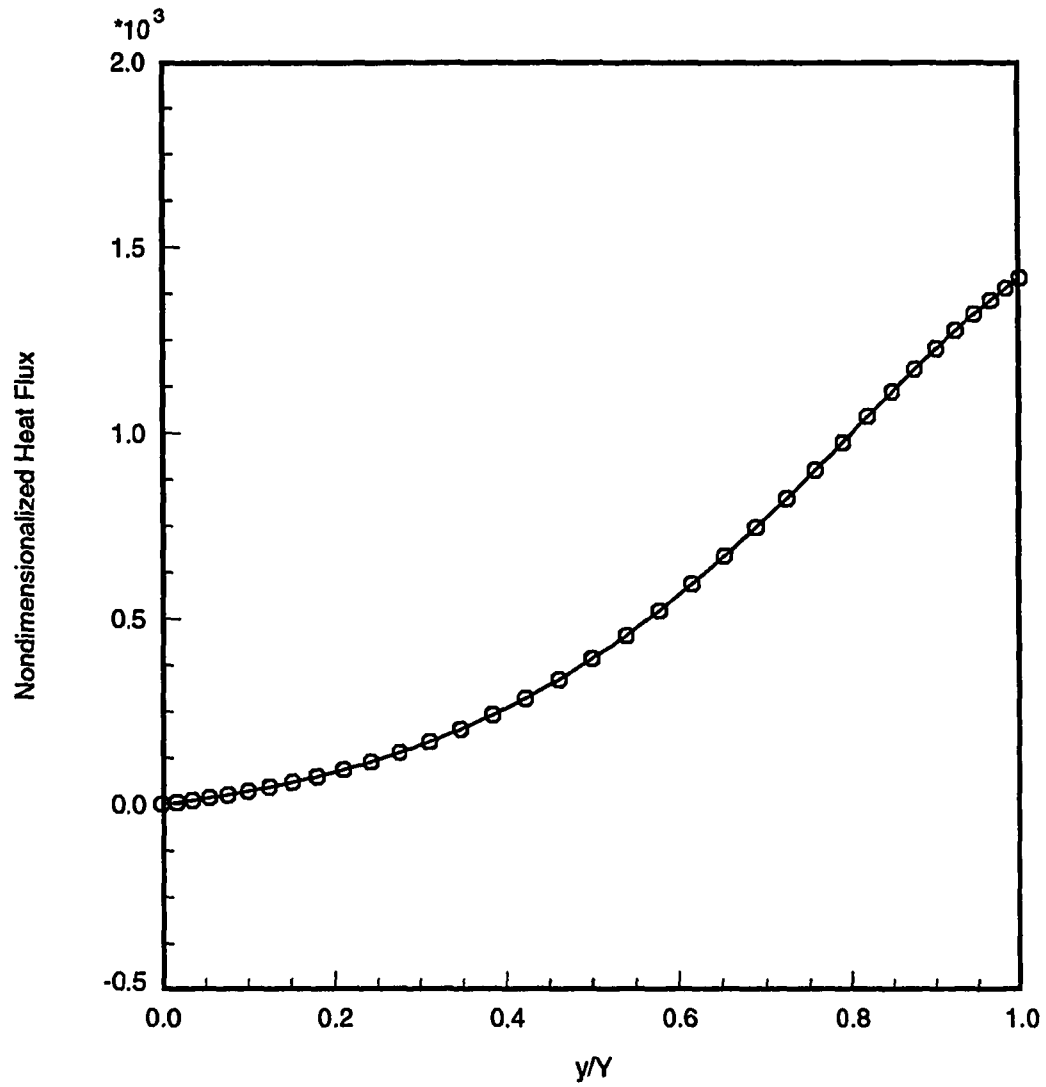


Figure 4.43: Nondimensionalized heat flux due to advection at the exit plane of the molten layer

Table 4.2: Percentages of heat due to conduction, advection, and phase change with respect to the total heat input

Conduction Loss into the solid	49.9%
Advection Loss at exit plane	45.2%
Phase Change at the melt interface	4.9%

However, of the 50 percent of the heat input that is lost through conduction into the solid, a large fraction is actually used to heat up the solid material to the melting temperature. For example, if the solid material is assumed to be initially at 300 K, the heat flux that is required to raise the temperature to the melting point can be estimated from

$$q'_{\Delta T} = \frac{Du_r}{\alpha_r} \vec{v}_c \cdot \hat{n} (T_m - T_r) \quad (4.8)$$

The result indicates that of the 50 percent that is lost to conduction, about 45 percent of it is used to heat up the solid material from the room temperature to the melting point.

It is also interesting to note the distribution of the conduction loss. Almost the entire heat flux provided by oxidation and laser beam at the leading edge is lost into the solid phase. This is due, partially, to the relatively small amount of heat flux needed to achieve the phase change. However, the heat loss through advection becomes more prominent as the velocity of the molten layer increases due to the continuous acceleration caused by the shearing stress of the gas jet. In fact, the magnitude of the heat flux that is lost due to conduction is higher than the input heat flux near the trailing end. This indicates the important role of advection in the overall heat transfer mechanism across the molten layer. Without the advection, a negative net heat flux would occur at the melt interface near the exit plane and the cutting process would cease near the trailing edge.

Furthermore, the conduction heat loss is maximum in the vicinity of the peak laser

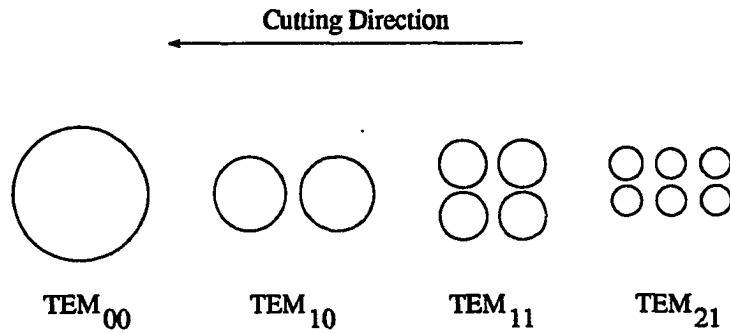


Figure 4.44: Various TEM modes and their spatial energy distributions

intensity. This observation suggests a way to optimize the spatial variation of the laser beam intensity. Although heat lost through conduction into the solid material is a necessary aspect of the overall cutting process (i.e., to raise the temperature of the solid material to the melting point), its distribution could be affected such as to minimize the excess heat loss. The excess heat loss refers to the portion of the total conduction heat loss that is not used to raise the temperature at the rate required to sustain the cutting process. This would imply the use of non-Gaussian beams, at least in the direction of the cut, where the spatial variation of the laser beam intensity is more diffused. This should improve the conduction heat loss characteristics. On the other hand, non-Gaussian beam, for example the Lorentzian distribution, may give rise to other difficulties such as producing a small focal spot size. Hence, the laser power density may not be as high as that which can be achieved with a Gaussian beam. Alternatively, multimode beam may be used, and in particular, the TEM_{10} mode (see Fig. 4.44).

CHAPTER 5. CONCLUSIONS

A novel procedure for computation of reactive gas assisted laser cutting of metal has been presented. Instead of using lumped capacitance approach, the appropriate governing equations in the molten metal and gas jet regions are solved in the present method. The interactions at the erosion front such as laser-material coupling, oxidation reactions, and heat losses through convection and radiation are treated intrinsically in the procedure. The erosion front itself is modeled as a free surface and is allowed to deform according to the momentum transfer. The approximation of the gas flow above the workpiece as a jet impingement problem provides an effective means for calculating the fluid dynamics and heat transfer phenomena of the gas jet.

The Newton-Raphson iteration method provides an elegant approach for the temporal discretization of the governing equations. Good convergence characteristics are obtained despite the various approximations that are made in developing the iterative scheme. The spatial discretization utilizes both central and upwind differenced schemes. Furthermore, the introduction of Roe's "Superbee" flux limiter effectively removed any oscillation about the discontinuities. Excellent comparison with existing results in all test cases are obtained and thus validated the present numerical algorithm.

Computed results for the laser cutting of a 6.35 mm thick low carbon steel plate (AISI 1008) with an oxygen jet provided considerable insight on the cutting process. The erosion

front showed a relatively flat profile and the thickness of the molten layer is of the order of 10^{-5} m. The "thinness" of the molten layer is thought to enhance the overall heat transfer across the molten layer. The "thinness" of the molten layer also suggested that the striation pattern observed along the edges of the kerf could not be due to the unsteady motion of the molten layer. It is interesting to note that the unsteady motion in the molten layer could be induced by introducing a pressure disturbance.

The maximum temperature (3300 K) at the erosion front showed that material removal through evaporation is negligibly small. Hence, the bulk of the molten material is removed through the combined effects of the pressure gradient and shearing stress of the jet flow within the kerf. The distributions of the axial force coefficients due to pressure and shearing stress indicates that the removal is effected by both the pressure and shearing stress. The effects due to the pressure gradient is confined to the leading edge of the erosion front while the effects due to shearing stress are responsible for maintaining a thin and relatively flat erosion front profile.

The distributions of the various heat fluxes along the erosion front demonstrated the significance of the contribution by oxidation reactions. Because of the spatial variation of the laser beam intensity, the heat flux near the leading edge of the erosion front is provided primarily by oxidation reactions. The effects due to the laser beam is confined to the midspan of the molten layer. Furthermore, heat losses due to convection and radiation are found to be almost negligible.

An energy balance indicates that 50 percent of the heat flux from the laser beam and oxidation is lost due to conduction in the solid phase. The energy needed for the phase change accounted for only 5 percent of the total energy input. It was observed that the large conduction loss was due to the spatial distribution of the Gaussian beam. It has been

suggested that the heat loss can be reduced by using multi-mode beam in the direction of the cut.

The present results are arrived at with certain assumptions regarding the overall laser cutting process. For example, the location of the laser beam centerline (or nozzle centerline) with respect to the leading edge of the erosion front is assumed at $0.15D$ where D is the diameter of the nozzle exit. This offset distance has a direct influence on the location of the peak laser intensity along the erosion front. However, despite this uncertainty, the results obtained would still indicate a large loss through conduction into the solid. Perhaps this is more an indicator for a non-optimum cutting situation with the present set of cutting parameters. High speed photography of the cutting zone can provide a better estimation of this offset distance.

The reflectivity at the erosion front assumed in the present calculation may not be correct at high temperatures. Further experimental investigation can be devoted to characterizing the dependency of reflectivity on the angle of incident at elevated temperatures. The dependency of reflectivity on temperature should also be obtained.

The assumption of a planar profile for the melt interface could be relaxed in future studies. The profile can be determined based on the energy balance. However, this would require the knowledge of the heat conduction characteristics in the solid phase. Hence, additional equations, along with a suitable correlation for the heat lost due to convection effects of the jet on the workpiece surface, must be solved to obtain the conduction heat loss.

REFERENCES

- [1] Graham, R. E., "Why A Laser Cutting System: A Comparison With More Conventional Cutting Systems," SPIE Vol. 527, *Applications of High Power Lasers*, 1985, pp. 6-10.
- [2] Rutt, J. P., "Applying Industrial Lasers for Improved Manufacturing Productivity," SPIE Vol. 744, *Lasers in Motion for Industrial Applications*, 1987, pp. 48-55.
- [3] Belforte, D., "Economic Justification of Industrial Laser Applications," SPIE Vol. 527, *Applications of High Power Lasers*, 1985, pp. 18-27.
- [4] Svelto, O., and Hanna, D. C., *Principles of Lasers*, Plenum Press, New York, 1982.
- [5] Luxon, J. T., and Parker, D. E., *Industrial Lasers and Their Applications*, Prentice Hall, Englewood Cliffs, New Jersey, 1992.
- [6] Schuöcker, D., "Laser Cutting," *The Industrial Laser Annual Handbook*, Pennwell Publishing Co., Tulsa, Oklahoma, 1986, pp. 87-107.
- [7] Arata, Y., Maruo, H., Miyamoto, I., and Takeuchi, S., "Dynamic Behavior in Laser Gas Cutting of Mild Steel," *Transactions of the Japan Welding Research Institute*, Vol. 8, No. 2, 1979, pp. 15-26.
- [8] Arata, Y., and Miyamoto, I., "Some Fundamental Properties of High Power CO_2 Laser Beam as a Heat Source," *Transactions of the Japan Welding Research Institute*, Vol. 3, No. 1, 1974, pp. 1-20.
- [9] Sullivan, A. B. J. and Houldcroft, P. T., "Gas-Jet Laser Cutting," *British Welding Journal*, Vol. 14, 1967, pp. 443-445.
- [10] Roessler, D. M., and Gregson, V. G., "Reflectivity of Steel at $10.6\mu\text{m}$ Wavelength," *Applied Optics*, Vol. 17, No. 7, 1978, pp. 992-993.

- [11] Belforte, D., *Industrial Laser Annual Handbook*, Pennwell Books, Tulsa, Oklahoma, 1990.
- [12] Olsen, F. O., "Studies of Sheet Metal Cutting with Plane-Polarized CO₂ Laser," *Optoelectronics in Engineering*, Waidelich, W. (Ed.), Springer Verlag, Berlin, Germany, 1982, pp. 227–231.
- [13] Rothe, R., and Sepold, G., "Important Requirement on Laser Beam Cutting Systems for Cutting Thick Plates," *Proceedings of International Conference on Laser Advanced Material Processing*, Osaka, Japan, 1987, pp. 251–253.
- [14] Sepold, G., and Rothe, R., "Laser Beam Cutting of Thick Steel," *Proceedings of ICALEO*, Los Angeles, November 1983, pp. 156–159.
- [15] Steen, W. M., and Kamalu, J. M., "Laser Cutting," *Laser Material Processing*, Bass, M. (Ed.), North-Holland Publishing Company, Amsterdam, 1983, pp. 15–112.
- [16] Duley, W. W., *Laser Processing and Analysis of Materials*, Plenum Press, New York, 1983.
- [17] Ward, B. A., "Supersonic Characteristics of Nozzles Used with Lasers for Cutting," *Proceedings of ICALEO*, Boston, November 1984, pp. 94–101.
- [18] Nielsen, S. E., "Laser Cutting with High Pressure Cutting Gases and Mixed Cutting Gases," Ph.D. Thesis, Technical University of Denmark, Denmark, 1985.
- [19] Fieret, J., Terry, M. J., and Ward, B. A., "Overview of flow dynamics in gas-assisted laser cutting," SPIE Vol. 801, *High Power Lasers*, 1987, pp. 243–250.
- [20] Forbes, N., "The Role of Gas Nozzle in Metal Cutting with CO₂ Lasers," *Laser 75 Optoelectronics Conference Proceedings*, Munich, Germany, June 1975, pp. 93–95.
- [21] Arata, Y., Maruo, M., Miyamoto, I., and Takuechi, S., "New Laser Gas Cutting Technique for Stainless Steel," *Plasma, Electron and Laser Beam Technology*, American Society for Metals, 1986, pp. 415–426.
- [22] Chryssolouris, G., and Choi, W. C., "Gas Jet Effects on Laser Cutting," SPIE Vol. 1042 *CO₂ Lasers and Applications*, 1989, pp. 86–96.
- [23] Hsu, M. J., "Analytical and Experimental Studies of Advanced Laser Cutting Techniques," Ph.D. Dissertation, Iowa State University, Ames, 1992.
- [24] Ketting, H. O., and Olsen, F. O., "High Pressure Off-axial Laser Cutting of Stainless Steel and Aluminum," *Proceedings of the International Conference on Laser Advanced Material Processing*, Nagaoka, Japan, 1992, pp. 607–612.

- [25] Molian, P. A., "Laser Cutting of Thick Metallic Solids," *Proceedings of International Conference on Laser Advanced Materials Processing*, Osaka, Japan, May 1987, pp. 245–250.
- [26] Mazumber, J., "The State-of-Art of Laser Material Processing," *Proceedings of Interdisciplinary Issues in Material Processing and Manufacturing*, Boston, Massachusetts, 1987, pp. 599–630.
- [27] Decker, I., Ruge, J., and Atzert, U., "Physical Models and Technological Aspects of Laser Gas Cutting," SPIE Vol. 455, *Industrial Applications of High Power Lasers*, 1983, pp. 81–87.
- [28] Babenko, V. P., and Tychinskii, V. P., "Gas-Jet Laser Cutting," *Soviet Journal of Quantum Electronics*, Vol. 2, No. 5, April 1973, pp. 399–410.
- [29] Bunting, K., and Cornfield, G., "Toward a General Theory of Cutting: A Relationship between the Incident Power Density and the Cutting Speed," *Journal of Heat Transfer*, February 1975, pp. 116–122.
- [30] Petring, D., Abels, P., Beyer, E., and Herziger, G., "Werkstoffbearbeitung mit Laserstrahlung," *Feinwerktechnik & Messtechnik*, Vol. 96, 1988, pp. 364–372.
- [31] Schuöcker, D., and Abel, W., "Material Removal Mechanism of Laser Cutting," SPIE Vol. 455, *Industrial Applications of High Power Lasers*, 1984, pp. 88–95.
- [32] Vicanek, M., and Simon, G., "Momentum and Heat Transfer of and Inert Gas Jet to the Melt in Laser Cutting," *Journal of Physics D: Applied Physics*, Vol. 20, 1987, pp. 1191–1196.
- [33] Sona, A., "Metallic Material Processing: Cutting and Drilling," *Applied Laser Tooling*, Soares, O. D. D., and Perez-Armor, M., (Eds.), Martinus Nijhoff Publisher, Dordrecht, Netherland, 1987, pp. 105–108.
- [34] Anderson, D. A., Tannehill, J. C., and Pletcher, R. H., *Computational Fluid Mechanics and Heat Transfer*, Hemisphere, New York, 1984.
- [35] Pulliam, T. H., "Efficient Solution Methods for the Navier-Stokes Equations," *Lecture Notes for the Von Karman Institute for Fluid Dynamics Lecture Series*, Brussels, Belgium, 1986.
- [36] Basu, B., and Srinivasan, J., "Numerical Study of Steady-State Laser Melting Problem," *International Journal of Heat and Mass Transfer*, Vol. 31, No. 11, 1988, pp. 2331–2338.

- [37] Bergman, T. L., and Webb, B. W., "Simulation of Pure Metal Melting with Bouyancy and Surface Tension Forces in the Liquid Phase," *International Journal of Heat and Mass Transfer*, Vol. 33, No. 1, 1990, pp. 139–149.
- [38] Tsai, M. C., and Kou, S., "Weld Pool Convection and Expansion due to Density Variations," *Numerical Heat Transfer, Part A*, Vol. 17, 1990, pp. 73–89.
- [39] Lacroix, M., and Arsenault, A., "Analysis of Natural Convection Melting of a Sub-cooled Pure Metal," *Numerical Heat Transfer, Part A*, Vol. 23, 1993, pp. 21–34.
- [40] Floryan, J. M., and Rasmussen, H., "Numerical Methods for Viscous Flows with Moving Boundaries," *Applied Mechanics Review*, Vol. 42, No. 12, December 1989, pp. 323–340.
- [41] Ivarson, A., Powell, J., and Magnusson, C., "The Role of Oxidation in Laser Cutting of Stainless and Mild Steels," *Journal of Laser Application*, Vol. 3, No. 3, 1991, pp. 41–45.
- [42] Schulz, W., Simon, G., and Vicanek, M., "Influence of the Oxidation Process in Laser Cutting," SPIE Vol. 801, *High Power Lasers*, 1987, pp. 331–336.
- [43] Iida, T., and Guthrie, R., *The Physical Properties of Liquid Metals*, Oxford University Press, New York, 1988.
- [44] Beyer, R. T., and Ring, E. M., "The Viscosity of Liquid Metals," *Liquid Metal: Chemistry and Physics*, Beer, S. Z. (Ed.), Marcel Dekker, Inc., New York, 1972, pp. 431–460.
- [45] Allen, B. C., "The Surface Tension of Liquid Metals," *Liquid Metal: Chemistry and Physics*, Beer, S. Z. (Ed.), Marcel Dekker, Inc., New York, 1972, pp. 161–212.
- [46] White, F. M., *Viscous Fluid Flow*, McGraw-Hill, Inc., New York, 1991.
- [47] Barillot, Ph., "Numerical Simulation of Crater Formation Heating by Laser Beam," *Numerical Heat Transfer, Part B*, Vol. 17, 1990, pp. 245–256.
- [48] Olsen, F. O., "Laser Cutting," SPIE Vol. 952, *Laser Technology in Industry*, 1988, pp. 572–581.
- [49] Incropera, F. P., and De Witt, D. P., *Fundamentals of Heat and Mass Transfer*, John Wiley and Sons, New York, 1990.
- [50] Kuo, K. K., *Principles of Combustion*, John Wiley and Sons, New York, 1986.

- [51] Powell, J., Ivarson, A., and Magnusson, C., "Laser Cutting of Steels: A Physical and Chemical Analysis of the Particles Ejected During Cutting," *Journal of Laser Applications*, Vol. 5, No. 1, 1993, pp. 25–31.
- [52] Chorin, A. J., "A Numerical Method for Solving Incompressible Viscous Flow Problems," *Journal of Computational Physics*, Vol. 2, 1967, pp. 12–26.
- [53] Rogers, S. E., and Kwak, D., "An Upwind Differencing Scheme for the Time-Accurate Incompressible Navier-Stokes Equations," AIAA Paper 88-2583, 1988.
- [54] Chang, J. L. C., and Kwak, D., "On the Method of Pseudo Compressibility for Numerically Solving Incompressible Flows," AIAA Paper 84-252, Jan. 1984.
- [55] Beam, R., and Warming, R. F., "An Implicit Finite-Difference Algorithm for Hyperbolic Systems in Conservation Law Form," *Journal of Computational Physics*, Vol. 22, 1976, pp. 87–110.
- [56] Osher, S., and Chakravathy, S., "Upwind Schemes and Boundary Conditions with Applications to Euler Equations in General Geometries," *Journal of Computational Physics*, Vol. 50, 1983, pp. 447–481.
- [57] Roe, P. L., "Approximate Riemann Solvers, Parameter Vectors, and Difference Schemes," *Journal of Computational Physics*, Vol. 43, 1981, pp. 357–372.
- [58] Tenpas, P. W., and Fletcher, R. H., "Solution of the Navier-Stokes Equations for Subsonic Flows Using a Coupled Space-Marching Method," AIAA Paper 87-1173-cp, 1987.
- [59] Rhie, C. M., "A Numerical Study of the Flow Past an Isolated Airfoil with Separation," Ph.D. Dissertation, University of Illinois, Urbana, 1981.
- [60] Acrivos, A., Leal, L. G., Snowden, D. D., and Pan, F., "Further Experiments on Steady Separated Flow Past Bluff Objects," *Journal of Fluid Mechanics*, Vol. 34, 1968, pp. 25–48.
- [61] Lim, C. K., "Numerical Simulation of Non-Lifting Flow over Two-Dimensional Elliptic Cylinders," MS Thesis, Iowa State University, Ames, 1991.
- [62] Lecointe, Y., and Piquet, J., "On the Use of Several Compact Methods for the Study of Unsteady Incompressible Viscous Flow Round a Circular Cylinder," *Computers & Fluids*, Vol. 12, No. 4, 1984, pp. 255–280.
- [63] Hirsch, C. *Numerical Computation of Internal and External Flows*, Vol. 2, John Wiley and Sons, New York, 1990.

- [64] Buning, P. G., Chiu, I. T., Obayashi, S., Rizk, Y. M., and Steger, J. L., "Numerical Simulation of the Integrated Space Shuttle Vehicle in Ascent," AIAA-Paper 88-4359-cp, August 1988.
- [65] Kayser, L. D., and Whiton, F., "Surface Pressure Measurements on a Boattailed Projectile Shape at Transonic Speeds," ARBRL-MR-03161, U. S. Army Ballistic Research Laboratory, March 1982.
- [66] Liou, M. S., "A Newton Upwind Method and Numerical Study of Shock Wave Boundary Layer Interactions," *International Journal for Numerical Methods in Fluids*, Vol. 9, 1989, pp. 747-761.
- [67] Green, J. E., "Interactions Between Shock Waves and Turbulent Boundary Layer," *Progress in Aerospace Sciences*, Kuchemann, D., et al. (Eds.), Vol. 11, Pergamon Press, Oxford, 1970.
- [68] Hankey, W. L., and Holden, M. S., "Two Dimensional Shock Wave-Boundary Layer Interactions in High Speed Flows," *AGARDograph* No. 203, 1975.
- [69] Adamson Jr, T. C., and Messiter, A. F., "Analysis of Two-Dimensional Interactions Between Shock Waves and Boundary Layers," *Annual Review in Fluid Mechanics*, Vol. 12, 1980, pp. 103-138.
- [70] Delery, J., and Marvin, J. G., "Shock-Wave Boundary Layer Interactions," *AGARDograph* No. 280, 1986.
- [71] Hakkinen, R. J., Greber, L., Trilling, L., and Abarbanel, S.S., "The Interaction of an Oblique Shock Wave with a Laminar Boundary Layer," NASA Memo 2-18-69W, 1959.
- [72] Vicanek, M., Simon, G., Urbassek, H. M., and Decker, I., "Hydrodynamical Instability of Melt Flow in laser Cutting," *Journal of Physics D: Applied Physics*, Vol. 20, 1986, pp. 140-145.
- [73] Schuöcker, D., "Dynamic Phenomena in Laser Cutting and Cut Quality," *Applied Physics B: Photophysics and Laser Chemistry*, Vol. 40, 1986, pp. 9-14.
- [74] Powell, J., "Guidelines and Data for Laser Cutting," *The Industrial Laser Annual Handbook*, Pennwell Publishing Co., Tulsa, Oklahoma, 1990, pp. 56-66.

APPENDIX EXPERIMENTAL INVESTIGATION

The laser experiments considered in the present study are configured for the characterization of the melt interface profile. Recall that the melt interface in the present model is assumed to be an inclined plane where the inclination angle is to be obtained from experimental observations.

Experimental Equipment

All experiments are conducted at the Laser Laboratory at Iowa State University. The laser system consists of the CO_2 laser, the beam delivery system, the programmable controller, and the work-table.

Laser and Beam Delivery System

A Spectra-Physics Model 820 CO_2 laser is used in the experiments. The continuous wave laser beam leaves the laser cavity through the iris of the shutter mechanism and is reflected through a series of mirrors and is finally focussed onto the workpiece by a 25.4 mm ZnSe lens with a focal length of 127 mm. The size of the laser beam at the focal point is approximately 0.3 mm in diameter. Amidst the mirror-lens configuration is a quarter-wave plate which converts the linearly polarized beam into a circularly polarized beam and thus making it possible to cut equally well in all directions.

To protect the lens and also to assist in the laser process, an oxygen stream is provided at the nozzle assembly. A convergent nozzle with an exit diameter of 2.54 mm is used for all the experiments. Furthermore, a 2mW He-Ne laser is used to align the mirrors and the nozzle such that the beam emerges through the nozzle exit without striking the walls.

Programmable Controller and Work-Table

The opening and closing of the shutter and the oxygen stream, as well as the motion of the work-table are controlled by a programmable Allen-Bradley controller. The work-table can traverse a maximum distance of 0.6 m \times 0.6 m \times 0.15 m in the x , y , and z axes at a maximum speed of 0.42 m/s (or 1000 inch/min). The laser cutting process is carried out in the program mode. The sequence of steps consists of

1. Set work-table velocity
2. Start assist gas flow
3. Open shutter
4. Traverse the work-table (with workpiece mounted)
5. Close shutter
6. Stop assist gas flow

Since it is the cross sectional profile of the cut that is of interest, the work-table is programmed to traverse only half the width of the workpiece before the shutter and the assist gas are shut off.

Experimental Conditions

The laser cutting of mild steel plate (AISI 1008) is used as the modal case in the present study. Two plate thickness are considered: 3.175 mm (0.125 inch) and 6.35 mm

(0.25 inch). For each thickness, three cutting speeds are considered and two cut samples are obtained for each cutting speed. In all cases, the laser power is set at a nominal value of 1000 Watt. The various cutting conditions are summarized in the following:

- Case 1: $t = 3.175$ mm
 - Gas Pressure, $p_t/p_\infty = 1.68$
 - Cutting Speed, $V_c = 0.76, 0.88, \text{ and } 1.02$ m/min
- Case 2: $t = 6.35$ mm
 - Gas Pressure, $p_t/p_\infty = 2.36$
 - Cutting Speed, $V_c = 2.0, 2.5, \text{ and } 3.0$ m/min

The three cutting speeds for each thickness represent 75, 85, and 95 percent of the reported maximum cutting speed [74] for the given laser power and plate thickness for mild steel.

Experimental Results

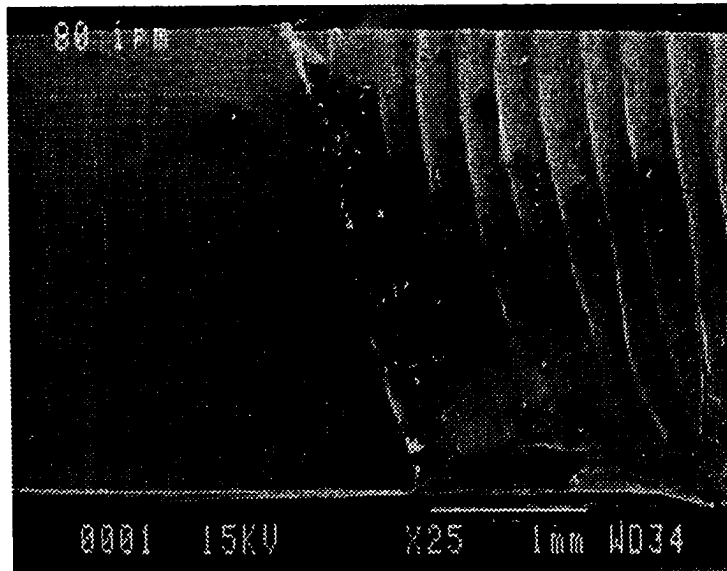
The samples are sectioned with a lathe and the cross sectional profiles of the melt interface are photographed using a scanning electron microscope (SEM). Figure A.1 shows the cross sectional profiles of melt interface for case 1 ($t = 3.175$ mm) and the melt interface profiles for case 2 ($t = 6.35$ mm) are shown in Fig. A.2.

Based only on the SEM pictures, insufficient data are available to establish the dependency of the melt interface inclination angle on the controlled parameters (i.e., thickness, cutting speed, and gas pressure) in the experiments. However, in all cases the melt interface is relatively planar and this observation is supportive of the assumption made in the development of the present model. Furthermore, the inclination angles seem to vary little with respect to the cutting speed for case 1 ($t = 6.35$ mm). In particular, the inclination angles are within 5–7 degrees from the x axis (See Figure 1.4). However, case 2 ($t =$

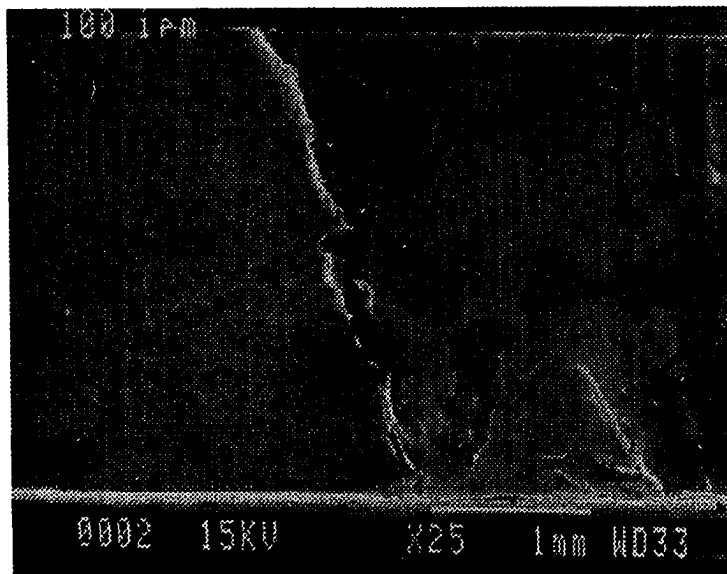
Table A.1: Variation of inclination angle with cutting speed for case 2 ($t = 3.175$ mm)

Cutting Speed, v_c	Inclination Angle, θ
2.0 m/min	15°
2.5 m/min	20°
3.0 m/min	35°

3.175 mm) shows considerable variation in the inclination angle depending on the cutting speed. The inclination angle is observed to increase linearly with respect to the cutting speed, as shown in Table A.1. In the all the SEM pictures of the kerf, the appearance of striation is well defined.

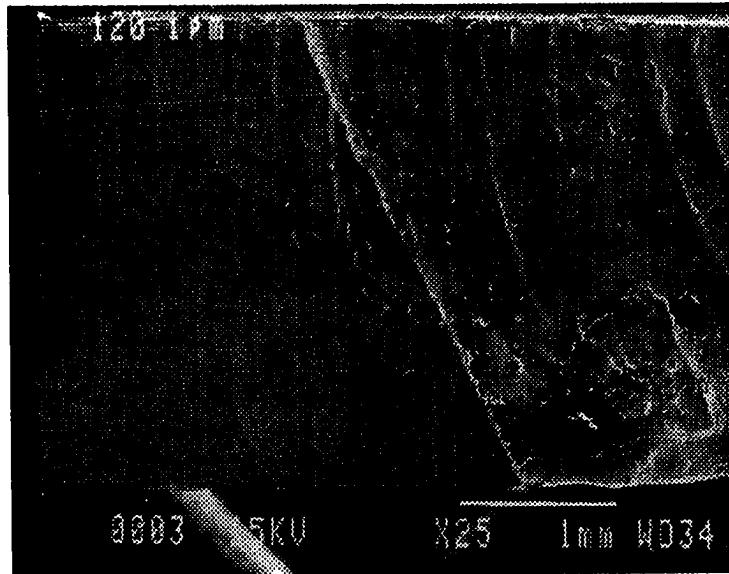


(a) $v_c = 2.0$ m/min



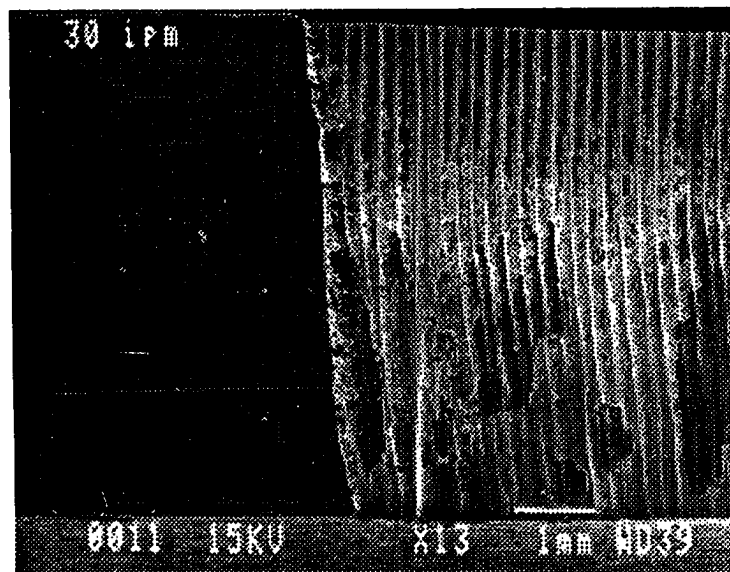
(b) $v_c = 2.5$ m/min

Figure A.1: SEM pictures of the melt interfaces for case 1 ($t = 3.175$ mm)



(c) $v_c = 3.0$ m/min

Figure A.1 (Continued)

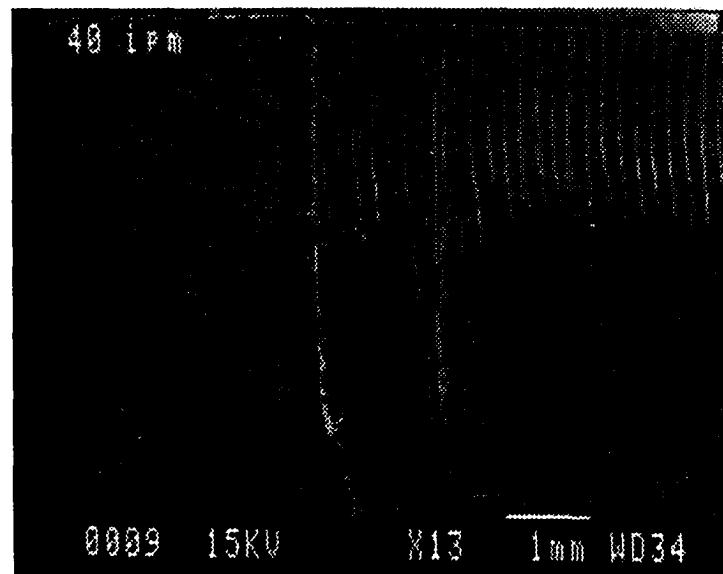


(a) $v_c = 0.76$ m/min

Figure A.2: SEM pictures of the melt interfaces for case 2 ($t = 6.35$ mm)



(b) $v_c = 0.88$ m/min



(c) $v_c = 1.02$ m/min

Figure A.2 (Continued)